INDOOR LOCATING BY BROADBAND HARMONIC RF BACKSCATTER

A Dissertation

Presented to the Faculty of the Graduate School

of Cornell University

in Partial Fulfillment of the Requirements for the Degree of

Doctor of Philosophy

by

Yunfei Ma

May 2016

INDOOR LOCATING BY BROADBAND HARMONIC RF BACKSCATTER

Yunfei Ma, Ph.D.

Cornell University 2016

The Internet of Things (IoT) requires proximity intelligence for many of its applications, especially for identification and locating. Passive radio frequency identification (RFID) locating beyond centimeter accuracy is highly desirable to enable advanced motion tracking, accurate robotic feedback, and gesture recognition. In the conventional RFID system, since the reader-to-tag (downlink) and tag-to-reader (uplink) signals overlap on the same carrier frequency, the self-jamming problem caused by strong leakage signals from the transmitter to the receiver is notorious and poses many constraints on the received signal quality, operation bandwidth, modulation flexibility and system complexity.

We show that harmonic backscatter locating is more effective than the conventional backscatter by exploiting nonlinear elements in passive devices to generate second or higher-order harmonics as the uplink response. Separation of downlink and uplink on different carriers allows immediate self-jamming cancellation and direct un-modulated carrier phase decoding, which bring better received signal quality and broad bandwidth of operation, both of which are critical for the locating system. We take advantage of a hardware and software co-design approach and resolve ambiguous phase cycles with heuristically optimized sparse carrier frequencies in the proposed heuristic multi-frequency continuous wave (HMFCW) ranging algorithm. We designed a 3D real-time locating system for passive devices based on the harmonic backscatter concept which achieved a measured median error less than 3.5cm with repetitious evaluations in different indoor environments.

We further embrace three different diversities: spatial diversity, frequency diversity and time diversity. By exploiting time diversity, we show that the error tolerance can be greatly enhanced to tolerate strong body motion interference, which is critical for many indoor scenarios. With the help of frequency diversity, we show that the antenna size can be greatly reduced and millimeter accuracy indoor ranging can be reliably achieved even with miniaturized low-directivity antennas. By jointly embracing spatial diversity provided by the low-cost passive RFID tags and frequency diversity provided by the broadband harmonic backscatter, we demonstrate ubiquitous tagless objects locating with centimeter accuracy even for small objects which cannot be easily detected by conventional RF systems.

BIOGRAPHICAL SKETCH

Yunfei Ma was born in Xuzhou, Jiangsu province in China. He received his B.E. degree from the University of Science and Technology of China (USTC), Hefei, China. He moved on to pursue his Ph.D. study at the school of Electrical and Computer Engineering, Cornell University in Ithaca, NY, United States. In the summer of 2015, he was an engineering intern with Qualcomm, San Diego, CA. His research interests include indoor locating technology, RFIC design, Radar, 5G communication systems, high speed data links, device modeling and bio-electronics. Yunfei received several awards and honors including the International Microwave Symposium (IMS) 2015 best student paper award (third place) from IEEE MTT society, Irwin and Joan Jacobs Scholar Fellowship from Cornell University and the National Scholarship from Ministry of Education, China.

This document is dedicated to my fiancée Zhen Zhang, my parents Xiaoping Ma and Ying Chen.

ACKNOWLEDGEMENTS

This work would not have been possible without the help and support from many wonderful people.

I would like to express my deepest gratitude to my Ph.D. advisor, Prof. Edwin C. Kan, for his excellent guidance, caring, patience. Prof. Kan gave me lots of freedom so that I could work on a research topic that was different from the traditional topics in our research group. Throughout my Ph.D. years, we explored together and had lots of fruitful discussions. I would have been lost without him. Thank you for always being supportive as a mentor and as a friend. It is also my great honor to have Prof. Kevin A. Tang and Prof. Ehsan Afshari on my Ph.D. committee. Their comments and suggestions provided new insights and helped reevaluate my work from fresh points of view. Prof. Tang helped me understand the beauty of mathematical optimization and I learned my RFIC basics from Prof. Afhshari. Their research also had great impacts on this work.

I would like to thank Fan Yu for being my mentor and teaching me the basic experimental skills in the first year of my Ph.D. studies. I would also like to thank Xiaonan Hui for helping me on the experiments. I am also grateful to my group members: Kshitij, Yingqiu, Shantanu, Krishna, Sarah, Joshua, Lieh-Ting, Philip, Yuan, Yinglei and Pragya for their support. I would also like to thank other fellow graduates at Cornell: Dong Yang, Chaoxu Tong, Xuan Zhao, Xin Huang, Mengjie Yu, Yao Wang, Ruonan Han, Wooram Lee, Rajeev Dokania, Nan Xu, Xiao Wang, Bo Xiang, Haoyan Geng and Bo Sun for their friendship and help.

Special thanks to my parents for their unconditional love. Finally, I thank my fiancée, Zhen Zhang, who gave me support and kept me company along the way.

TABLE OF CONTENTS

Biographical Sketch . . . iii
Dedication . . . iv
Acknowledgements . . . v
Table of Contents . . . vi
List of Tables . . . ix
List of Figures . . . x

1 Introduction 1
1.1 Prior arts and related works . . . 1
1.2 The indoor RF locating challenges . . . 3
1.3 Proposed approach . . . 6
1.4 Main contributions of this dissertation: . . . 7
1.5 Thesis organization . . . 9

2 linear backscatter v.s. nonlinear backscatter 11
2.1 Understanding present limitations . . . 11
2.2 Harmonic/Nonlinear backscatter techniques . . . 15

3 Hardware design for broadband harmonic/nonlinear tranceiving 17
3.1 Broadband passive harmonic tag design . . . 17
3.1.1 Broadband Design Strategy . . . 20
3.1.2 Design Examples . . . 22
3.2 Reflective NLTL with a single antenna . . . 24
3.3 CMOS Compatibility . . . 25
3.4 Integration with an RFID circuitry . . . 27
3.4.1 Broadband harmonic generation unit . . . 28
3.4.2 WISP unit . . . 29
3.4.3 Power routing unit . . . 29
3.4.4 Measurement results . . . 31
3.5 Broadband harmonic reader design for coherent carrier phase detection . 33
3.6 Conclusion . . . 37

4 Heuristic optimized multi-frequency continuous ranging algorithm 39
4.1 Error tolerance function . . . 40
4.2 Selecting optimal frequency combination via Genetic Algorithm . . . 42
4.3 HMFCW in single-band operation . . . 45
4.4 HMFCW in multi-band operation . . . 47
4.5 Conclusion . . . 50

5 Real-time 3D locating by broadband harmonic backscatter **52**
5.1 System overview . . . 53
5.2 Frequency selection . . . 54
5.3 3D locating algorithm . . . 54
5.3.1 Locating error from ranging errors and RX antenna phase center uncertainties . . . 57
5.4 Experimental Evaluation . . . 58
5.4.1 1D ranging measurements . . . 60
5.4.2 2D localization measurements . . . 61
5.4.3 3D locating measurements . . . 62
5.4.4 Locating with different scatters . . . 65
5.4.5 Time budget . . . 66
5.4.6 Real-time 3D tracking . . . 67
5.5 Conclusion . . . 68

6 Diversity exploration: time diversity **69**
6.1 Multi-path variations with body motions . . . 69
6.2 Harmonic ranging in ST-HMFCW . . . 73
6.2.1 K-Consistency Sequential Test . . . 74
6.3 Phase error threshold boosting by time diversity . . . 78
6.4 Experimental verification . . . 81
6.5 Conclusion . . . 83

7 Diversity exploration: frequency diversity **84**
7.1 Basic idea . . . 84
7.2 Multi-paths and coherence bandwidth . . . 85
7.3 AoA on frequencies separated larger than B_c . . . 87
7.4 Digital beamforming with 2-element antenna arrays . . . 88
7.5 Experimental results . . . 90
7.6 Conclusion . . . 94

8 Diversity exploration: spatial diversity **96**
8.1 PhiRadar overview . . . 100
8.2 Non-uniform sampling in Fourier domain . . . 103
8.3 Tagless object position recovery in PhiRadar . . . 106
8.3.1 Basic signal model . . . 107
8.3.2 Differential receiving for $\phi_{l,m}$ cancellation . . . 108
8.3.3 Reconstruction . . . 110
8.4 Experimental verification . . . 112
8.5 Conclusion . . . 114

9 Conclusion **116**
9.1 Future works . . . 118

Bibliography **121**

LIST OF TABLES

3.1 Design parameters for four NLTL design examples 23
3.2 Nominal inductance and capacitance values for the presented NLTLs on IBM 8rf 130nm CMOS process. 27

4.1 Optimized frequency selection samples for single-band/dual-band operation 47

5.1 Optimal Tx frequency combination used in the real-time 3D locating experiment 54

6.1 Optimized frequency selection samples 80

7.1 Optimal Tx frequency combination used in experiment 90
7.2 AoA Gap with and without aluminum curtain (AC) 92
7.3 Ranging errors with and without beamforming & AoA Gap estimates . 94

9.1 Our works discussed in this thesis which are listed in Fig. 9.1 116
9.2 State of art works which are listed in Fig. 9.1 117

LIST OF FIGURES

1.1 Challenges in phase-based locating: (a) Received phase of the backscatter signal is not a pure monotonic function of distance, but with many ambiguous cycles. (b) Self-jamming problem in the state-of-art RFID system. Leakage signals and direct reflection from Tx to Rx can be over 80dB larger than the desired tag signal. (c) The dense indoor multi-path induces large phase errors in the measurements. . . . 5

1.2 In the proposed nonlinear backscatter approach, a tag communicates to the reader at higher order harmonics. 6

2.1 Leakage signals and received backscatter signal in a conventional RFID reader. 12

2.2 Leeson's phase noise model and the noise floor raised up in a conventional RFID reader. 12

2.3 Large leakage signals caused by large antenna reflection S_{11} and hence bandwidth limited in a conventional RFID reader 13

2.4 Nonlinear backscatter based on passive second harmonic generation with mono-static and multi-static tranceivers 14

2.5 Noise floor comparison between conventional RFID and nonlinear backscatter RFID 15

3.1 Broadband harmonic generation by nonlinear lattice: (a) NLTL sections. (b)C-V characteristic of a nonlinear varactor. 18

3.2 $\min\{g(f, f_T, x)|f_L \leq f \leq f_H\}$ versus f_T/f_c when the stage number x (4, 8, 12 and 16) and attenuation per stage vary. BW is set to 20%. 21

3.3 Reflection coefficients versus f/f_T for different Z_0/Z_A. 22

3.4 Second-harmonic power conversion gain in NLTL sections. The input power is fixed at 0 dBm. 24

3.5 Single antenna configuration with open-end NLTL. 25

3.6 Die photo of the 10-stage matched, 5-stage open-ended and 5-stage short-ended NLTLs (f_T = 10 GHz). 26

3.7 Measured output second harmonic power of the 10 GHz 10-stage matched, and 5-stage open-ended and short-ended NLTL with 0 dBm sinusoidal input signal (Pin = 0 dBm). 26

3.8 (a) System architecture of the proposed Harmonic-WISP RFID tag. (b) An example of reader inquiry signal sequence in the broadband harmonic backscatter operation. 28

3.9 Power routing in Harmonic-WISP: (a) The start-up/energy harvesting mode; (b) The harmonic generation mode. 30

3.10 Photo of the Harmonic-WISP prototype 32

3.11 Measured input reflection coefficient plotted in Smith Chart for energy harvesting mode and harmonic generation mode. 33

3.12 (a) Measured Harmonic-WISP decoded downlink bit stream (repeated 1010101010); (b) Measured Harmonic-WISP modulated backscatter signal on second harmonic (bit stream 11010010); (c) Measured spectrum of uplink (ASK off) at 0dBm 915MHz fundamental input; (d) Measured spectrum of uplink (ASK on) at 0dBm 915MHz fundamental input. 34
3.13 Photo of proposed homedyne nonlinear backscatter reader. 35
3.14 Block diagram of reader. 35
3.15 Measured reader RX receiving gain in broadband. 36
3.16 Measured maximum reader TX power and corresponding input referred interference in broadband. 37

4.1 Selecting optimal freq. combination with small number of freq. via genetic algorithm 42
4.2 HMFCW ranging: (a) single-band and (b) multi-band operations. . . . 45
4.3 The minimum number of frequencies $K(\mathbf{F}, R)$ needed for $\Phi(\mathbf{F}, K, R)$ to reach $\pi \mathrm{BW}/2$. λ_c is the wavelength of the center frequency f_c in $\mathbf{F}$. . . 47
4.4 HMFCW averaged ranging error versus maximum phase error by Monte Carlo simulation for single-band and dual-band operations of the five cases in Table 4.1. Phase error is uniformly distributed within $[-\Delta\theta_{\max}, \Delta\theta_{\max}]$. 48
4.5 Relationship between the phase error threshold Φ and the center frequency when the number of frequencies is not limited. $R/\lambda_{c2} = 25$. . . 49
4.6 Relationship between Φ and center frequencies selection with small number of frequencies and different Rmax denoted as $(R/\lambda_{c2}, K)$. BW1=BW2=5% in simulation. Number of frequencies in each band are same, all equal to K/2. 50

5.1 Illustration of the passive nonlinear backscatter real-time 3D locating system. 52
5.2 Ranging error simulated from Monte Carlo simulation using frequencies shown in Table.5.1 55
5.3 3D locating by solving hyperboloid intersection 56
5.4 Locating errors from (a) ranging error. (b) antenna phase center uncertainties. 57
5.5 Experiment setup in indoor environments (a) Lab environments. (b) In a narrow lounge passage. (c) In a classroom. 59
5.6 Measurement on (a) thermal noise induced phase error (b) multi-path induced phase error. 60
5.7 CDF 1-D ranging error. 61
5.8 (a) CDF 2-D localization errors (b) a sample of 2D localization measured on the experiment table for various locations. 62
5.9 (a)(b)(c) CDF 3D locating error CDF measured in environments shown in Fig. 5.5 (a) (b) and (c) respectively. 63

5.10 Testing sample of 3D locating in scatterer-free (a) and 5 metal scatterers (b) scenarios. 64
5.11 Median and maximum errors with different number of scatterers. . . . 65
5.12 Pie chart of time consumption for one 3D locating measurement. . . . 65
5.13 Passive tag real-time 3D tracking: (a) moving left, (b) moving up (c) moving inward, (d) moving circularly. 67
5.14 Real-time 3D tracking of a passive tag attached to a toy train. 68

6.1 Harmonic backscattering with body motion interference 70
6.2 Received second harmonic phase error fluctuations caused by random body motion 72
6.3 Auto-correlation in $\exp(j\alpha)$ and B. 73
6.4 (a) Integer estimation error evolution; (b) Effects with and without K-consistency sequential tests in HMFCW ranging. 75
6.5 State machine of K-consistency sequential test. 76
6.6 Estimated integer error profile evolution as $\Delta\theta_{\max}$ increases at 20% BW. 77
6.7 ST-HMFCW performance vs. $\Delta\theta_{\max}$ for (a) different K, BW = 20%; (b) different BW, $K = 4$. 78
6.8 ST-HMFCW with $K = 4$, BW = 20% under random body motion interference: (a) Received SH phase fluctuations for each inquiry frequency; (b) Ranging error and delay. 79
6.9 Experiment setup second harmonic ST-HMFCW ranging. 80
6.10 Relative phase errors caused by body motion when a person is walking around of the harmonic backscatter signal for the tag fixed at 0.9m. . . 81
6.11 Corresponding ranging errors and delays caused by body motion when a person is walking around in ST-HMFCW ranging with K = 4 at BW=14% based on the measurements in Fig. 6.10. 82

7.1 High-directivity antenna and low-directivity antenna. Low-directivity antenna is much smaller, lighter, more flexible, but sees more multi-paths. 85
7.2 Simplified wireless channel impulse response and power delay profile . 86
7.3 Frequency selective channel response resulted from multi-paths 87
7.4 Quality Estimate w/ Gap of AoA. When LoS is strong, two frequencies will have close AoA. When multi-paths are strong, two frequencies will have different AoA estimations when separated larger than B_c 88
7.5 Frequency selective channel response resulted from multi-paths 89
7.6 Beamforming factors with different antenna separation at different frequencies. The incident angle is set at 45°. 90
7.7 Experimental setup: (a) Coordinates in the ranging experiment. (b) The harmonic backscatter reader. (c) The indoor ranging setup. (d) Richer scattering environment was created with aluminum curtain to test the multi-path dominance indicator by the AoA gap. 91

7.8 Experimental measurements: (a) Received signal amplitude ratio between antennas A and B within each array at 1798MHz to indicate the effect of indoor multi-paths. (b) Reduction of received phase errors at 1798MHz array 1 antenna B for (phase(x) − phase(x=25cm)) with digital beamforming. (c) Ranging errors from HMFCW for 5 frequencies with and without digital beamforming. (d) AoA gaps with and without aluminum curtain. 93
7.9 CDF plot of ranging error results. 94

8.1 (a) Temporal signal recovery via Fourier domain sampling. (b) Object reflectivity can also be recovered by Fourier domain sampling if we find its spectrum. 98
8.2 (a) Illustration of PhiRadar system. (b) Broadband harmonic tag based on NLTL. (c) Harmonic reader for coherent carrier phase and amplitude measurement. 100
8.3 Multi-static passive Radar system. 102
8.4 Spherical coordinates for the multi-static passive RF locating system. . 103
8.5 Effects of Fourier domain sampling coverage on locating 2 adjacent targets by the imaging function $|F(\mathbf{p})|^2$ in Eq. (8.17). PhiRadar uses both frequency and spatial diversity to enhance Fourier domain sampling for accurate and unambiguous location estimations. 111
8.6 Experimental setup: (a) Schematic;(b) Photo. 112
8.7 2D position recovery of small objects for the single and dual target cases. 113
8.8 Fourier domain samples in experiment. 114
8.9 CDF of experiment measurement errors. 115

9.1 Comparison of proposed works with the state of art 118

CHAPTER 1

INTRODUCTION

The Internet of Things (IoT) requires proximity intelligence for many of its applications, especially for identification and locating [1, 5, 11, 12, 13]. A passive tag that can operate without a battery is free of maintenance and ideal to be attached to any article as the last layer in IoT [2] . High-accuracy locating and tracking around centimeter accuracy is highly desirable for these passive devices in order to enable new motion tracking systems [8, 9], accurate robotic feedback [13] for object fetching and delivery, and gesture acquisition without the need for ambient light and expensive cameras [14].

1.1 Prior arts and related works

Although passive tags can provide an distinguishable signal from ambient radio frequency (RF) reflections, accurate locating is still a very challenging task due to the rich scattering indoor environment. Among RFID locating methods, received signal strength (RSS) [1, 6, 51, 50] suffers from poor accuracy and reliability due to multi-path interference because RSS is not a sensitive function of distance. Time of flight (TOF) is not suitable for short range due to the synchronization difficulty, signal sampling complexity, the difficulty in forming an ultra wideband (UWB) wave packet in passive devices [7], and the challenge of measuring event of nano-seconds round-trip time delay [16]. Carrier phase-based methods are preferred for their ultra-high sensitivity as a function of distance [5, 11] and many techniques can be inherited from the mature outdoor radar. In recent years, several phase-based systems had been proposed, such as holographic tag localization [17], Tagoram [8], RF-compass [13], PinIt [18], Backpos [15] and RF-IDraw [9]. However, these systems came with a variety of constraints in order to be

extended to a ubiquitous 3D passive device locating system. These constraints include but are not limited to:

(1) Requirement of relative motion: Several systems had shown deca-centimeter to centimeter accuracy but relied on relative reader and tag motion. Holographic RFID localization [17] and later Tagoram [8] utilized inverse synthetic aperture radar (ISAR) techniques [22] to form a large virtue antenna array in order to pin down the initial position of an RFID tag with a known trajectory. PinIt [18] adopted an synthetic aperture radar (SAR) approach which required reader antenna motion in order to collect multi-path profiles of the target tag which was later compared to many anchor tags. RF-compass [13] utilized a robot which carried several reference tags to rotate around a target tag to find its position. However, in many scenarios, the relative motion between tags and reader antennas cannot be easily implemented. In some cases, the reader antennas position has to be fixed for indoor applications.

(2) Availability of reference tags or anchor nodes: The locating accuracy can be greatly improved if we have the luxury of reference tags or anchor nodes with known accurate positions. Both PinIt [18] and RF-compass [13] utilized reference tags. PinIt compared the multi-path profiles and found the nearest reference tag to the target tag. RF-compass relied on the distance comparison of the target tag to multiple reference tags to achieve a 2D-plane partitioning with the help of a moving robot. Reliance on reference or anchor tags brings forth the heavy dependence on the granularity of the reference tags. In order to achieve high accuracy, the number of required reference tags may be large. Reference tags also need initial deployment with accurate positions, which puts additional hurdles to many applications.

(3) Knowledge of moving trajectory: In order to mitigate multi-path effects, ISAR-based systems such as holographic RFID locating [17] and Tagoram [8], would need prior knowledge of the tag moving trajectory. Tagoram relaxed this constraint by fitting

moving trajectory from tag moving speed estimation. However, not only the accuracy is compromised, but the latency is also prolonged. The moving tag may need to finish the 10 laps of a fixed trajectory which took 5 minutes before locating can be performed.

(4) Rigid configuration of reading antenna: Phase-based methods can be vulnerable to ambiguous phase cycles. Instead of directly determining the ambiguous cycle integer, systems like BackPos [15] constrained the tag motion within a region of "interrogation zone", where the differential distance from two reader antennas to the target tag falled within half wavelength. When the target tag was out of the interrogation zone, such system became unreliable. RF-IDraw [9] took advantage of antenna arrays with different resolutions and ambiguities in a 2D-plane. To resolve ambiguity, RF-IDraw required closely-spaced, low-resolution antenna arrays to remove the grating lobes. Furthermore, the rigid antenna configuration can be problematic to integrate with other system components.

(5) Limitation to 2D: Holographic RFID localization [17], RF-compass [13], Tagoram [8], BackPos [15] and RF-IDraw [9] were essentially 2D locating systems, and were difficult to extend to the 3D space. For example, RF-compass required a moving robot around the target tag which was difficult in 3D space. BackPos and RF-IDraw utilized linear antenna arrays and hence difficult to resolve 3D positions. Holographic RFID locating and Tagoram needed to compute the image of "Hologram", which had high computational cost in the 3D space.

1.2 The indoor RF locating challenges

Can we build a 3D indoor locating system for passive devices without the above constraints? First of all, we must understand the difficulties for the phase-based locating in the current RFID systems. The main challenges include:

(1) The ambiguous phase cycles: Since the measured phase is always within $[0, 2\pi)$, cycle ambiguity exists when the distance is longer than one wavelength. When the measured phase is θ, the actual phase can be $\theta + 2n\pi$ where n is the cycle integer as depicted in Fig. 1.1(a). The cycle integer must be solved correctly in order to reduce ambiguity in the 3D location.

(2) Self-jamming and bandwidth limitation: For passive backscatter communication, the downlink and uplink are extremely asymmetric due to the need to reduce tag cost and complexity. Such asymmetry brings forth the notorious jamming problem in RFID readers as shown in Fig. 1.1(b). It is not uncommon that the leakage from the reader transmitting signal to receiver is 80dB higher than the received tag response. Phase noise skirts of the strong transmitting signal at effective isotropic radiated power (EIRP) above 4 Watts can drastically raise the receiver noise floor [23, 24]. The input leakage signal needs proper isolation to be less than the 1-dB suppression point of the receiver to avoid saturation and nonlinear effects. The extremely high isolation from transmitter (Tx) to receiver (Rx) puts stringent requirements on frontend RF circulator and antenna reflection loss S_{11}, which leads to limited operation bandwidth due to the Bode-Fano criteria [28].

(3) Large phase error induced by multi-paths: A dense multi-path environment in Fig. 1.1(c) may cause measured phase error up to several tens of degrees. For example, if a multi-path component is only 3dB below the line of sight (LOS), the largest induced phase error is $\pm 45^\circ$. We need to deal with low signal-to-interference ratio (SIR) even the LOS path appears to be clear. With moving scatterers such as human body, the phase detection can be easily smeared. The problem is even more complicated when the ambiguous cycle comes into play. Few works considered the theoretical phase error bound for correct phase cycle estimation.

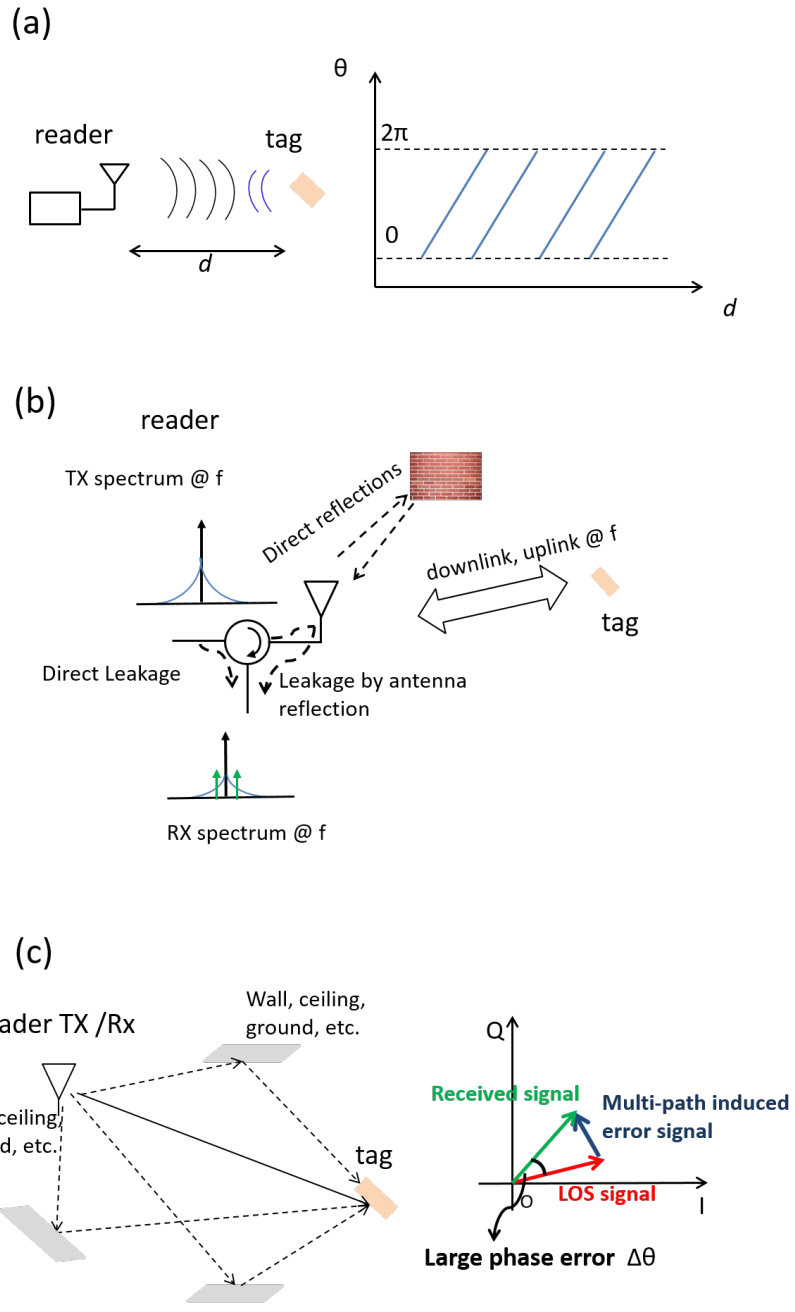

Figure 1.1: Challenges in phase-based locating: (a) Received phase of the backscatter signal is not a pure monotonic function of distance, but with many ambiguous cycles. (b) Self-jamming problem in the state-of-art RFID system. Leakage signals and direct reflection from Tx to Rx can be over 80dB larger than the desired tag signal. (c) The dense indoor multi-path induces large phase errors in the measurements.

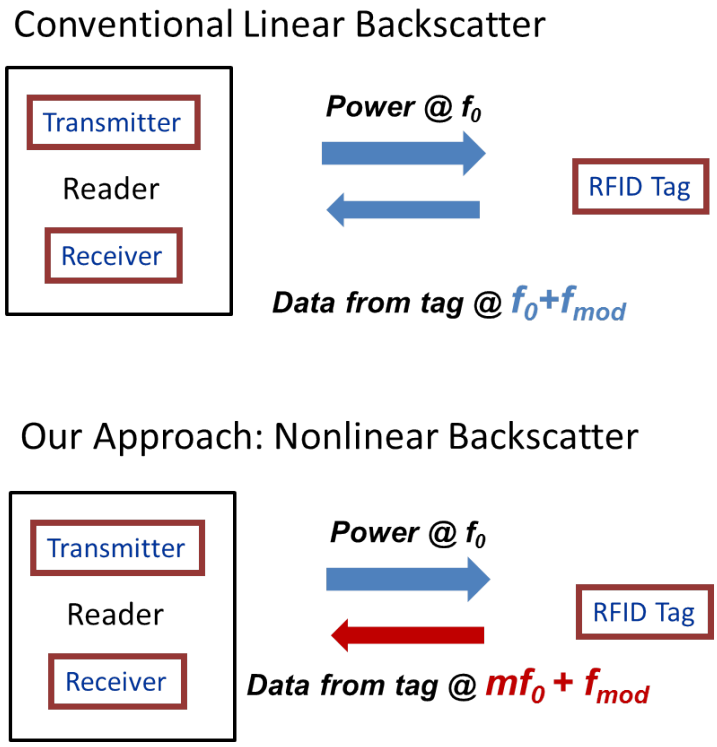

Figure 1.2: In the proposed nonlinear backscatter approach, a tag communicates to the reader at higher order harmonics.

1.3 Proposed approach

Notice that most of the previous works attempted tackling the problem with commercial off-the-shelf (COTS) equipment and improved algorithms. In fact, the constraints come from not only the algorithm but also the hardware implementation. Hardware and software co-design approach may offer a better solution. This thesis proposes a new system solution to directly solve the above issues with high flexibility and least constraints. The proposed solutions offer an indoor real-time 3D locating approach for passive devices within centimeter accuracy, small latency and convenient calibration. The basic idea is to exploit nonlinear effects in passive devices instead of the conventional linear backscatter approach as shown in Fig. 1.2. When a passive tag receives reader inquiry signal in the conventional backscatter, it responds to the reader by switching

its antenna "on"and "off". The antenna switching effectively changes the reflected RF signal energy. Since the downlink and uplink are on the same carrier, the conventional backscatter is essentially linear. In our nonlinear backscatter approach, nonlinear circuit elements such as varactors and diodes are used to passively generate second or higher-order harmonics. The uplink information is then encoded on these harmonics instead of the fundamental carrier. The separation of downlink and uplink signals in nonlinear backscatter can fundamentally eliminate the self-jamming problem in conventional RFID, enabling broadband operation. The harmonic signal can be detected even if it is unmodulated. With the broadband operation, we then resolve ambiguous cycle integers with a novel sparse multi-frequency sequence which is selected by a heuristic optimization such as genetic algorithm (GA) to offer the best phase error tolerance with small number of hopping frequencies.

1.4 Main contributions of this dissertation:

The contribution of this dissertation is summarized below:

(1) We demonstrate the first real-time 3D passive device locating system based on broadband harmonic backscatter. We achieve beyond centimeter accuracy locating and show that passive harmonic backscatter can eradicate many traditional RFID hardware constraints and enable extremely broadband operation for accurate ranging and locating.

(2) With the help of broadband coherent carrier phase detection enabled by the nonlinear approach, we directly determine the phase cycle integer based on a novel heuristic multi-frequency continuous wave (HMFCW) ranging method. We generalize two basic theorems for HMFCW ranging regarding the phase error tolerance. HMFCW is able to compute correct cycle integer with 100% reliability when multi-path induced phase error is within $\pm 90^\circ \times \mathrm{BW}\%$. In our experiment, we achieved measured ranging error

less 1 *cm* with multi-path phase error that can go up to more than ±60°.

(3) Our methods requires minimal calibration efforts for the environment. The only calibration is to compute the cable delay between the receiving antennas and the reader. Our present system is able to compute one 3D position every 0.1 seconds.

(4) We show that robustness and flexibility of the proposed approach can be further extended by embracing three different diversities: spatial diversity, frequency diversity and time/temporal diversities.

(5) By exploiting temporal diversity, we show that the phase error threshold can be greatly enhanced to tolerate strong body motion interference. We point out that there is a trade-off between the required percentage bandwidth and latency when the wireless channel is fast-fading in HMFCW ranging and therefore, a high phase error tolerance can be obtained even for small percentage bandwidth systems.

(6) The use of small, light-weight and flexible low-directivity omni-directional antennas is highly desired to replace the large, heavy and cumbersome high directivity antennas for an easy integration with other mobile platforms. However, low-directivity antennas bring much more multi-path interference compared to the high directivity antennas. With the help of frequency diversity, we show that millimeter accuracy indoor ranging can be reliably achieved even with miniaturized low-directivity omni-directional antennas by adopting the coherence bandwidth concept in the HMFCW ranging algorithm. When the LoS signal is weaker than the multi-path interference signal, angles of arrival (AoA) at carrier frequencies that are separated larger than coherence bandwidth will become independent. We propose a system that utilize this phenomenon to evaluate channel quality and the reliability of measurement results to greatly improve the ranging accuracy.

(7) Finally, we show that by jointly embracing spatial diversity provided by the low-cost passive RFID tags and frequency diversity provided by the broadband nonlinear

backscatter, high accuracy tagless objects locating can be realized. We propose a system called PhiRadar which stands for passive harmonic indoor radar. To the best of our knowledge, PhiRadar is the first system to pursue wide and dense Fourier domain sampling of the reflectivity function with low-cost passive RFID technology. We demonstrate a prototype that can even locate objects with size about 5cm. We show that single and dual objects can be located within area of 1.2m $\times$ 1.2m with locating errors below 3cm for 90% of measurements.

1.5 Thesis organization

This dissertation intends to discuss high accuracy locating techniques based on passive nonlinear backscatter thoroughly. The thesis will begin with detailed comparisons between the nonlinear backscatter approach and the conventional linear backscatter approach as well as the discussions on operation bandwidth enhancement opportunities in the proposed passive nonlinear backscatter locating systems, thanks to the self-jamming elimination in Chapter 2. Chapters 3 and 4 will discuss the basic hardware and algorithm design respectively. In Chapter 3, we will describe the design of passive nonlinear backscatter tags based on NLTL and its integration with RFID logic circuits. We will then address the broadband RFID reader design for accurate coherence carrier phase detection. The theory and algorithm of HMFCW ranging for both single band and multiband operation to reliably solve ambiguous phase cycle integers will be addressed in Chapter 4. Chapter 5 will present the real-time 3D indoor locating system based on nonlinear backscatter approach. The 3D location is directly computed from accurate ranging results with an efficient nonlinear CG algorithm to resolve the hyperboloid intersection problem. The antenna configuration is flexible and only requires 4 Rx antennas to give a unique location in 3D space. Chapters 6, 7 and 8 present extension of the proposed

nonlinear backscatter approaches through temporal, frequency and spatial diversity explorations. we first describe how to utilize temporal diversity to further boost phase error threshold in fast-fading channels to tolerate strong body motion interference in Chapter 6. In Chapter 7, by embracing frequency diversity and design HMFCW ranging with careful consideration on indoor coherence bandwidth, we demonstrate millimeter level accuracy ranging by low directiviy antenna with quality estimate. We show that the proposed nonlinear backscatter is not only suitable for passive tag tracking, but also good for tagless object tracking. In Chapter 8, we present PhiRadar, a high accuracy tagless object locating system with the assistance of ambient harmonic RFID tags. We point out that to achieve high accuracy tagless object locating, fundamentally, one need to acquire better knowledge on a Fourier domain transformed from objects reflectivity. PhiRadar utilizes ambient broadband harmonic RFID backscatter which is able to provide low-cost spatial and frequency diversity simultaneously to achieve better Fourier domain sampling than the conventional RFID technology.

CHAPTER 2

LINEAR BACKSCATTER V.S. NONLINEAR BACKSCATTER

2.1 Understanding present limitations

In order to achieve accurate indoor locating, broad bandwidth can help tolerate multi-path phase errors. Such trade-off has been exploited in frequency modulated continuous-wave (FMCW) Radar and UWB systems [32], which is however very challenging in passive backscatter communication. The major problem is that passive tags are battery-less and hence they cannot afford regular RF frontends to generate or amplify an RF signal in the range of GHz. Today, a passive RFID tag operating power is typically in the vicinity of 10 μW, which can only passively reflect the reader inquiry signal. The power of the reader received tag response P_r experiences twice free-space propagation losses, one from the downlink (reader to tag) and the other from the uplink (tag to reader):

$$P_r = GP_t \frac{\lambda^4}{(4\pi)^4 |\mathbf{r}_{tag} - \mathbf{r}_{reader}|^4} \tag{2.1}$$

where G includes reader Tx/Rx antenna gains and tag Tx/Rx antennas gains, $\mathbf{r}_{tag}$ and $\mathbf{r}_{reader}$ are position vectors of the tag and reader antennas, P_t is the reader transmitting power and λ is the wavelength. Notice that P_r is inversely proportional to the distance to the 4th power. One the other hand, a passive tag generates its own voltage supply through energy harvesting using an RF-to-DC converter [21], however, the efficiency of an RF to DC converter can be lowered down to be less than 10% to when the input RF voltage is in the vicinity of the transistor threshold voltage. Therefore, backscatter communication requires a very strong reader inquiry signal to power up the passive tags. So, today, an RFID reader usually operates with > 1W transmitting power while P_r can be less than 100dB of the Tx power. This brings forth the problem of self-jamming.

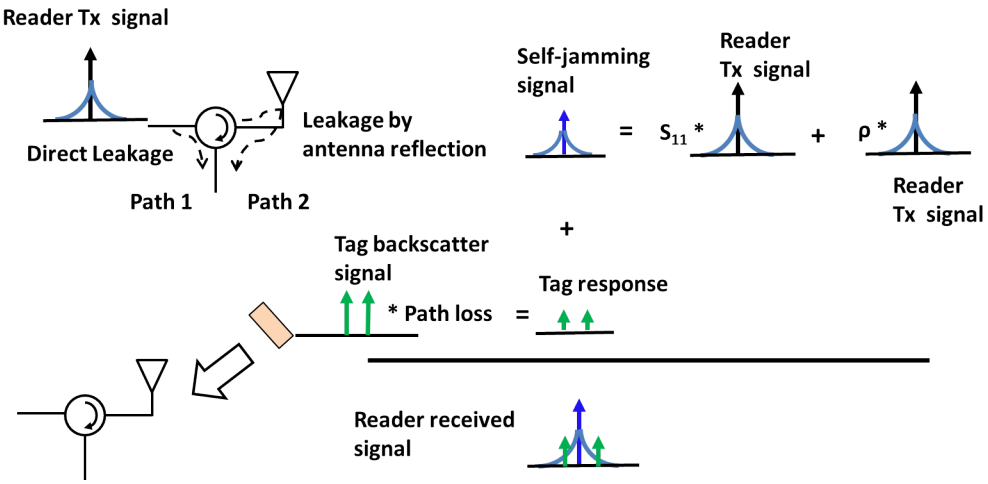

Figure 2.1: Leakage signals and received backscatter signal in a conventional RFID reader.

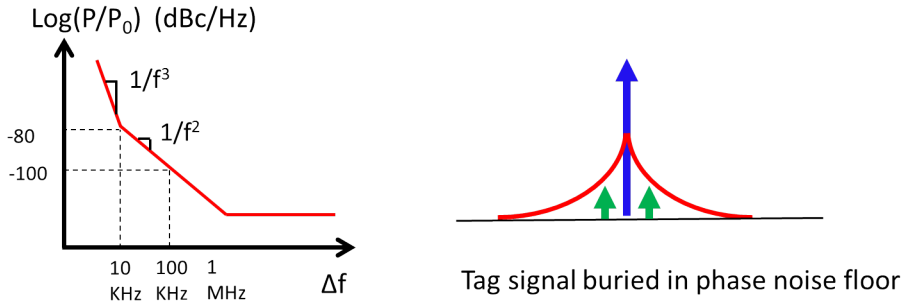

Figure 2.2: Leeson's phase noise model and the noise floor raised up in a conventional RFID reader.

The RF signal flow of a conventional RFID reader is shown in Fig. 2.1. In addition to P_r, there are two main leakage signals. One leakage path is from the circulator [28] (denoted as path 1 in Fig. 2.1). A circulator is an isolation device that is commonly used to separate the Tx/Rx channels. A good RF circulator can usually provide 25 to 30dB isolation. The other leakage path is from the front end antenna reflection (denoted as path 2 in Fig. 2.1). Let S_t denote the transmitted signal, then the total leakage signal S_{leak} can be written as

$$S_{leak} = S_{11}^{ant} S_t + \rho S_t \tag{2.2}$$

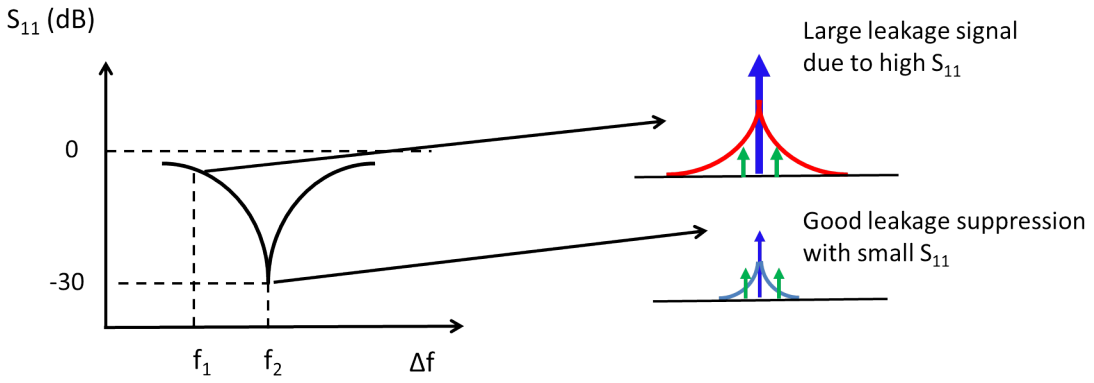

Figure 2.3: Large leakage signals caused by large antenna reflection S_{11} and hence bandwidth limited in a conventional RFID reader

where the antenna reflection is represented by S_{11}^{ant} and the isolation of circulator is denoted as ρ. The received signal is the sum of the leakage signals and the reader received tag response, which is fed into the input of the receiving block. If the leakage signal is not well suppressed, it may cause receiving saturation which leads to failure of operation. Another issue with unsuppressed leakage is the raised noise floor. Different from other communication systems, passive backscatter is usually full duplex in the way that the Tx and Rx are active simultaneously. The noise floor is set by the phase noise of the leakage signal rather than the thermal noise floor. The phase noise [33] is a low-frequency noise located around the carrier and is very difficult to filter it out. Phase noise filtering would require ultra high Q components that are not commonly available in RF frequency. Fig. 2.2 shows the Leeson's model [33] of phase noise, When the offset frequency approaches zero, the noise power spectrum will increase according to $1/\Delta f^2$. The noise slope may be even $1/\Delta f^3$ when the offset frequency further decreases. For passive devices, because the operating power is very low, hence the data modulation is at the range of kHz to hundreds of kHz. The modulated backscatter signal will overlap with the phase noise of the leakage signal. For a common RF frequency source, the phase noise at 10kHz is about -80dBc/Hz. If a leakage signal is of 0dBm, this -80dBm/Hz

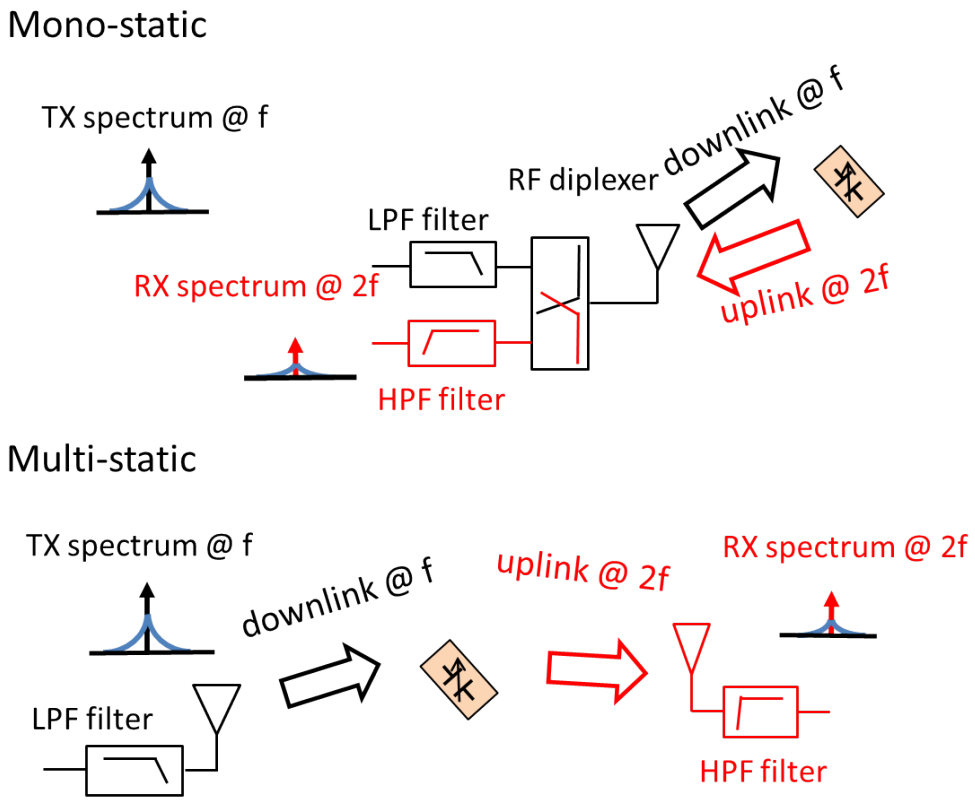

Figure 2.4: Nonlinear backscatter based on passive second harmonic generation with mono-static and multi-static tranceivers

phase noise floor is much higher than the -174dBm/Hz thermal noise floor. For an even larger leakage, the desired backscatter may be totally buried in the phase noise skirt as depicted in Fig. 2.2. Therefore, a present RFID reader can only have receiving sensitivity of around -70 dBm [38].

Due to the above reasons, the leakage signal must be handled properly. As shown in Fig. 2.3, the front-end antenna reflection loss S_{11} must be minimized for all operating frequencies. However, there is a trade-off between the reflection loss and bandwidth for RF antennas, which is set by the Bode-Fano criteria [28, 33]. If we want broad bandwidth, we have to sacrifice the lowest S_{11}. For an RC load, the Bode-Fano criteria

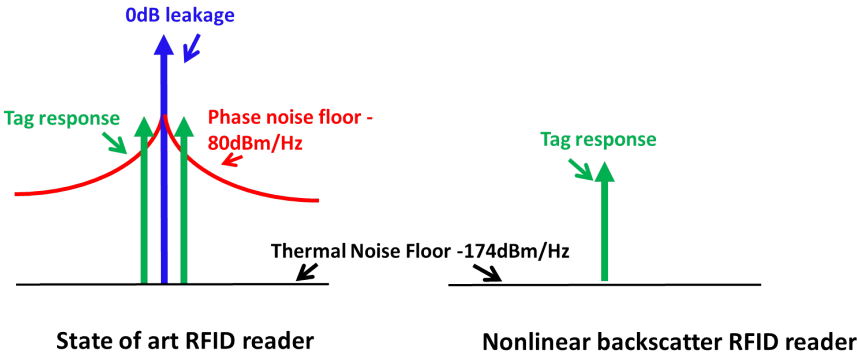

Figure 2.5: Noise floor comparison between conventional RFID and nonlinear backscatter RFID

can written as:

$$\int_0^{\infty} \ln \frac{1}{S_{11}(f)} \mathrm{d}f \leq \frac{\pi}{RC} \tag{2.3}$$

2.2 Harmonic/Nonlinear backscatter techniques

The self-jamming problem can be fundamentally eliminated via nonlinear backscatter, as shown in Fig. 2.4. When we modulate the uplink response on the second harmonic which is passively generated by nonlinear devices, we can use broadband low-pass filters (LPF) and high-pass filters (HPF) to easily separate the Tx and Rx signals. Due to the large frequency separation which is in the range of GHz, it is not difficult to filter out the Tx signal at the fundamental frequency even by 90dB rejection. The nonlinear backscatter approach is very flexible in construction and deployment. An RF diplexer can be inserted between the antenna and the filter banks for mono-static transceiving. In comparison with the conventional RFID reader, where mono-static antenna with a circulator is more stable, our nonlinear backscatter method can readily implement the multi-static tranceiver approach as shown in Fig. 2.4, because antenna isolation by filters in close space can now be guaranteed.

In nonlinear backscatter, the antenna reflection loss S_{11} is not a bottleneck any more. Since all the harmonics from power amplifier (PA) is immediately stopped by the LPF filter, only the fundamental frequency is at the Tx antenna. Therefore, no matter how much power at the fundamental frequency is reflected from the antenna to the receiving input, it can be immediately stopped by the HPF. The noise floor for the receiver is determined by the thermal noise floor at -174dBm/Hz and now we can even retrieve the carrier phase of un-modulated carriers as shown in Fig. 2.5.

CHAPTER 3

HARDWARE DESIGN FOR BROADBAND HARMONIC/NONLINEAR TRANCEIVING

3.1 Broadband passive harmonic tag design

Previous research on distributed microwave structures had shown that higher order of harmonics can be efficiently generated with periodically loaded varactors and inductors [42, 45]. Such microwave structures are called nonlinear transmission lines (NLTLs) [46], which allow ready broadband matching to the antenna. As shown in Fig. 3.1 (a) for a typical section of NLTL, when the fundamental frequency propagates along a NLTL, due to the nonlinearity of varactors as shown in Fig. 3.1(b), second and higher-order harmonics are generated in each section. When the propagation speed of harmonics is equal to that of the fundamental frequency, they will add up constructively with the harmonics generated in later sections. Hence, the power in the fundamental frequency will be gradually converted to harmonics. Because the tag received signal is usually below 0dBm, it can be treated as a small signal. The varactor can then be treated as a variable capacitor whose capacitance is a linear function of the voltage using Taylor expansion to the first order [45]:

$$C(V) = C_0(1 + bV) \tag{3.1}$$

where C_0 is the capacitance corresponding to zero voltage and the slope b reflects the nonlinearity which is process dependent. For a common RF CMOS process, b is about 0.5/V. The second harmonic at different stages can be written as [42, 45]:

$$|V_{2nd}(x)| = \left| \frac{bV_0^2}{2} \frac{\gamma_2^2}{\gamma_2 + 2\gamma_1} \frac{\sinh(\frac{\gamma_2 - 2\gamma_1}{2}x)}{\gamma_2 - 2\gamma_1} e^{-\frac{\gamma_2 + 2\gamma_1}{2}x} \right| \tag{3.2}$$

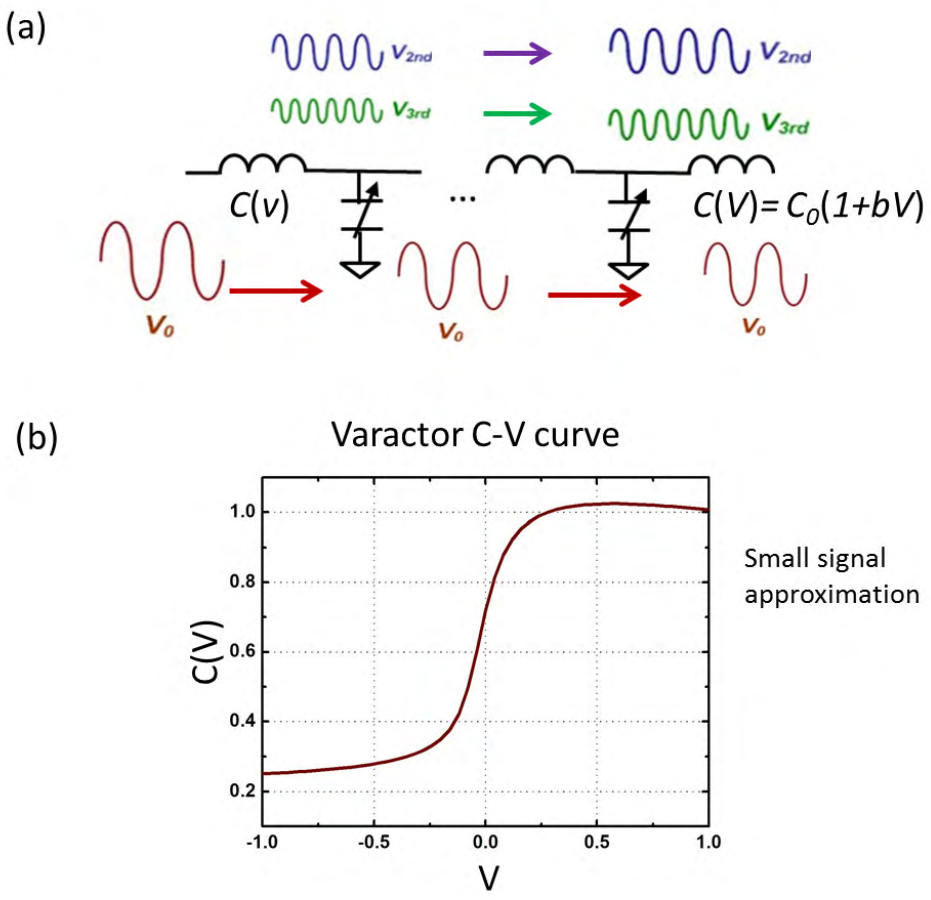

Figure 3.1: Broadband harmonic generation by nonlinear lattice: (a) NLTL sections. (b)C-V characteristic of a nonlinear varactor.

In Eq. (3.2), x is the stage number and $\gamma_{1,2}$ are propagation constants for fundamental and second harmonic signals including the dispersion and loss effects. An efficient design would require careful trade-offs between the number of stages, dispersion and loss effects [42]. γ can be expressed as

$$\gamma_m = \alpha_m + \beta_m \tag{3.3}$$

where $m = 1, 2$ which denotes the m-th harmonic. β is a function of frequency [78].

$$\beta_m = \arccos\left(1 - 2(m\frac{f}{f_T})^2\right) \tag{3.4}$$

where f_T is the cutoff frequency which depends on inductance L and varactor capacitance at zero bias voltage C_0:

$$f_T = \frac{1}{\pi\sqrt{LC_0}} \tag{3.5}$$

For a low-loss transmission line, α_m can be approximated as

$$\alpha_m = \frac{R}{2}\sqrt{\frac{C_0}{L}} + \frac{G}{2}\sqrt{\frac{L}{C_0}} \tag{3.6}$$

where R and G are the series resistance and parallel conductance of inductors and varactors respectively. Another important parameter is the Bloch impedance Z_B

$$Z_B = Z_0\sqrt{1 - \left(\frac{f}{f_T}\right)^2} \tag{3.7}$$

where $Z_0 = \sqrt{\frac{L}{C_0}}$ is the characteristic impedance. A broadband design requires matching at both input and output ports.

An important feature of NLTL backscatter tags: although it is a nonlinear device, the phase shift of generated second harmonic compared to the phase of the input fundamental frequency exhibits power independence as shown in Eq. (3.2), as long as Eq. (3.1) gives a decent approximation to the nonlinear behavior. This feature allows accurate calibration as well as fast operation in inquiry power adjustment because only coarse tuning will be needed in case the input power becomes too large. When differential ranging techniques are employed, there is no need to make difference between power-dependent and power-independent phase shift along NLTL as the phase shifts are always canceled out in the differential ranging algorithm. Details in the differential ranging algorithm will be discussed later in Chapter 4.

3.1.1 Broadband Design Strategy

In this section, we present a simple design strategy for broadband harmonic generation. We will avoid complex formula but instead pin down parameters intuitively by Eqs. (3.1)-(3.7). Further optimization can be achieved through simulation around initial parameter estimations.

Assume the intended fundamental frequency in operation is between $f_L = f_c(1 - \mathrm{BW}/2)$ and $f_H = f_c(1 + \mathrm{BW}/2)$, where f_c is the center frequency and BW denotes the normalized bandwidth. Given b, R and G as technology parameters and f_c and BW, f_T, Z_0 and x can be selected for high conversion efficiency over the whole bandwidth of interest. Finally, component parameters L and C_0 can be determined.

Cutoff frequency f_T and stage number x:These two parameters are coupled together in Eq. (3.2). If the attenuation constant is first neglected, as f_T becomes larger, β_2 decreases towards zero while the ratio of $\sinh[(\gamma_2 - 2\gamma_1)x/2]/(\gamma_2 - 2\gamma_1)$ approaches its maximum value of $2x$ at $\gamma_2 - 2\gamma_1 \approx 0$. On the contrary, if f_T goes down towards $2f_c(1 + \mathrm{BW}/2)$, although β_2 will approach towards its maximum value of π, the ratio $\sinh[(\gamma_2 - 2\gamma_1)x/2]/(\gamma_2 - 2\gamma_1)$ becomes very small if $(\beta_2 - 2\beta_1)x/2$ is close to integer multiples of π. In fact, the harmonic generated at different stages will begin to add destructively when $(\beta_2 - 2\beta_1)x$ passes π. Similarly, increasing x so that $(\beta_2 - 2\beta_1)x$ goes towards π may help harmonic growth in some cases, but when per-stage attenuation is considered, further increasing x leads to severe penalty of exponential loss. For broadband design, define

$$g(f, f_T, x) = \left| \frac{\gamma_2^2}{\gamma_2 + 2\gamma_1} \frac{\sinh(\frac{\gamma_2 - 2\gamma_1}{2} x)}{\gamma_2 - 2\gamma_1} e^{-\frac{\gamma_2 + 2\gamma_1}{2} x} \right| \tag{3.8}$$

(f_T, x) is chosen so that the minimum value of $g(f, f_T, x)$ over the bandwidth, i.e., $\min\{g(f, f_T, x) | f_L \leq f \leq f_H\}$, is maximized as shown in Fig. 3.2. The inductor at-

tenuation α, which is determined by the quality factor Q, is assumed the same for $m = 1$ and 2 in Fig. 3.2 for simplicity. For printed circuit board (PCB) designs, discrete inductors around a few nH can provide Q larger than 50 around several GHz [34], which results in low loss. However, due to the parasitic in varactor packaging, f_T is often very limited, which constrains optimization of f_T and x. In IC design, f_T is often not a limiting factor below 10 GHz [42, 78], but the inductor Q is limited to around 10 or below. If possible, technology with larger inductor Q and higher varactance b shall be chosen to obtain better harmonic generation efficiency.

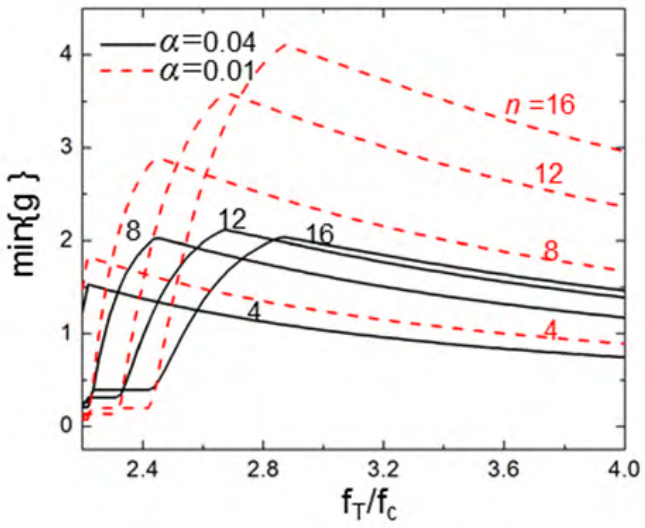

Figure 3.2: $\min\{g(f, f_T, x) | f_L \leq f \leq f_H\}$ versus f_T/f_c when the stage number x (4, 8, 12 and 16) and attenuation per stage vary. BW is set to 20%.

Characteristic impedance Z_0:Z_0 is important for impedance matching. Assuming antennas are designed with input impedance of Z_A (in common practice, Z_A is 50Ω), the reflection coefficient Γcan be expressed as

$$|\Gamma| = \left| \frac{Z_A - Z_B}{Z_A + Z_B} \right| \tag{3.9}$$

From Fig. 3.2, f_T should be chosen not too far from $2f_c(1 + \mathrm{BW}/2)$ to obtain high conversion efficiency. Z_B will drop when frequency moves towards f_T, resulting in poor matching. A good choice of Z_0 should compensate this decrease, as shown in Fig. 3.3. If f_c is close to half of f_T, Z_0 should be slightly larger than Z_A, for say about 1.1 to 1.2 times. Further increasing the characteristic impedance will lead to narrow bandwidth and poor matching at relatively low frequency. For example, when Z_0/Z_A is 1.1, will be less than -25 dB and -15 dB for $f_0 < 0.6f_T$ and $f_0 < 0.8f_T$, respectively.

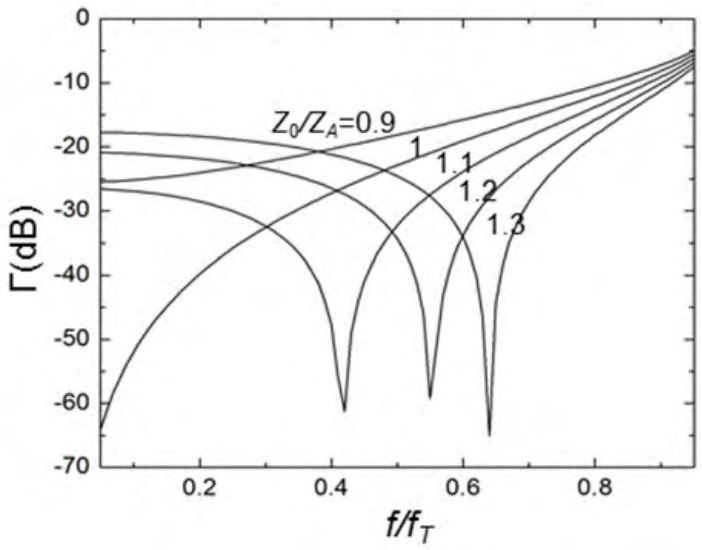

Figure 3.3: Reflection coefficients versus f/f_T for different Z_0/Z_A.

3.1.2 Design Examples

In Table 3.1, four design examples are given. The corresponding second harmonic conversion gains at 0 dBm input power level are given in Fig. 3.4, with both input and

Table 3.1: Design parameters for four NLTL design examples

Design No.	f_c(GHz)	BW(%)	$b(V^{-1})$)	f_T(GHz)	stage number x	α	$Z_0(\Omega)$
1	0.6	20%	0.5	2.2	42	0.01	55
2	1.05	20%	0.5	2.5	6	0.01	55
3	1.05	20%	1.2	2.8	8	0.04	55
4	1.69	90%	1.2	5.8	12	0.04	55

output ports matched at 50Ω. The first two represent the PCB design, where low-loss inductors are usually available ($\alpha = 0.01$). However, due to the parasitics in packaging, the minimum capacitance value and available b are often non-ideal which give small f_T and nonlinearity. With a relatively low fundamental frequency f and a properly chosen f_T, high conversion efficiency can be achieved with large number of x, as in Design #1. However, as f goes up, since f_T is limited, small x has to be chosen in Design #2. Designs #3 and #4 are typical for IC, where low inductor Q leads to much larger loss ($\alpha = 0.04$ as in [45]). However, since varactors have much smaller parasitic capacitance, b can be much larger compared to the PCB design. For example, in IBM 8RF technology, nMOS varactor can offer b as large as $1.5V^{-1}$ [43, 44]. Also f_T can be much larger than that of the PCB design. All four designs show ultra-wideband harmonic generation in the NLTL tag. In first three designs, BW is aimed at 20% and the resulted 3 dB BWs are 40%, 33% and 38%, respectively. In the last design, BW of interest is 90%, and the resulted 3 dB bandwidth is 44% but output second harmonic power difference is within 6.5 dB over the designed 90% bandwidth, which can cover both the 902-928 MHz and 2400-2483 MHz bands regulated by FCC for unlicensed radios simultaneously.

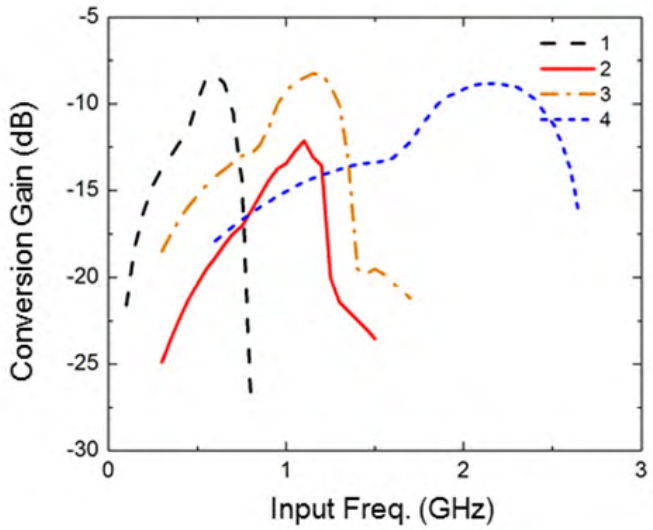

Figure 3.4: Second-harmonic power conversion gain in NLTL sections. The input power is fixed at 0 dBm.

3.2 Reflective NLTL with a single antenna

In order to use a single-antenna configuration, in our implementation, we adopt a reflective structure as depicted in Fig. 3.5. We terminate one terminal of NLTL with an open end and the other terminal with a broadband antenna that covers both fundamental and second harmonic bands. The signal propagates to the end of NLTL and is reflected by the open circuit with a reflection coefficient $\Gamma = 1$. The reflected signal then propagates back towards the tag antenna for backscatter. Reader can find detailed theory of reflected NLTL tag design in [30]

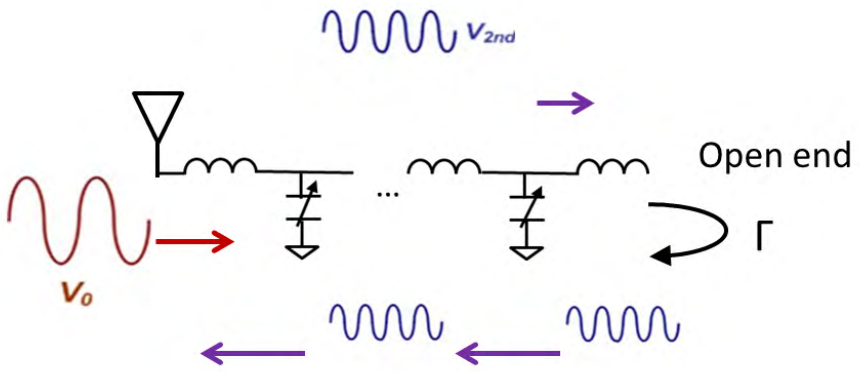

Figure 3.5: Single antenna configuration with open-end NLTL.

3.3 CMOS Compatibility

The proposed design of NLTL based RFID tag is complimentary metal-oxide-semiconductor (CMOS) technology compatible. Current CMOS technology provides good nonlinear varactors and therefore allows efficient broadband harmonic generation in NLTL structure both for matched configuration (a NLTL tag connected to two antennas at its two terminals) and reflected case (only one terminal of NLTL is connected to an antenna while the other terminal is open-ended or short-ended). The CMOS compatibility is important for the eventual low-cost mass production and as a practical platform for the ubiquitous IoT solutions. To verify the CMOS compatibility of NLTLs, we implement on-chip NLTLs with f_T = 10GHz and 15 GHz in the IBM 130nm CMOS process. We fabricated 5-stage 10 GHz open-ended and short-ended NLTLs in IBM 8RF 130nm CMOS process. For comparison, the 10-stage 10 GHz matched NLTLs are also implemented. Fig. 3.6 shows the chip photograph. The core areas are around 0.6mm × 0.35mm for reflective NLTLs and 1.05mm × 0.35mm for matched NLTL, not including

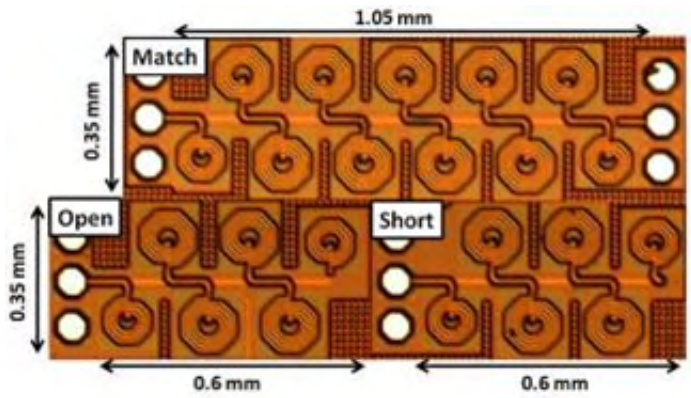

Figure 3.6: Die photo of the 10-stage matched, 5-stage open-ended and 5-stage short-ended NLTLs (f_T = 10 GHz).

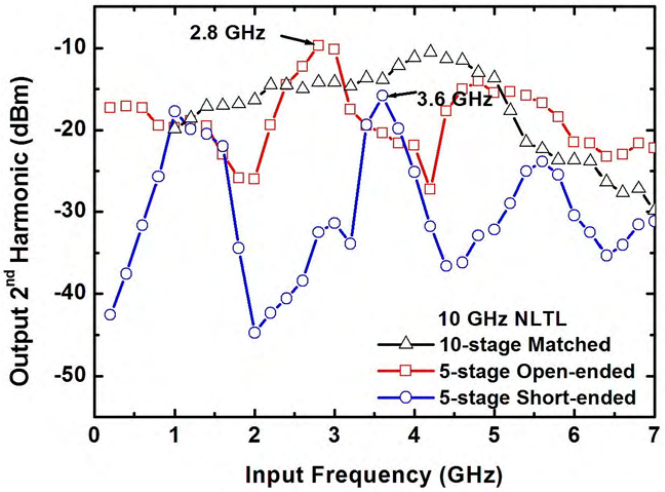

Figure 3.7: Measured output second harmonic power of the 10 GHz 10-stage matched, and 5-stage open-ended and short-ended NLTL with 0 dBm sinusoidal input signal (Pin = 0 dBm).

the RF GSG pads. In all the designs, we use ground-shielded spiral inductors with peak Q around 17 at 10 GHz, respectively. Accumulation-mode nMOS varactors are used in NLTL with minimum-to-maximum capacitance ratio around 3.5. The nominal inductor and capacitor values are shown in Table 3.2.

Fig. 3.7 shows the reflected second harmonic power measured against input frequency. The directional coupler Marki C20-0R612 is used to measure the reflected sig-

Table 3.2: Nominal inductance and capacitance values for the presented NLTLs on IBM 8rf 130nm CMOS process.

Cut-off freq. f_T.	Inductance L(nH)	Capacitance (fF)
10	1.39	530

nals. The NLTLs are excited by a 0 dBm CW RF signal generated by Agilent E8257D. From Fig. 3.7, we can find that the open-ended NLTL achieves maximum harmonic power around -10 dBm as the matched one, while only half of the stages are needed. Comparing the open-ended and the short-ended ones, the open configuration exhibits larger conversion efficiency with Q of NLTL lower than 10, The optimal input frequencies for the 10 GHz open-ended and short-ended NLTLs are around 2.8 GHz and 3.6 GHz, respectively. Both the open-ended design and the matched design can achieve efficient broadband harmonic generation (above -20dBm second harmonic power with 0dBm fundamental signal excitation) over GHz bandwidth.

3.4 Integration with an RFID circuitry

One important question is how we can integrate the NLTL with a normal RFID circuitry. An RFID system consists of a power harvesting unit, a digital control unit and memory logic. When the uplink is modulated on the second harmonic, we need a switch to control the signal flow in NLTL. At the same time, to allow efficient power harvesting to wake up the tag, no power should be spent on harmonic generation during the start-up state. We can achieve the above purposes by adopting a power routing strategy.

We show a design example with the assist of open-platform WISP [47] for the tag

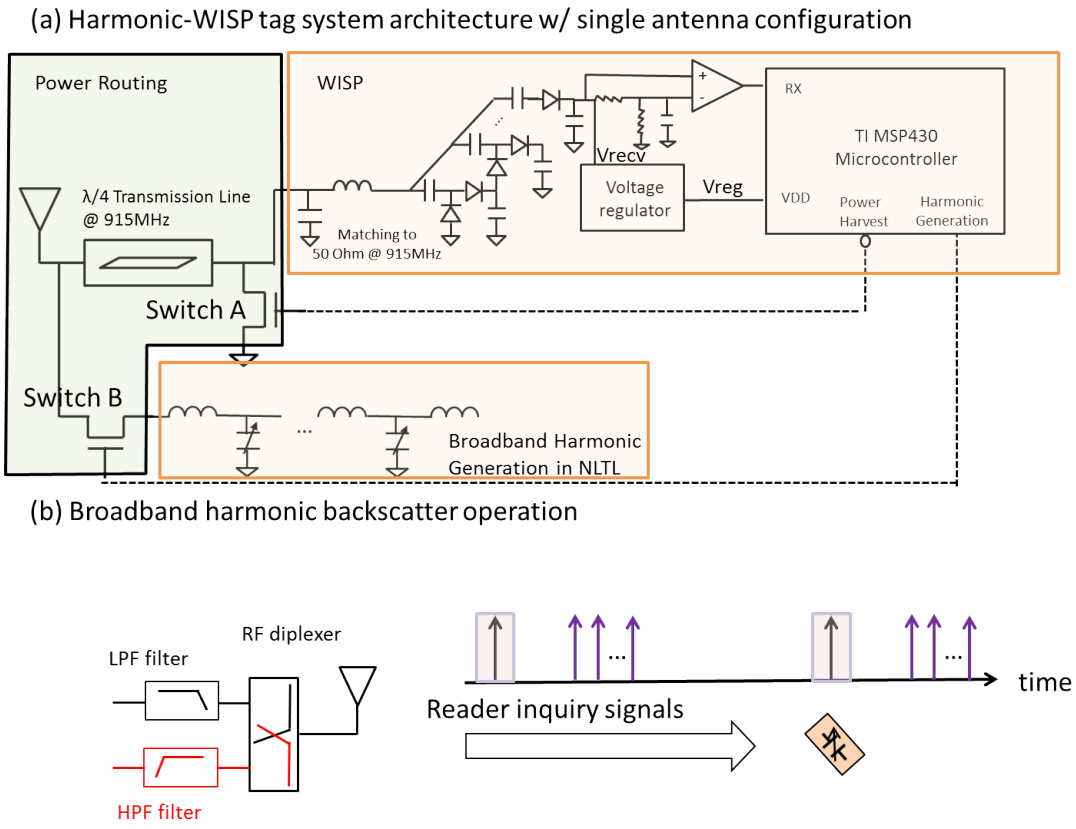

Figure 3.8: (a) System architecture of the proposed Harmonic-WISP RFID tag. (b) An example of reader inquiry signal sequence in the broadband harmonic backscatter operation.

logic circuit part. The proposed system is called the Harmonic-WISP. The tag architecture of Harmonic-WISP is shown in Fig. 3.8. The system consists of three major subsystems: broadband harmonic generation, WISP signal processing, and power routing.

3.4.1 Broadband harmonic generation unit

The broadband harmonic generation unit is built on nonlinear transmission lines (NLTL) which consist of periodically loaded inductors and nonlinear varactors. When the signal

at the fundamental frequency f is routed to NLTL, the second harmonic signal at $2f$ will be generated and propagate along NLTL to the antenna. The characteristic impedance is designed to match 50Ω so that harmonics can be efficiently re-radiated over broadband. The uplink communication is carried on $2f$ using amplitude shift keying (ASK) by turning Switch B in Fig. 3.8(a) on and off.

3.4.2 WISP unit

The WISP unit is based on WISP 5.0 [47]. It performs the functions of energy harvesting, reader command decoding, computation and protocol control. A matching section in the WISP unit is needed to match the input impedance to 50Ω. This is essential for the power routing unit to work properly. Notice that unlike the harmonic generation unit, the WISP power matching is designed around 915MHz in order to achieve good efficiency in the downlink channels. An operation example of broadband Harmonic-WISP is shown in Fig. 3.8(b). Reader emits inquiry signal between 902 to 928MHz when the tag is in the start-up or energy harvesting mode. After the tag harvests enough energy, it can then switch to the harmonic generation mode by the power routing unit. During harmonic generation, the reader can pursue operation with broader bands by sending carrier signals from 700MHz to 1.2GHz. The reader can also opt for a dual-frequency system in addition to the time division.

3.4.3 Power routing unit

The difficult design in a harmonic tag lies on efficient harmonic generation in conjunction with energy harvesting. Harmonic-WISP adopts a novel power routing solution.

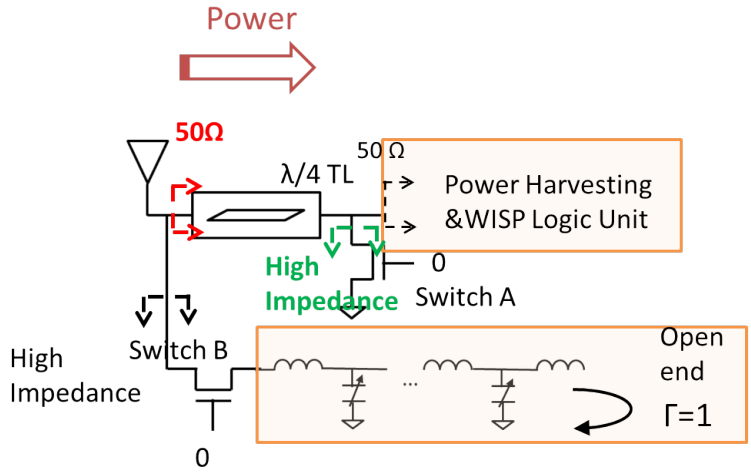

(a) Start-up/ Energy Harvesting

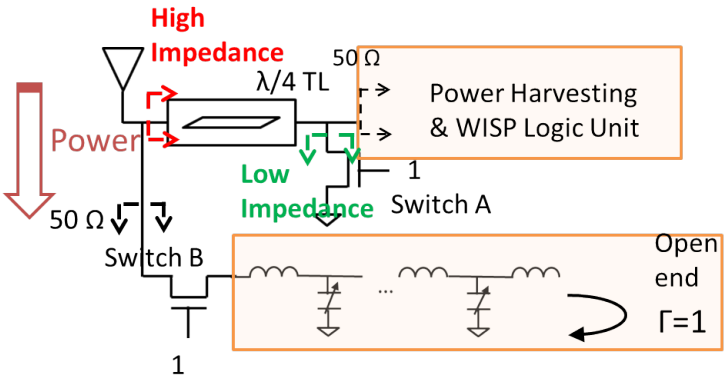

(b) Harmonic generation

Figure 3.9: Power routing in Harmonic-WISP: (a) The start-up/energy harvesting mode; (b) The harmonic generation mode.

The operation of the power routing is depicted in Fig. 3.9. The power routing unit consists of an antenna to receive signals from the reader, a quarter-wavelength ($\lambda/4$) 50Ω meandering micro-strip line, and two RF switches. In the start-up/energy harvesting mode, both Switch A and Switch B are set to off without DC power supply, thus blocking power into NLTL. The WISP power harvesting module is matched to 50Ω and the antenna matching remains after the $\lambda/4$ microstrip line so all power is directed to energy

harvesting. In the harmonic generation mode, both Switches A and B are pulled to the on state. The drain node on Switch A is grounded, and the $\lambda/4$ line acts as an impedance transformer so that a large impedance appears at the input end. Meanwhile, Switch B is also on and impedance looking into NLTL is matched at 50Ω, so all of the received power is routed to generate second harmonics efficiently.

3.4.4 Measurement results

To verify the effectiveness of the proposed system architecture, we prototyped Harmonic-WISP on a printed circuit board as shown in Fig. 3.10(a). The voltage regulator on WISP consisted of a RF to DC converter and a low-dropout (LDO) regulator as the power supply Vreg to the microcontroller MSP430. The voltage regulator Vreg was set to peak at 3.3 V. The measured peak value of Vreg and the tag received power were shown in Fig. 3.10(b).

The second harmonic generation at different frequencies with 0dBm input was measured and shown in Fig. 3.10(c). Harmonic-WISP was able to generate second harmonic above -15dBm from 800MHz to 1100MHz (32% bandwidth). The harmonic RFID system has the noise floor set by the thermal noise, so high receiver sensitivity is enabled in comparison with the conventional RFID system. The reading range limited by reader receiving sensitivity is computed according to the measured harmonic generation characteristics in Fig. 3.10(c) and is shown in Fig. 3.10(d), where the receiver sensitivity at 4W EIRP reader inquiry power is at -100dBm, tag antenna gain at 0dBi, and reader antenna gain at 6dBi. Harmonic-WISP relies on the reader signal from 902MHz to 928MHz to power up the digital circuits. The tag sensitivity limited reading range on 915MHz is also marked in Fig. 3.10(d) which is 4.6 meters. At such range we could

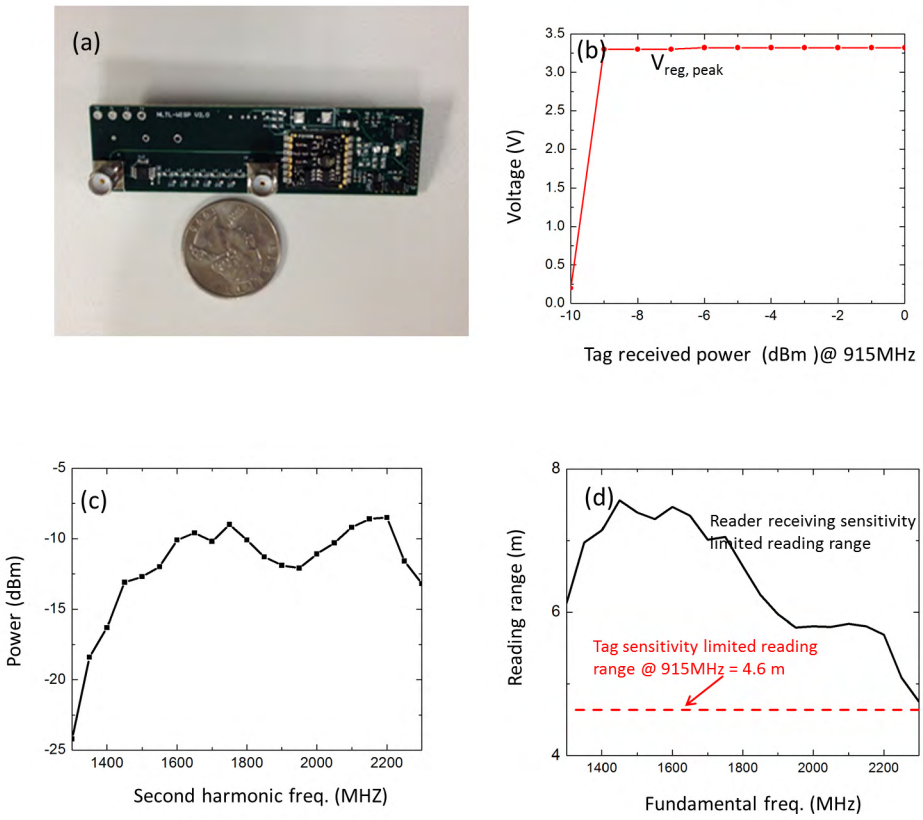

Figure 3.10: Photo of the Harmonic-WISP prototype

pursue a broadband harmonic operating frequency range from 1400MHz to 2400MHz (53% bandwidth). The Smith Chart of the measured input impedance at both energy harvesting and harmonic generation states is shown in Fig. 3.11. Although with small deviation in both inductive and capacitive directions, the overall matching across the operational bandwidth is satisfactory. By our power routing strategy, we were able to fully utilize the received power in both states. To demonstrate the Harmonic-WISP tag data waveforms, decoded reader commands (100Kb/s) from ASK-modulated 915MHz carriers in the downlink measured by oscilloscope were shown in Fig. 3.12(a). The up-link tag second harmonic signals with ASK modulation (150Kb/s) on 1.83GHz were also captured by oscilloscope and shown in Fig. 3.12(b). The measured spectrum of the

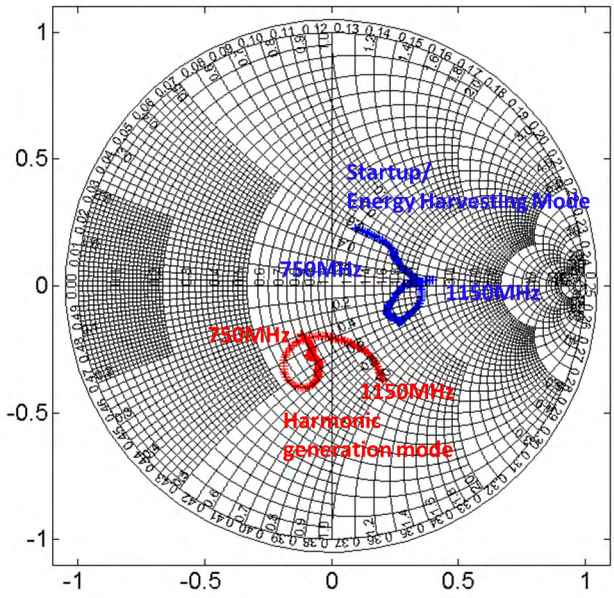

Figure 3.11: Measured input reflection coefficient plotted in Smith Chart for energy harvesting mode and harmonic generation mode.

uplink tag signal for ASK "off"and "on"were shown in Figs. 3.12(c)(d), respectively, at 0dBm input with f_0=915MHz.

3.5 Broadband harmonic reader design for coherent carrier phase detection

With nonlinear backscatter, we can build a reader with broad operation bandwidth. Fig. 3.13 and Fig. 3.14 show the homodyne reader photo and block diagram. Besides the Tx/Rx signal separation block which is illustrated in Fig. 2.4, the reader supports 1 Tx antenna and 4 Rx antennas for 3D locating. The received harmonic signal is directly converted to the baseband and sampled by the analog to digital converter (ADC) on the Cortex M4 STM 32-bit micro-controller. To allow coherent phase detection, the local

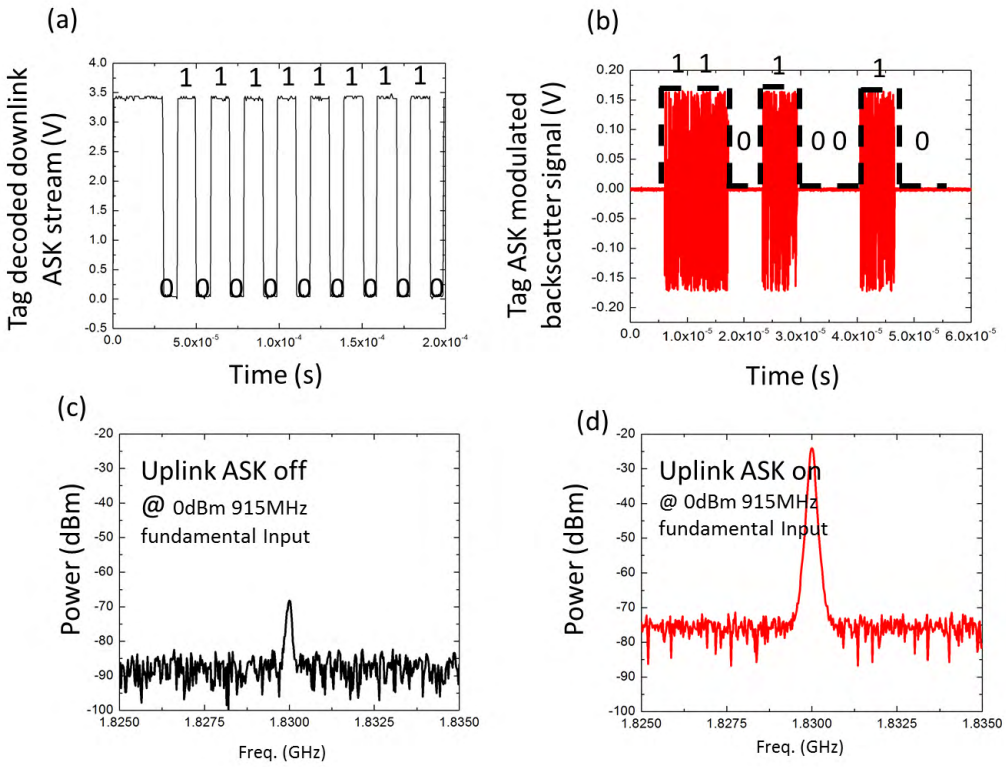

Figure 3.12: (a) Measured Harmonic-WISP decoded downlink bit stream (repeated 1010101010); (b) Measured Harmonic-WISP modulated backscatter signal on second harmonic (bit stream 11010010); (c) Measured spectrum of uplink (ASK off) at 0dBm 915MHz fundamental input; (d) Measured spectrum of uplink (ASK on) at 0dBm 915MHz fundamental input.

oscillator (LO) signal to the mixer is coupled from harmonics of the power amplifier in Tx. The reader employs variable gain amplification in both Tx and Rx to enhance the dynamic range. Our reader can communicate to a host computer by a Bluetooth module. Fig. 3.15 shows the measured maximum Rx gain of our reader. The reader achieve 60dB gain from 1400MHz to 2400MHz for received harmonic signal. The measured Tx output power is 29dBm from 700MHz to 1100MHz as shown in Fig. 3.16. When Tx is at maximum power, the measured interference signal to the receiving chain is also

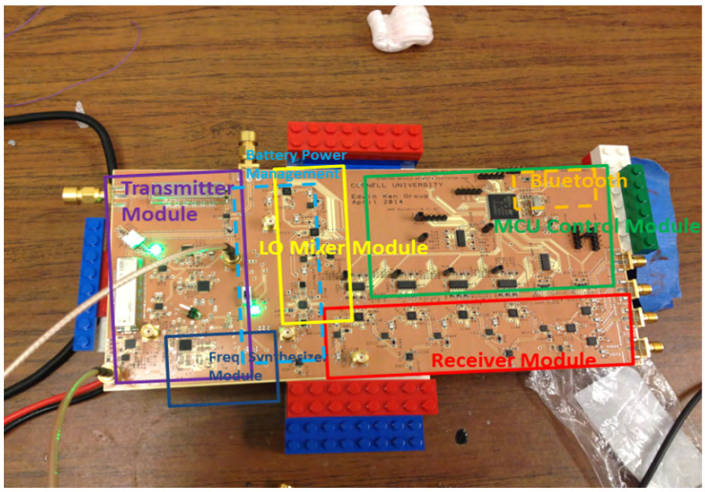

Figure 3.13: Photo of proposed homedyne nonlinear backscatter reader.

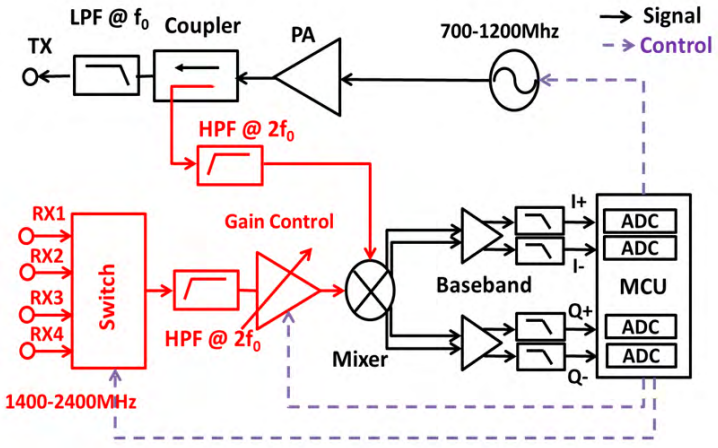

Figure 3.14: Block diagram of reader.

plotted in Fig. 3.16, which is below −90dBm. With the implemented reader, we can pursue a broadband operation over 45% bandwidth.

In comparison to the conventional RFID tranceiving system, the proposed multi-static harmonic tranceiver has the following six merits. (1) Strong interference on interrogating fundamental frequency can be easily filtered out. Thus, in-band interference

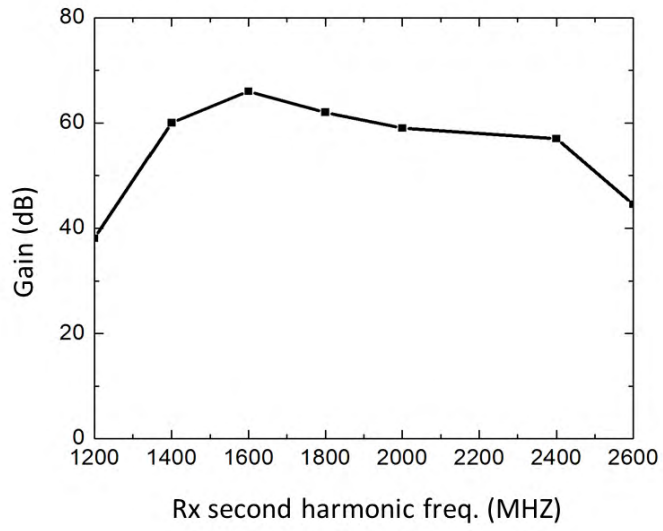

Figure 3.15: Measured reader RX receiving gain in broadband.

cancellation is straightforward and the receiver does not need a large dynamic range. (2) Synchronization is robust as we generate the second harmonic of the local oscillator (LO) to the mixer input directly from the transmitting path as shown in Fig. 3.14. Unlike active-radio locating which needs to generate LO with phase lock loop (PLL) and may lock into other in-band interference signals, our system is much more robust for in-band interference. (3) Constructing a broadband receiving system is more viable due to easy synchronization and the straightforward in-band interference cancellation. (4) In conventional backscattering readers such as Impinj R420 [52], modulation is necessary for separating the useful information from self-leakage, which may introduce an undesirable 180° phase ambiguity for beamforming. We can decode the carrier phase information without modulating the backscatter. Software signal processing gain can be readily added in the microcontroller through averaging. (5) In our system, sensitivity is determined by thermal noise rather than the phase noise around interference. Phase

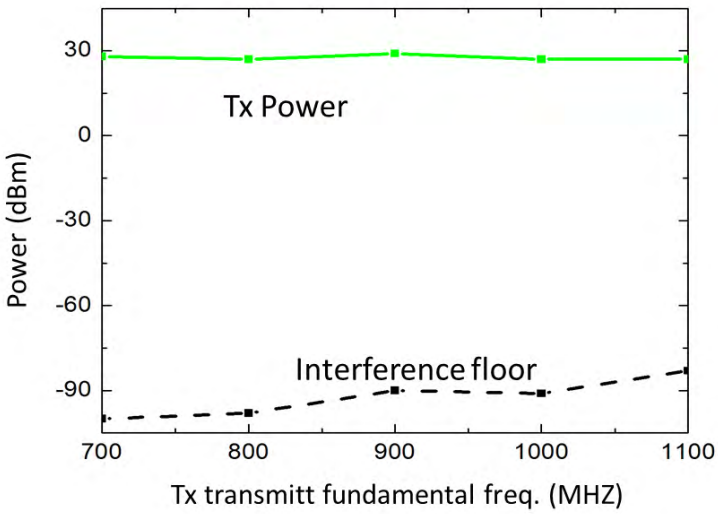

Figure 3.16: Measured maximum reader TX power and corresponding input referred interference in broadband.

decoding can be much more accurate, and we have achieved standard deviation below 0.7° for -60dBm backscatter carrier phase measurements in typical indoor ambient. (6) By multi-static ranging and differential phase of arrival (DPoA), only the multi-path in the uplink matters for ranging. The multi-path signal in the downlink can actually help power transmission. Compared to the mono-static approach in Fig. 2.4, the phase error by the multi-path interference is at least halved.

3.6 Conclusion

In this chapter, we have presented hardware designs for passive harmonic backscatter. As harmonic backscatter techniques can fundamentally eliminate the self-jamming problems in passive RFID system, the system including tag and reader can be designed

to operate in extremely broad bandwidth. As will be discussed later in Chapter 4, such a broadband operation is critical for multi-path phase error tolerance in the proposed HMFCW high accuracy ranging method.

CHAPTER 4

HEURISTIC OPTIMIZED MULTI-FREQUENCY CONTINUOUS RANGING ALGORITHM

A phase-based ranging algorithm needs to accurately resolve ambiguous phase cycle integers with maximum tolerance of phase errors. Traditional multi-frequency ranging based on the Chinese Remainder Theorem (CRT) showed that frequency redundancy can help removing ambiguity [48]. However, CRT-based methods are vulnerable under multi-path phase errors and cannot provide a theoretical phase error bound for correct phase cycle integer estimation. In this chapter, we build the theory of of heuristic optimized continuous wave (HMFCW) ranging. We further generalize two theorems for HMFCW. The two theorems show that in order to tolerate large phase error while solving phase cycle integers correctly, we can rely on optimal utilization of the broad bandwidth which is enabled by our nonlinear backscatter tag and reader design discussed in Chapter 3.

Assume Tx is at the fundamental frequency f_k, the correspondingly measured phase of backscatter second harmonic signal is $\theta_k \in [0, 2\pi)$, the distance from tag to i-th antenna is d_i and the differential distance d_{ij} is

$$d_{ij} = d_i - d_j \tag{4.1}$$

then there is an ambiguous cycle integer n_k for measurements on k-th harmonic frequency which gives

$$d_{ij}^{(k)} = \frac{\theta_k}{2\pi}\frac{\lambda_k}{2} + n_k\frac{\lambda_k}{2} \tag{4.2}$$

where $\lambda_k = c/f_k$ is the wavelength with c equal to the speed of light. Notice that in Eq. (4.2), each cycle is $\lambda_k/2$ instead of λ_k because we compute ranging on the second harmonic corresponding to frequency $2f_k$. Our goal is to correctly computes n_k within a

reading range R, where

$$-R/2 < d_{ij} \leq R/2 \tag{4.3}$$

The typical R for indoor locating is in the range of several meters.

4.1 Error tolerance function

What makes the problem difficult is the large phase error in indoor environment. HMFCW ranging is much more robust than those based on CRT. In HMFCW, a reader transmits a sequence of K frequencies $\mathbf{f} = (f_1, f_2, \cdots, f_K)$ and HMFCW ranging method first defines the **error tolerance** as a function of $\mathbf{f}$ and the reading range R

Definition 1. *Let $\lambda_k = c/f_k$, the error tolerance function is defined as*

$$\begin{aligned} T(\boldsymbol{f}, R) = & \min_{\boldsymbol{b}=(b_1,\cdots,b_K)} \max_{1\leq k,l\leq K} \pi \frac{|\lambda_k b_k - \lambda_l b_l|}{\lambda_k + \lambda_l} \\ s.t. & \begin{cases} b_k \in \boldsymbol{Z}, \quad 1 \leq k \leq K \quad \sum_k b_k^2 > 0 \\ \frac{1}{2}|\lambda_k b_k| < R + \frac{1}{2}\lambda_k \end{cases} \end{aligned} \tag{4.4}$$

Theorem 1. *Let $\Delta\theta_k$ denote the measured phase error for k-th second harmonic frequency and $\Delta\theta_k \in [-\Delta\theta_{max}, \Delta\theta_{max}]$. The measured phase $\theta_k = \theta_k^{ideal} + \Delta\theta_k$, where θ_k^{ideal} is the "ideal" phase when there is no multi-path error. If*

$$\Delta\theta_{max} < T(\boldsymbol{f}, R) \tag{4.5}$$

then we can resolve cycle integers $\boldsymbol{n} = (n_1, n_2, \cdots, n_K)$ correctly by finding the integer vector $\boldsymbol{n}$ that satisfies

$$-R - \lambda_k < n_k\lambda_k \leq R \quad \forall k \tag{4.6}$$

and

$$\frac{2\pi|n_k\lambda_k + \frac{\theta_k}{2\pi}\lambda_k - n_l\lambda_l - \frac{\theta_l}{2\pi}\lambda_l|}{\lambda_k + \lambda_l} < T(\boldsymbol{f}, R) \quad \forall k, l \tag{4.7}$$

Proof. Assume the actual distance is d which is also the distance by θ_k^{ideal}. Because for k-th frequency, we have phase error $\Delta\theta_k$, so the measured distance $d^{(k)}$ for k-th frequency is

$$d^{(k)} = d + \frac{\Delta\theta_k}{2\pi}\frac{\lambda_k}{2} = \frac{n_k\lambda_k}{2} + \frac{\theta_k}{2\pi}\frac{\lambda_k}{2} \tag{4.8}$$

where $\mathbf{n} = (n_1, \cdots, n_k, \cdots, n_K)$, $k \in \{1, \cdots, K\}$ are the true integers that we want to compute. Because of Eq. (4.2) and Eq. (4.3), we have

$$-\frac{R}{2} < \frac{n_k\lambda_k}{2} + \frac{\theta_k}{2\pi}\frac{\lambda_k}{2} \leq \frac{R}{2} \tag{4.9}$$

and $0 \leq \theta_k < 2\pi$. Hence n_k satisfies Eq. (4.6). Because of Eq. (4.8), we have

$$|d^{(k)} - d^{(l)}| = |\frac{\Delta\theta_k}{2\pi}\frac{\lambda_k}{2} - \frac{\Delta\theta_l}{2\pi}\frac{\lambda_l}{2}| < \frac{\Delta\theta_{\max}}{2\pi}\frac{\lambda_k + \lambda_l}{2} \tag{4.10}$$

By using Eqs. (4.5) (4.8) and (4.10), we know n_k and n_l where $k, l \in \{1, \cdots, K\}$ satisfy Eq. (4.7) and therefore, the true $\mathbf{n}$ is a solution that satisfies the condition in Eqs. (4.6) and (4.7).

Next, we will prove that $\mathbf{n}$ is the unique solution by contradiction. Suppose there is another solution $\tilde{\mathbf{n}} = \mathbf{n} + \mathbf{b}$. Since both $\mathbf{n}$ and $\tilde{\mathbf{n}}$ satisfy Eq. (4.6), integer b_k must satisfy $\frac{1}{2}|\lambda_k b_k| < R + \frac{1}{2}\lambda_k$ and because $\tilde{\mathbf{n}} \neq \mathbf{n}$, $\sum b_k^2 > 0$. Since both $\mathbf{n}$ and $\tilde{\mathbf{n}}$ satisfies Eq. (4.7), this leads to:

$$\frac{\pi|b_k\lambda_k - b_l\lambda_l|}{\lambda_k + \lambda_l} < T(\mathbf{f}, R) \quad \text{for} \quad \forall\ 1 \leq k, l \leq K \tag{4.11}$$

Eq. (4.11) contradicts with the definition of $T(\mathbf{f}, R)$ in Eq. (4.4). Therefore, the desired integer $\mathbf{n}$ is the unique solution that satisfies condition in Eqs. (4.6) and (4.7). □

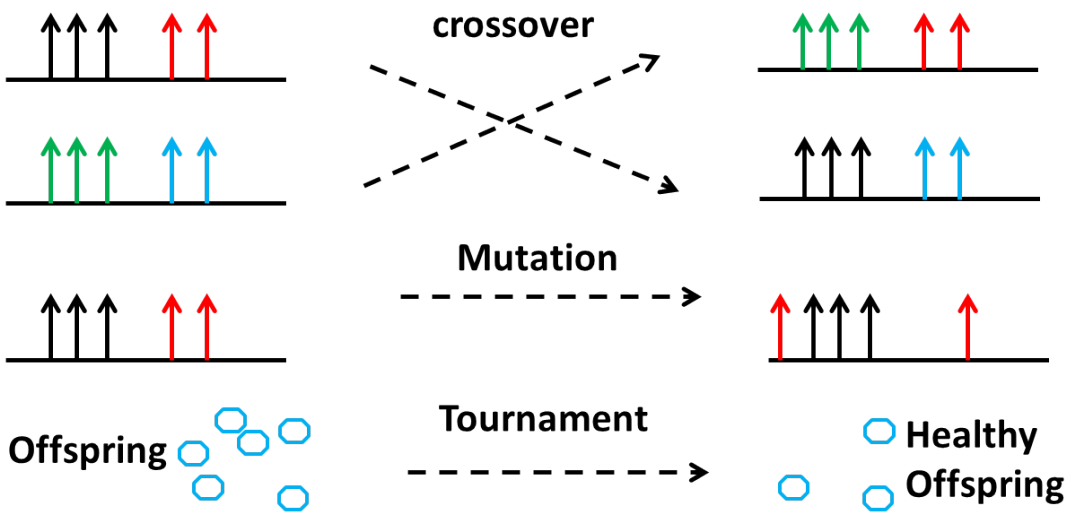

Figure 4.1: Selecting optimal freq. combination with small number of freq. via genetic algorithm

4.2 Selecting optimal frequency combination via Genetic Algorithm

As long as the measured phase error is smaller than $T(\mathbf{f}, R)$ in Eq. (4.4), we can resolve cycle integers correctly. We now need to select a frequency combination that can maximize the error tolerance function $T(\mathbf{f}, R)$. The maximum value of $T(\mathbf{f}, R)$ is defined as the **phase error threshold** Φ:

Definition 2. *Definition The phase error threshold:*

$$\Phi(\boldsymbol{F}, K, R) = \max_{\boldsymbol{f}=(f_1,\cdots,f_K)} T(\boldsymbol{f}, R) \tag{4.12}$$

where $\mathbf{F}$ represents the bandwidth of operation and K is the number of frequencies used for ranging. Assume $f_{\max} = \max\{f, f \in \mathbf{F}\}$ and $f_{\min} = \min\{f, f \in \mathbf{F}\}$ are the maximum and minimum frequencies in $\mathbf{F}$, We define the percentage bandwidth as

$$\mathrm{BW}\% = 2\frac{f_{\max} - f_{\min}}{f_{\max} + f_{\min}} \tag{4.13}$$

Theorem 2. *Theorem An integer $K(\boldsymbol{F}, R)$ exists for a continuous frequency band $\boldsymbol{F}$ with $BW\% < 100\%$ and a reading range R so that for $K > K(\boldsymbol{F}, R)$, an optimal frequency combination $\boldsymbol{f}^{opt} = (f_1^{opt}, f_2^{opt}, \cdots, f_K^{opt})$ can be found for which*

$$\Phi(\boldsymbol{F}, K, R_{max}) = T(\boldsymbol{f}^{opt}, R) = 90^\circ \times BW\% \tag{4.14}$$

Proof. First note that

$$\begin{aligned} T(\mathbf{f}, R) &\leq \min_{\mathbf{b}=(1,\cdots,1)} \max_{1\leq k,l\leq K} \pi \frac{|\lambda_k b_k - \lambda_l b_l|}{\lambda_k + \lambda_l} \\ &\leq \pi \frac{\lambda_{max} - \lambda_{min}}{\lambda_{max} + \lambda_{min}} = 90^\circ \times \mathrm{BW}\% \end{aligned} \tag{4.15}$$

so we only need to prove that the upper bound is attainable. Without loss of generality, assume $f_1 > f_2 > \cdots > f_K$. For $\mathbf{b} \neq \mathbf{0}$, define

$$t(\mathbf{f}, \mathbf{b}) = \max_{i,j} \pi \frac{|\lambda_i b_i - \lambda_j b_j|}{\lambda_i + \lambda_j} \tag{4.16}$$

for the integer vector $\mathbf{b}$

Case 1: there exist a pair of b_i and b_j $(i \neq j)$ that have different signs. Then it is easy to see that $t(\mathbf{f}, \mathbf{b}) \geq \pi$

Case 2: all elements in $\mathbf{b}$ are not in decreasing order when non-negative or not in increasing order when non-positive. For $r < s$, there exists $0 \leq b_r < b_s$ or $b_s < b_r \leq 0$. Then since $\lambda_r < \lambda_s$,

$$t(\mathbf{f}, \mathbf{b}) \geq \pi \frac{|b_s - b_r|\lambda_s + |b_r|(\lambda_s - \lambda_r)}{\lambda_r + \lambda_s} > \frac{\pi}{2} \tag{4.17}$$

Case 3: all elements in b are equal and non-zero, $b_1 = b_2 = \cdots = b_K \neq 0$. Then,

$$t(\mathbf{f}, \mathbf{b}) = \pi |b_1| \frac{\lambda_K - \lambda_1}{\lambda_K + \lambda_1} > \pi \frac{\lambda_K - \lambda_1}{\lambda_K + \lambda_1} \tag{4.18}$$

The equality holds when $b_1 = \pm 1$.

Case 4: elements in $\mathbf{b}$ are non-negative and in decreasing order but not equal, $b_1 \geq b_2 \cdots \geq b_K \geq 0$, so there mush exist r, such that $b_r > b_{r+1} \geq 0$, or elements in $\mathbf{b}$ are non-positive and in increasing order but not equal, $b_1 \leq b_2 \cdots \leq b_K \leq 0$, so there mush exist r, such that $b_r < b_{r+1} \leq 0$, Then

$$t(\mathbf{f}, \mathbf{b}) \geq \pi \frac{\lambda_r - M(\lambda_{r+1} - \lambda_r)}{\lambda_{r+1} + \lambda_r} \tag{4.19}$$

where $M = \lceil \frac{2R}{\lambda_{\min}} \rceil + 1$. Thus,

$$T(\mathbf{f}, R) \geq \min \left\{ \pi \frac{\lambda_K - \lambda_1}{\lambda_K + \lambda_1}, \pi \frac{\lambda_r - M(\lambda_{r+1} - \lambda_r)}{\lambda_{r+1} + \lambda_r} \right\} \tag{4.20}$$

Consider a special frequency combination

$$f_k{}^T = f_{\max} \left(\frac{f_{\min}}{f_{\max}} \right)^{\frac{k-1}{K-1}} \qquad 1 \leq k \leq K \tag{4.21}$$

as long as

$$K > \left\lceil \log_{\frac{M+1-0.5\mathrm{BW}\%}{M+0.5\mathrm{BW}\%}} \left(\frac{1 + 0.5\mathrm{BW}\%}{1 - 0.5\mathrm{BW}\%} \right) \right\rceil + 1 \tag{4.22}$$

It can be shown that

$$\pi \frac{\lambda_r{}^T - M(\lambda_{r+1}{}^T - \lambda_r{}^T)}{\lambda_{r+1}{}^T + \lambda_r{}^T} \geq \frac{pi}{2} \mathrm{BW}\% \tag{4.23}$$

And thus,

$$T(\mathbf{f}^T, R) \geq 90^\circ \times \mathrm{BW}\% \tag{4.24}$$

Consider case 1 to 4 and Eq. (4.15), with $\mathrm{BW}\% < 1$, we have $T(f, R) = 90^\circ \times \mathrm{BW}\%$. □

Theorem 2 dictates that we can always find an optimal frequency combination in a continuous frequency band so that our error tolerance is maximized. The maximum error toleration is equal to $\mathrm{BW}\% \times 90^\circ$. The larger the operation bandwidth we have, the more robust we are to the multi-path induced phase error. For example, if we have a system with percentage bandwidth of 50%, we can tolerance phase error from -45° to 45° with 100% reliable cycle integer calculation. Although Eq. (4.21) gives an optimal

solution, however, it is pessimistic when considering the number of frequency required to meet the upper bound. Usually, the upper bound can be achieved with less than 6 frequencies for reading range about 4 meter and 30% bandwidth.

A heuristic optimization program can be employed to find the optimal frequency combination with small number of frequencies. In our case, we choose the genetic algorithm (GA) which utilizes three mechanisms: crossover, mutation and tournament. At the start, we randomly select a poll of frequency combinations. Then these frequency vectors mate with each other to produce offspring with a mutation probability. The next generation is then generated by selecting healthy offsprings ny comparing the cost function $T(\mathbf{f}, R)$ through a tournament. This process is briefly illustrated in Fig. 4.1. After pinning down the optimal frequency combination, ranging can be performed using Algorithm 1.

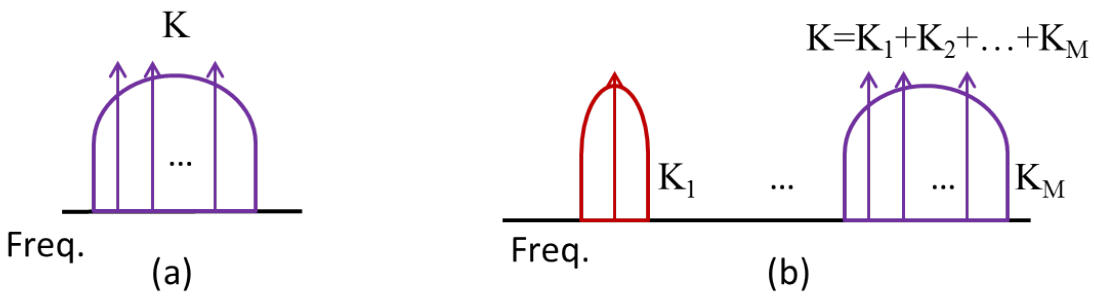

Figure 4.2: HMFCW ranging: (a) single-band and (b) multi-band operations.

4.3 HMFCW in single-band operation

The operation of the proposed HMFCW is very flexible. It can be applied for both single-band and multi-band operations as shown in Fig. 4.2. For single band operation, the actual minimum number of frequencies $K(\mathbf{K}, R)$ needed is usually much smaller than

Algorithm 1: HMFCW ranging with optimal frequency combination

Inputs: wavelength for **optimal** frequency combination $\lambda_1 > \lambda_2 > \cdots > \lambda_K$, measured phase $(\theta_1, \theta_2, \cdots, \theta_K)$, reading range R

Outputs: distance d

$\Phi = 2\dfrac{\lambda_1 - \lambda_K}{\lambda_1 + \lambda_k}\dfrac{\pi}{2}$ ▷ compute phase error threshold

$N_{\max} = \dfrac{R}{\lambda_K} + 1$ ▷ compute the range of cycle integer for λ_K

while Iter $\leq$ MaxIter **do**

  for $n_K = -N_{\max} \rightarrow N_{\max}$ **do**

    $d_{\text{temp}} = n_K\dfrac{\lambda_K}{2} + \dfrac{\theta_K}{2\pi}\dfrac{\lambda_K}{2}$

    for $i = 1 \rightarrow K-1$ **do**

      $n_i = round\left(\dfrac{d_{temp} - \frac{\theta_i}{2\pi}\frac{\lambda_i}{2}}{\frac{\lambda_i}{2}}\right)$

    end for

  end for

  if $\dfrac{\pi|n_i\lambda_i + \frac{\theta_i}{2\pi}\lambda_i - n_j\lambda_j - \frac{\theta_j}{2\pi}\lambda_j|}{\lambda_i + \lambda_j} < \dfrac{\Phi}{2}$ for $\forall i, j$ **then**

    Break ▷ solution found

  end if

  $\Phi = \tau\Phi$ ▷ if no solution found, relax phase error threshold

end while

$d = \dfrac{1}{K}\sum_{i=1}^{K}\left(\dfrac{\lambda_i}{2}n_i + \dfrac{\theta_i}{2\pi}\dfrac{\lambda_i}{2}\right)$ ▷ compute average

the right hand side of Eq. (4.22). As shown in Fig. 4.3, for sensing range R less than 100 times of transmitting wavelength, only a small number of frequencies are needed to attain the optimal threshold. HMFCW ranging performance simulated by Monte Carlo is shown in Fig. 4.4 and Table I (Cases 1 to 3). Phase error is assumed uniformly distributed within $[-\Delta\theta_{\max}, \Delta\theta_{\max}]$ and uncorrelated for different frequencies. HMFCW ranging maintains sub millimeter accuracy for phase error below threshold in Eq.(4.14).

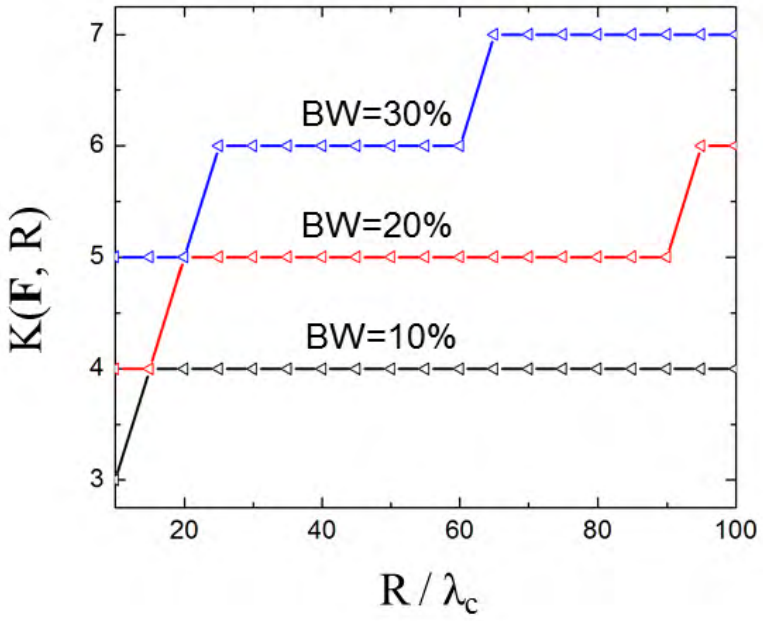

Figure 4.3: The minimum number of frequencies $K(\mathbf{F}, R)$ needed for $\Phi(\mathbf{F}, K, R)$ to reach $\pi \mathrm{BW}/2$. λ_c is the wavelength of the center frequency f_c in $\mathbf{F}$.

Table 4.1: Optimized frequency selection samples for single-band/dual-band operation

Case No.	Number of freq.	Freq. (MHz)	BW(BW1,BW2)%	Phase error threshold Φ	Reading range R
1	4	950,968,1014,1050	10%	9°	3 m
2	5	900,945,1007,1012,1100	20%	18°	3 m
3	5	850,916,1113,1125,1150	30%	27°	3 m
4	5	910,928,2400,2461,2474	92%(2%,3%)	21°	3 m
5	6	2400,2450,2475,5749,5759,5875	84%(3%,2%)	18°	3 m

4.4 HMFCW in multi-band operation

The HMFCW can also be applied to multi-band operation thanks to the broadband property of NLTLs as shown in the design example in Chapter 3. Assume totally M bands are used and then $\mathbf{f}$ can be expressed as $(\mathbf{f}_1, \mathbf{f}_2, \cdots, \mathbf{f}_K)$ with the p-th element in $\mathbf{f}_i$, denoted

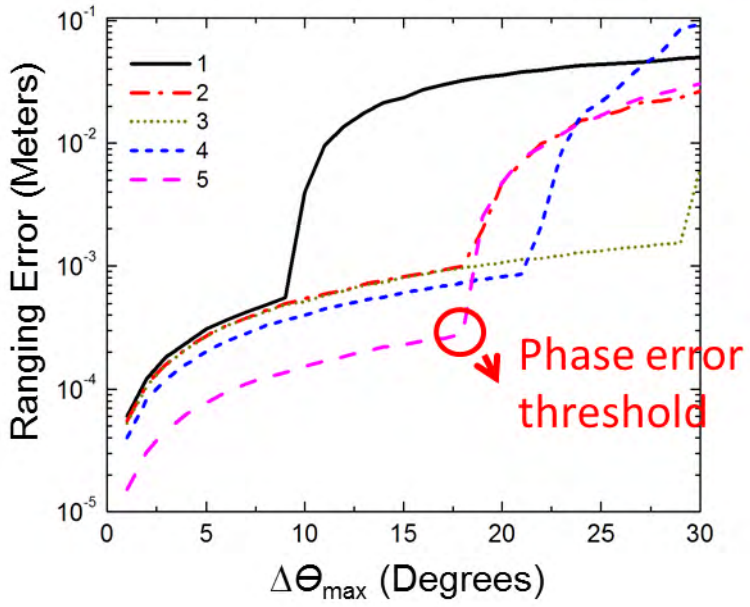

Figure 4.4: HMFCW averaged ranging error versus maximum phase error by Monte Carlo simulation for single-band and dual-band operations of the five cases in Table 4.1. Phase error is uniformly distributed within $[-\Delta\theta_{\max}, \Delta\theta_{\max}]$.

as $f_p{}^i$, confined by the i-th frequency band, as shown in Fig. 4.2(b). The multi-band operation does not require large bandwidth in each band but can allow large maximum phase error threshold Φ. The multiband operation is the same as single band operation in its algorithm but can bring two advantages due to its flexibility in making use of the spectrum resource more efficiently:

(i) It can be optimized into unlicensed frequency bands.

(ii) It can take advantage of dynamic spectrum management to help increase phase error tolerance by accessing an additional unoccupied band.

For simplicity, the feasibility of dual-band operation is investigated only with sim-

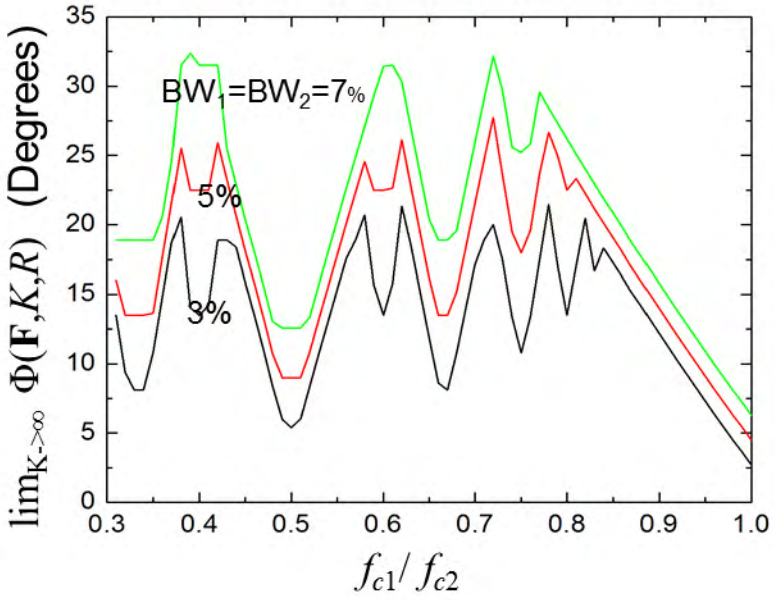

Figure 4.5: Relationship between the phase error threshold Φ and the center frequency when the number of frequencies is not limited. $R/\lambda_{c2} = 25$.

ulation results. The relationship between $\lim_{K\to\infty}(\mathbf{F}, K, R)$ and different operation band combinations is shown in Fig. 4.5. f_{c1} and f_{c2} are center frequency of the first and second bands, respectively. R is equal to $25\lambda_{c2}$. Dual-band operation provides much larger Φ than that by single band with the same bandwidth ($f_{c1}/f_{c2} = 1$ as the single-band case). Fig. 4.6 shows Φ with small number of frequencies and different R when BW1=BW2=5%. Similar to single-band operation, dual-band operation does not need large number of frequencies to achieve high performance for a decent sensing range. Examples of dual-band HMFCW performance are also shown in Fig. 4.4 (Cases 4 and 5 in Table 4.1), which exhibits robustness against large phase errors in preserving millimeter accuracy. The special property of NLTL tag can work over 90% BW without dropping too much conversion efficiency, which makes the dual-band approach very feasible. When operating in dual-band mode, wideband or multiband antennas can be

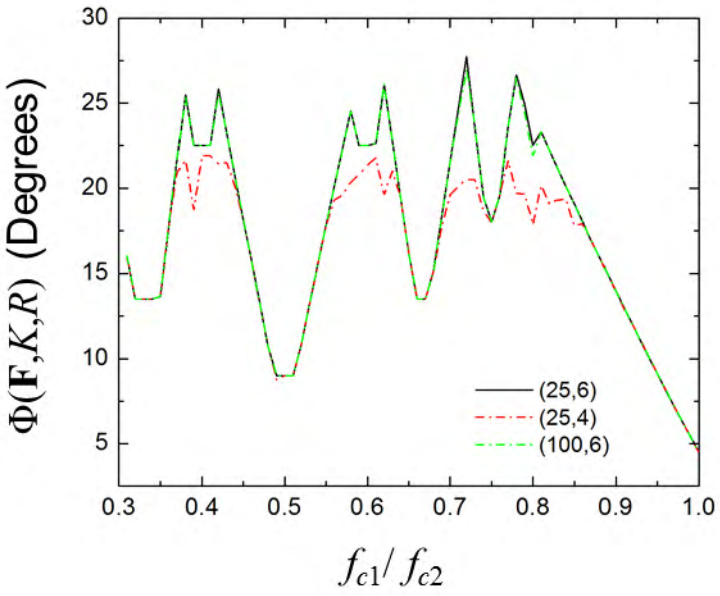

Figure 4.6: Relationship between Φ and center frequencies selection with small number of frequencies and different Rmax denoted as $(R/\lambda_{c2}, K)$. BW1=BW2=5% in simulation. Number of frequencies in each band are same, all equal to K/2.

applied, such as in [53], where a triple band antenna is designed to facilitate power harvesting at 900 MHz, 1900 MHz and 2400 MHz.

4.5 Conclusion

In this Chapter, we present the theory and algorithm implementation of HMFCW ranging method. HMFCW ranging maximally utilizes given bandwidth resources with optimized frequency combination to provide the highest achievable phase error tolerance when resolving ambiguous phase cycle integers. Through the use of heuristic optimization, the required number of frequency is small and the HMFCW ranging is highly flex-

ible which can be applied to both single frequency band and multiple frequency bands operations. For single frequency band operation, HMFCW ranging calculates phase cycle integer with 100% reliability when the phase error is within $90^o \times \mathrm{BW}\%$.

CHAPTER 5

REAL-TIME 3D LOCATING BY BROADBAND HARMONIC BACKSCATTER

We have discussed accurate ranging in previous chapter. To achieve 3D locating, we need at least 4 antenna to uniquely pin down the target tag locating. In this Chapter, we discuss real-time 3D locating based on the broadband harmonic backscatter system and HMFCW ranging algorithm.

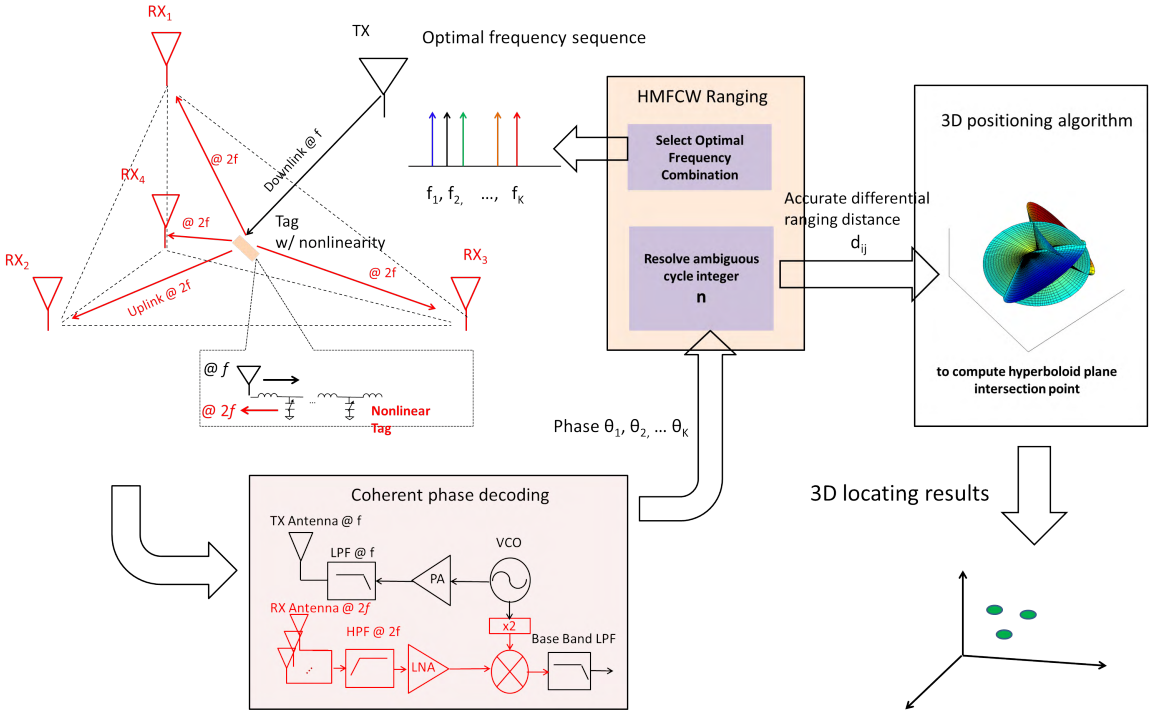

Figure 5.1: Illustration of the passive nonlinear backscatter real-time 3D locating system.

5.1 System overview

The proposed nonlinear backscatter locating system is shown in Fig. 5.1. The function of the system is to determine the 3D location of a passive tag that is able to generate harmonics when impinged by reader inquiry signal. The system consists of four main sub-systems: (1) Phase information acquisition; (2) Coherent phase detection; (3) Heuristic multi-frequency continuous wave ranging; (4) 3D positioning algorithm.

The phase information acquisition subsystem consists of 1 broadband transmitting antenna at the fundamental frequency and 4 receiving antennas at the corresponding second harmonics. When the nonlinear tag has received the inquiry signal from the Tx antenna, it responds to the 4 receiving antennas by re-radiating the second harmonic signals. The system later computes the differential distance from the tag to different receiving antennas in order to pin down its accurate position.

The phase detection subsystem utilizes a homodyne receiver to directly covert the backscatter harmonic signal to baseband and compute the the carrier phase. One fundamental advantage of RFID positioning is coherent detection without carrier offset between the transmitting and receiving signals. This remains true when we use nonlinear backscatter for the round trip. Becaise the uplink harmonic signal is passively generated from reader inquiry signal on tag, we are able to coherently detect the carrier phase by utilizing harmonics generated in the TX chain.

The heuristic multi-frequency continuous-wave ranging sub-system has two functions. It first decides what are the frequencies to transmit based on the available bandwidth. The transmitting frequency sequence is very important to resolve the ambiguous phase cycles reliably in HMFCW ranging. After receiving the decoded harmonic carrier phase the cycle integer for each frequency is calculated. The final output is the differen-

Table 5.1: Optimal Tx frequency combination used in the real-time 3D locating experiment

Number of freq.	Freq. (MHz)	BW%	Phase error threshold Φ	Reading range R
8	721 750 829 889 950 996 1045 1060	38%	34°	4 m

tial distance from the tag to receiving antennas d_{ij}, where $d_{ij} = d_i - d_j$, with d_i being the distance from tag to the i-th receiving antenna.

The last part is the 3D positioning computation. Each differential distance d_{ij} determines a hyperboloid in the 3D space. In order to uniquely determine the 3D position, we need to compute the intersection point of at least 3 hyperboloids. We convert such a task into an optimization problem and utilize the efficient nonlinear conjugate gradient search.

5.2 Frequency selection

In this work, we pick an optimal frequency combination by HFMCW shown in Table. 5.1 which achieves phase error threshold of 34°. Fig. 5.2 shows the simulated ranging results for median, mean and max errors for a reading ranging R of 4 meters. The phase error for each frequency is uniformly distributed within $[-\Delta\theta_{\max}, \Delta\theta_{\max}]$. We can achieve median ranging error below 1cm even when $\Delta\theta_{\max} = 50°$.

5.3 3D locating algorithm

In the previous sections, we have discussed the robust and accurate HMFCW ranging. Since each ranging result is a differential distance from a tag to two antennas at differ-

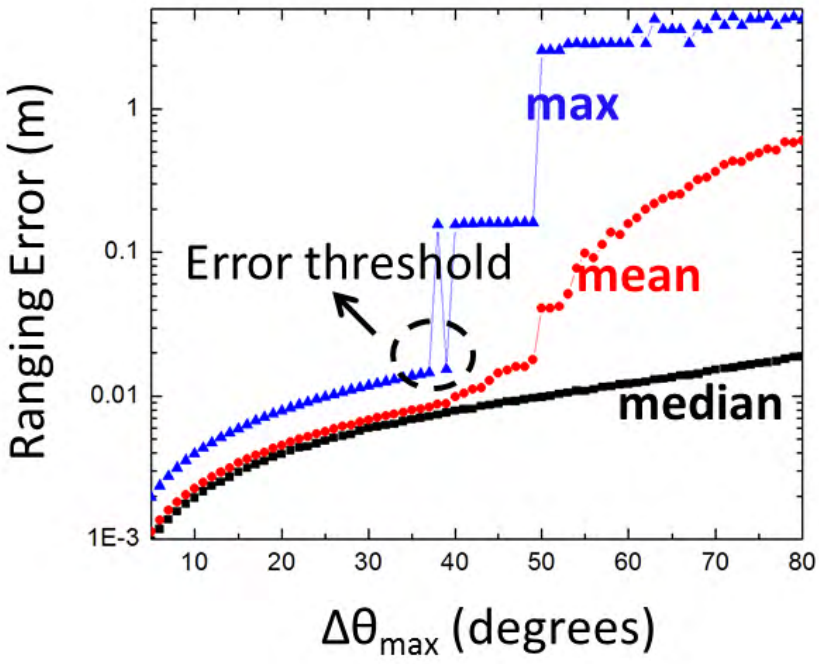

Figure 5.2: Ranging error simulated from Monte Carlo simulation using frequencies shown in Table.5.1

ent position, in 3D space, one differential distance measurement gives a hyperboloid as shown in Fig. 5.3(a). To uniquely pin down a tag position in 3D, at least three hyperboloid are required to compute the intersection point as depicted in Fig. 5.3(b).

We achieve such task by solving the following optimization problem

$$\min_{\mathbf{p}} \sum_{i=2}^{4} \left(|\mathbf{p} - \mathbf{p}_1^{\text{ant}}| - |\mathbf{p} - \mathbf{p}_i^{\text{ant}}| - d_{1i} \right)^2 \tag{5.1}$$

where, the target tag position is denoted as $\mathbf{p} = (x, y, z)$ and the i-th antenna position is $\mathbf{p}_i^{\text{ant}}$. The problem is essentially a nonlinear optimization problem. We solve it efficiently with the Fletcher-Reeves nonlinear conjugate gradient (CG) method [80].

CG is different from gradient descend algorithm which is most popular and widely

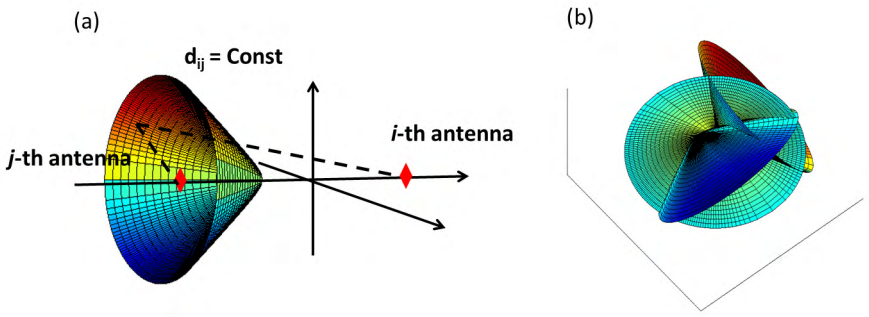

Figure 5.3: 3D locating by solving hyperboloid intersection

used. In gradient method, for every step we take the gradient as the steepest descending direction. However, this choice is only local optimal and may not be efficient through the whole optimization process. As a results, in gradient method, we may go into the same descending directional over and over again and thus lose efficiency. On the other hand, CG selects search direction by finding M vectors that are A-orthogonal in a M-dimension space, where A is the local Hessian matrix of the objective function in Eq. (5.1). If the problem can be well approximated by the taylor expansion to the second order, CG can quickly find the optimal solution within about M steps.

Fletcher-Reeves nonlinear (CG) can be trapped with local minima. To avoid such a problem, we select the initial point $\mathbf{p}_0$ from a poll of 300 randomly generated initial points fir a comprehensive search.

$$\mathbf{p}_0 = \min_{\mathbf{p}\in\{\mathbf{p}_0^{(1)},\cdots,\mathbf{p}_0^{(300)}\}} \sum_{i=2}^{4} \left(|\mathbf{p}-\mathbf{p}_1^{\text{ant}}| - |\mathbf{p}-\mathbf{p}_i^{\text{ant}}| - d_{1i}\right)^2 \tag{5.2}$$

5.3.1 Locating error from ranging errors and RX antenna phase center uncertainties

For 3D locating error, there are two main error sources. The first error source comes from the ranging measurement error while the second error is from the uncertainty in the phase center position of the 4 Rx antennas. The ranging error Δd_{1i} is introduced from

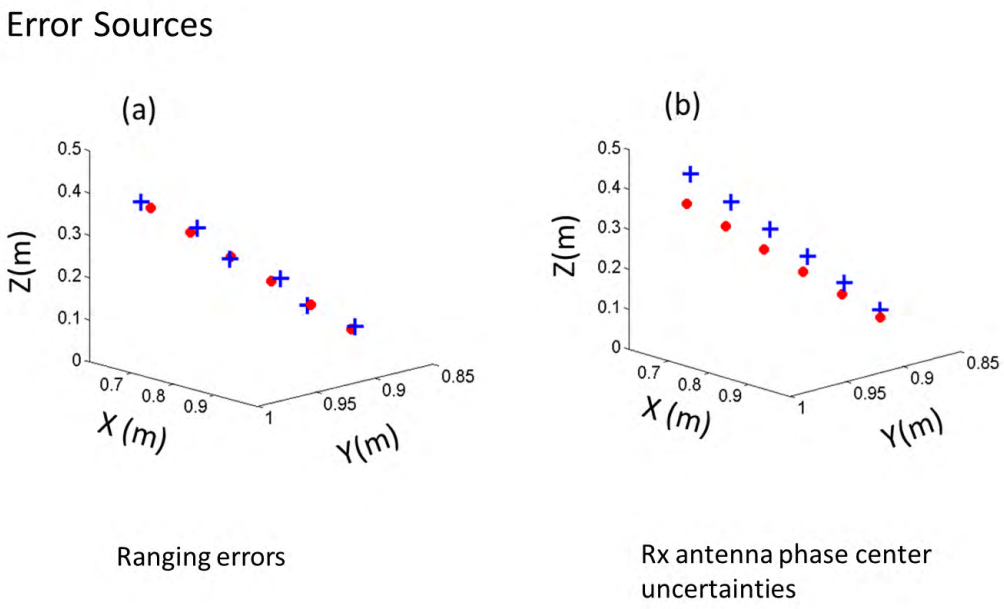

Figure 5.4: Locating errors from (a) ranging error. (b) antenna phase center uncertainties.

both multi-path induced phase error and noise induced phase error. For the proposed approach, unlike the conventional backscatter system where the noise floor is set by phase noise in the leakage signal, the noise floor is determined by the thermal noise. Based on our testing as will be discussed later, thermal noise induced phase errors are usually very small and typically within $\pm 1^{\circ}$. Compared to noise induced ranging error,

multi-paths induced phase error is much larger and typically distributed within ±60°. Multi-paths is very sensitive to tag location so the effect of multi-path introduces 3D locating errors that looks noise-like when we consider different positions in the space as shown in Fig. 5.4(a).

The effect of antenna phase center position error $\Delta\mathbf{p}_i^{ant}$ [58] introduces an error effect that is more like an offset or distortion compared the noise-like ranging error as shown in Fig. 5.4(b). The phase center uncertainty arises from the fact that, for an antenna, the signal receiving center is not necessarily the same as antenna geometry center. In fact, the signal receiving center could be dependent on the angle of arrival of the received signal [81]. In order to minimize such distortion, the antenna phase center needs to be measured as accurate as possible. However an antenna phase center error of ±3 cm is typical. In this work, since we can directly resolve the ambiguous phase cycle integer even under large phase error, the ranging error is typically in the range of millimeter level, the major locating error is contributed from the antenna phase center uncertainties.

5.4 Experimental Evaluation

We evaluate the the proposed approach through intensive experimental measurements in indoor environments as shown in Fig. 5.5. We will present final 3D locating results as well as the 1D ranging and 2D localization. The experiment setup in our lab environment is shown in Fig. 5.5(a).

Hardware: The harmonic RFID tag and the RFID reader were implemented on PCB and are shown in Fig. 3.8(a) and Fig. 3.11. The tag is connected to a single antenna (Tagolas broadband antenna [35]) with average gain of −1.9dBi. For 3D locating 4 Rx patch antennas which cover the harmonic band and 1 Tx Yagi antenna which covers the

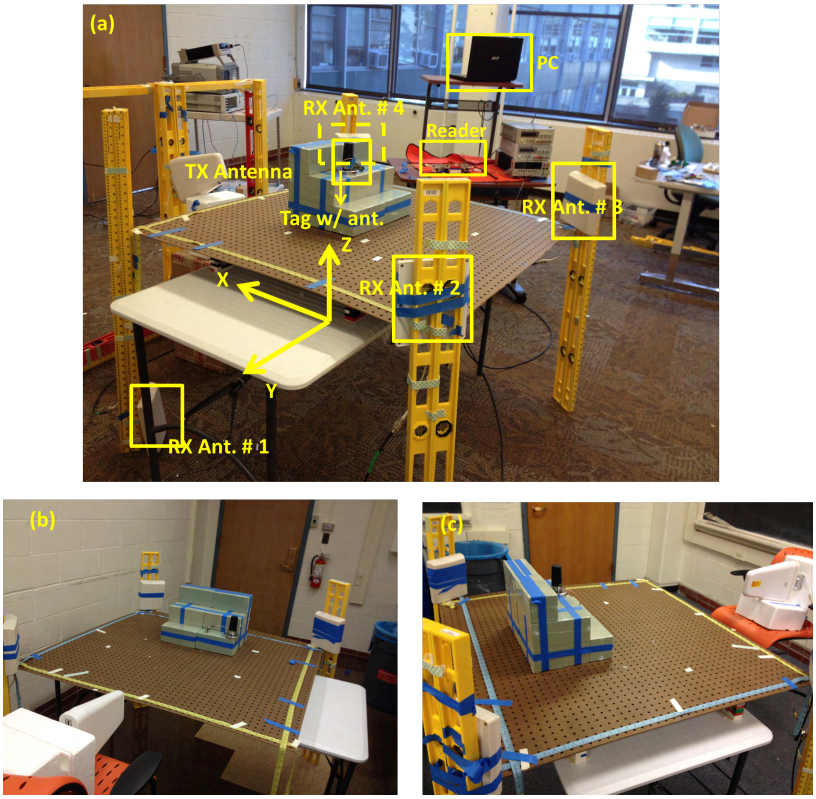

Figure 5.5: Experiment setup in indoor environments (a) Lab environments. (b) In a narrow lounge passage. (c) In a classroom.

fundamental frequency band were used. To help measure the locating error, we setup a wooden table with ruler markers. The 4 Rx antenna positions were $(122, 124, -83)$cm, $(12, 124, 0)$cm, $(12, 14, 0)$cm, $(122, 14, 0)$cm respectively. The distance from the Tx antenna to the center of the table was 100cm. The reader communicated to the host computer through a HC-06 Bluetooth module [37].

Software: We implemented the ranging algorithm and 3D locating algorithm as discussed in previous sections. The control program on the host computer was implemented via National Instrument Labview[39]. After obtaining data from reader via Bluetooth, Labview will then call the ranging and locating programs. A STM32 Cortex M4 microcontroller [40] coordinated amplification for both transmitter and receiver, the frequency synthesizer which handled frequency hopping, the ADC sampling for the decoded phase

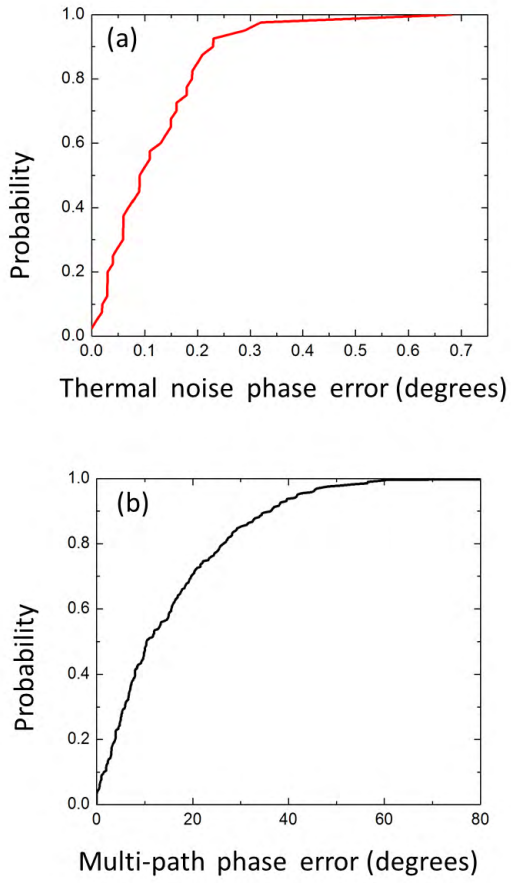

Figure 5.6: Measurement on (a) thermal noise induced phase error (b) multi-path induced phase error.

values, and communication between the host computer and the reader. The control program on the micro-controller was implemented with the Chibi-OS RT [54] platform.

5.4.1 1D ranging measurements

The cumulative distribution function (CDF) of thermal-noise induced phase measurement error and the multi-path induced phase measurement error in Lab environment are shown in Fig. 5.6(a) and (b), respectively. The thermal induced phase error is below 1°

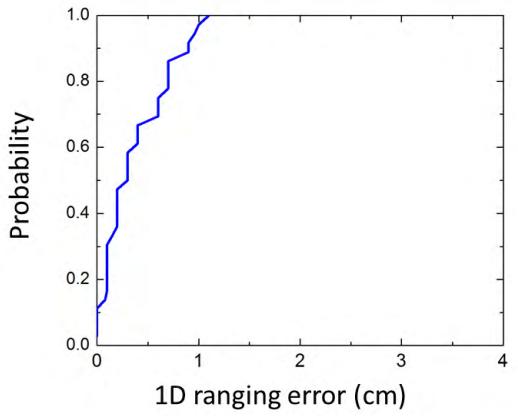

Figure 5.7: CDF 1-D ranging error.

while error is dominated by multi-path phase error which can be as large as 60°. However, our system can tolerate such large phase error by reliably computing phase cycle integers within a search range of R = 4m. The CDF of 1-D ranging is shown in Fig. 5.7. We achieve ranging below 1cm over 90% with median error of 3mm.

5.4.2 2D localization measurements

The CDF of 2D measurement results is shown in Fig. 5.8(a). In 2D experiments the #1 Rx antenna position was mounted at (122, 124, 0)cm and the rest 3 Rx antennas position remained unchanged. The search space is constraint in 2D. We achieved median error of 0.53cm and 0.82cm in the X and Y position respectively. A sample measurement in the 2D plane is shown in Fig. 5.8(b), where we put tag on the lattice in random order and our system was able to compute each location accurately and instantly.

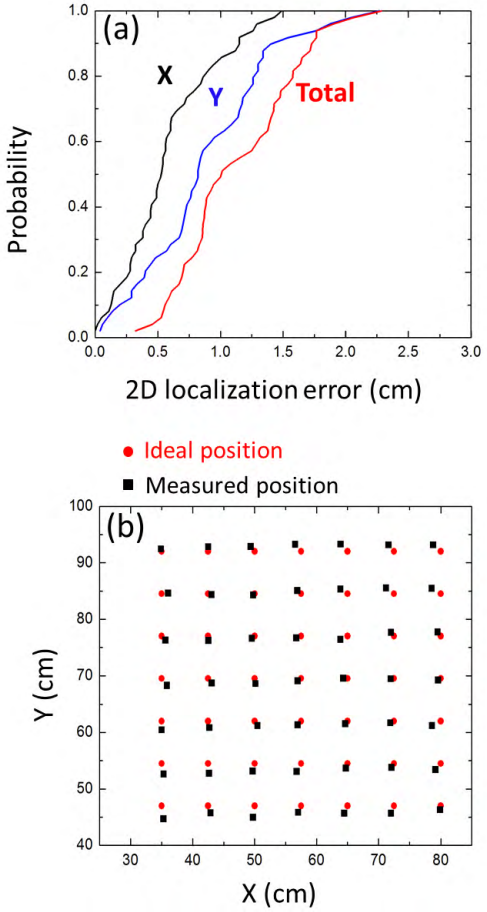

Figure 5.8: (a) CDF 2-D localization errors (b) a sample of 2D localization measured on the experiment table for various locations.

5.4.3 3D locating measurements

The CDF of 3D locating measurements are shown in Fig. 5.9(a)(b)(c). Three scenarios shown in Fig. 5.5 were tested to demonstrate robust measurements under different multipath interferences. The measurement was conducted in a region of 60cm ×60cm ×40cm above the table with the help of a foam stair which was put at different locations on the table. For lab environment, we achieved median error of 0.59, 1.54 and 1.97cm for X, Y and Z coordinates and a total median error of 3.5cm. While the maximum

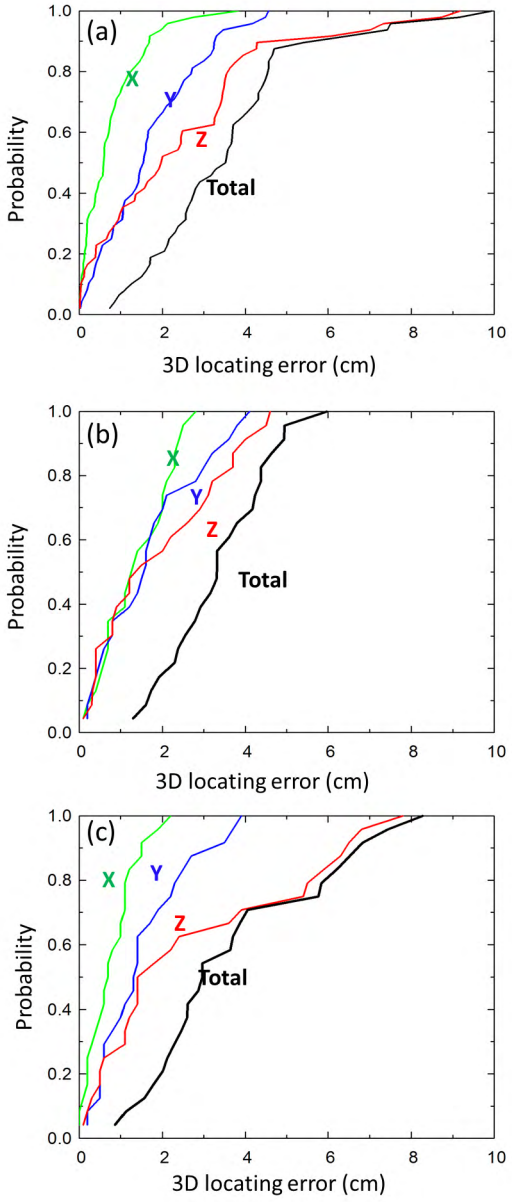

Figure 5.9: (a)(b)(c) CDF 3D locating error CDF measured in environments shown in Fig. 5.5 (a) (b) and (c) respectively.

error for X, Y, Z are 3.82, 4.56 and 9.17cm. By comparing Fig. 5.9(b)(c) to Fig. 5.6(a), the measurements were shown to be stable in other indoor environments. The major contribution of the measurement error was from the measured Rx antenna position errors which is not dependent on the environment. Because of the low diversity in Z direction

as we mounted Rx antenna # 2,3,4 in the XY plane between #1 Rx antenna and the target tag, maximum error along Z axis was significantly higher.

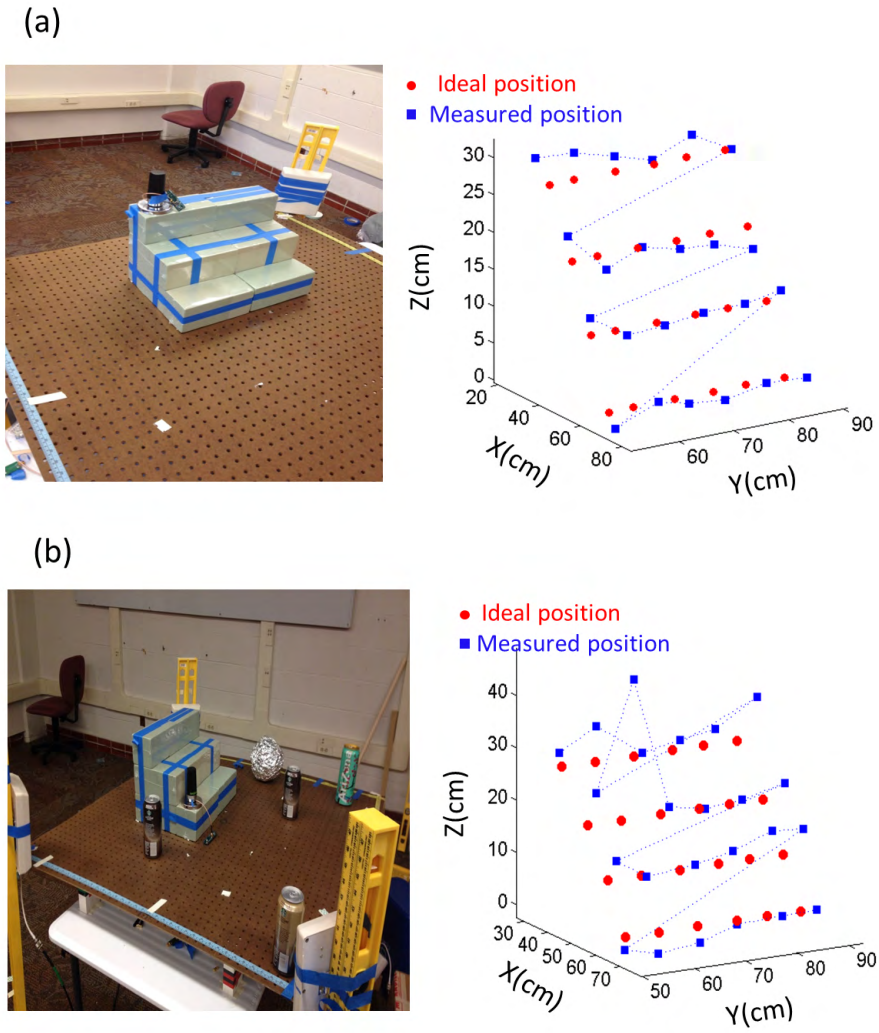

Figure 5.10: Testing sample of 3D locating in scatterer-free (a) and 5 metal scatterers (b) scenarios.

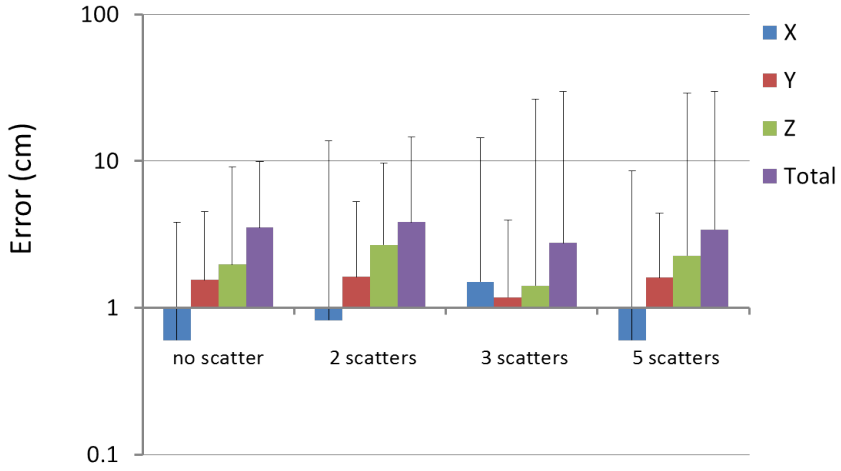

Figure 5.11: Median and maximum errors with different number of scatterers.

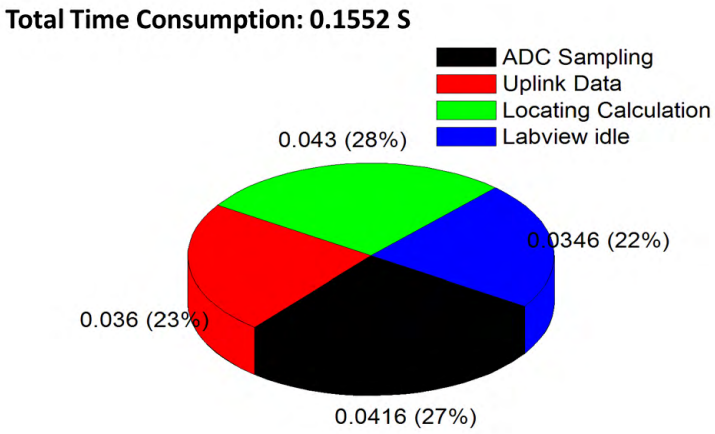

Figure 5.12: Pie chart of time consumption for one 3D locating measurement.

5.4.4 Locating with different scatters

To further show the robustness of the proposed method, 3D locating under various metal scatterers made of aluminum Balls with diameter around 15cm and soda cans of heights

from 10cm to 20cm within the reading zone was performed. The metal scatterers were randomly distributed on the table among the TX and RX antennas. A sample measurement with 5 scatterers is shown in Fig. 5.10(b) in comparison with the scatterer-free case in Fig. 5.10(a). The measured median and maximum errors for scatterer-free, 2 scatterers, 3 scatterers and 5 scatterers are shown in Fig. 5.11. The outliers with above 10cm locating errors all had wrong cycle integer estimation when the multi-path phase errors are beyond our system tolerance. As our locating methods performed robust, the median errors all fell within centimeter range due to the accurate phase cycle integer solution. There were no obvious relationship between the median errors and number of scatterers during the measurements, as when the phase cycle integer calculation are correct, the major error source came from the antenna phase center uncertainties which could vary during each calibration. Further integration with more receiver antennas or with beamforming capabilities to solve such problems will be in the future work [49].

5.4.5 Time budget

The Pie chart of time consumption for the present system is shown in Fig. 5.12. The total time consumption at present for one 3D locating measurement was 0.1552 seconds. The HMFCW ranging algorithm computation and 3D locating computation consumed 0.043 seconds, which is 28% of the total time consumption. In our current system, the ADC consumed most time budget with 0.0416 seconds (27%). To ensure Labview running smoothly, an idle time 0.0346 seconds (22%) was also inserted.

As our core algorithms are highly efficient which only take 28% of the total time, further acceleration of the whole 3D locating process can be readily made with more efficient control environment.

5.4.6 Real-time 3D tracking

In the previous section, we have shown that each 3D location measurement can be completed within 0.1552 seconds, the process can be further accelerated to track fast moving tag continuously by aligning data acquisition and locating computation in parallel. We demonstrated real-time 3D locating experiment in this section. In the experiment, the Harmonic-WISP RFID tag which is discussed in Chapter 3 was connected to a whip antenna [36] for its small size. In Fig. 5.13, we show real-time 3D tracking of a passive

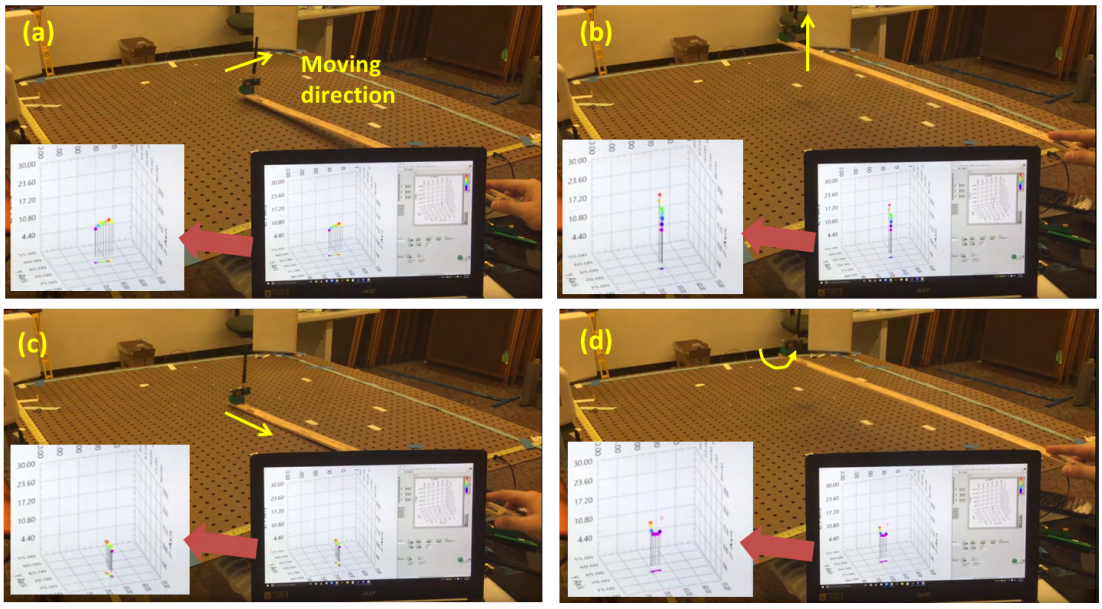

Figure 5.13: Passive tag real-time 3D tracking: (a) moving left, (b) moving up (c) moving inward, (d) moving circularly.

tag for different moving trajectory. We show examples of 4 motions: (a) moving left, (b) moving up (c) moving inward, (d) moving circularly. The real-time tracking curves were shown in the computer screens in Fig. 5.13. Our prototype system were able to capture this motions correctly at an updating rate of 13Hz. In Fig. 5.14, we show real-time 3D tracking of a toy train running at speed about 5cm/s with the help of a passive harmonic RFID tag. The tag is attached to the toy train. The height of the trajectory is denoted by

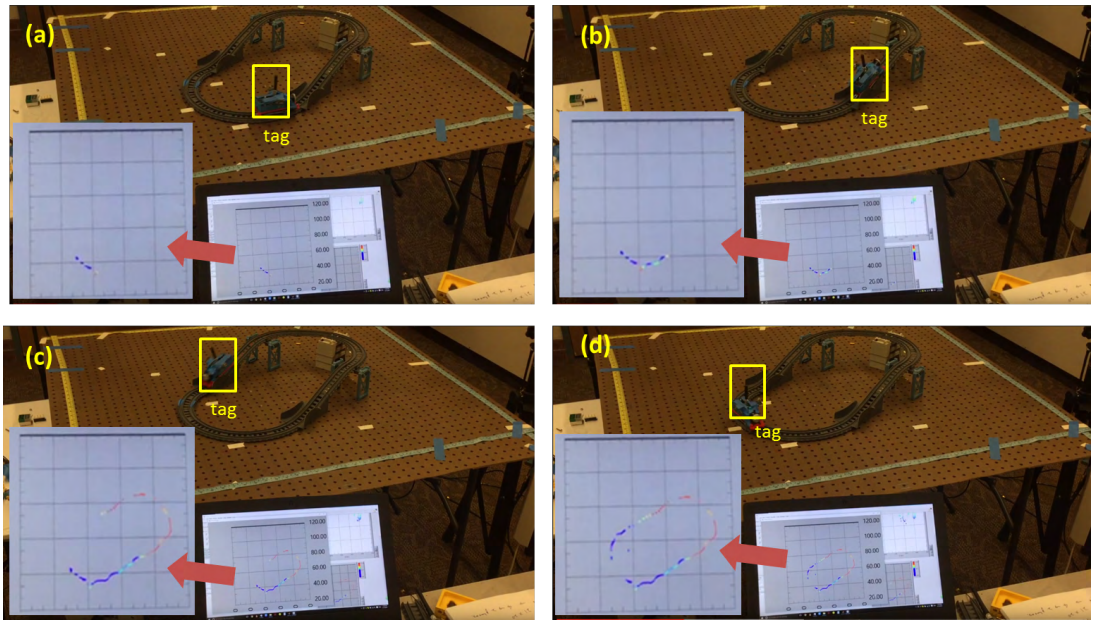

Figure 5.14: Real-time 3D tracking of a passive tag attached to a toy train.

the color of the trace. In our experiment, we can robustly recovery the moving trajectory of the toy train in real time shown in the computer screens in Fig. 5.14. The tracking accuracy is within the range of centimeter.

5.5 Conclusion

In this Chapter, we show that centimeter-level accuracy real-time 3D locating can be achieved for RFID with the nonlinear backscatter approach. The proposed approach does not need any relative motion or anchor nodes and therefore can be readily applied to a large variety of applications.

CHAPTER 6

DIVERSITY EXPLORATION: TIME DIVERSITY

Interference caused by unpredictable body motion is notorious in RF-based ranging and tracking. For passive tags, the strong self-leakage signal and large unwanted direct reflections encountered in conventional RFID transceivers make precision ranging even more difficult. To achieve fast, high accuracy ranging capability against body interference, we show that time diversity of fast-fading wireless channel can be exploited to boost the phase error threshold in HMFCW. In this Chapter, we investigate a second harmonic backscattering solution in the opportunistic method of sequential test heuristic multi-frequency continuous wave (ST-HMFCW) ranging. We show that direct reflection and self-interference are greatly suppressed, so the received second harmonic phase variation is decoupled from the power-dependent phase distortion caused by large jamming interference. ST-HMFCW ranging seeks opportunities in phase fluctuations caused by interferer motion and its performance can be drastically improved as bandwidth increases. Robust millimeter-accuracy ranging is achieved under strong body-motion interference with the broadband nonlinear transmission line (NLTL) backscatter tags. We present the theory, simulation and experimental prototypes to verify the effectiveness of the proposed ST-HMFCW ranging method.

6.1 Multi-path variations with body motions

In the presence of boy motion interference as shown in Fig. 6.1, the received second harmonic signal at $2f$ backscattered from the tag takes the form:

$$r = qA \exp\left[j(4\pi f t - \frac{8\pi f}{c}|\mathbf{r}_{\text{tag}}|) \right] + N \tag{6.1}$$

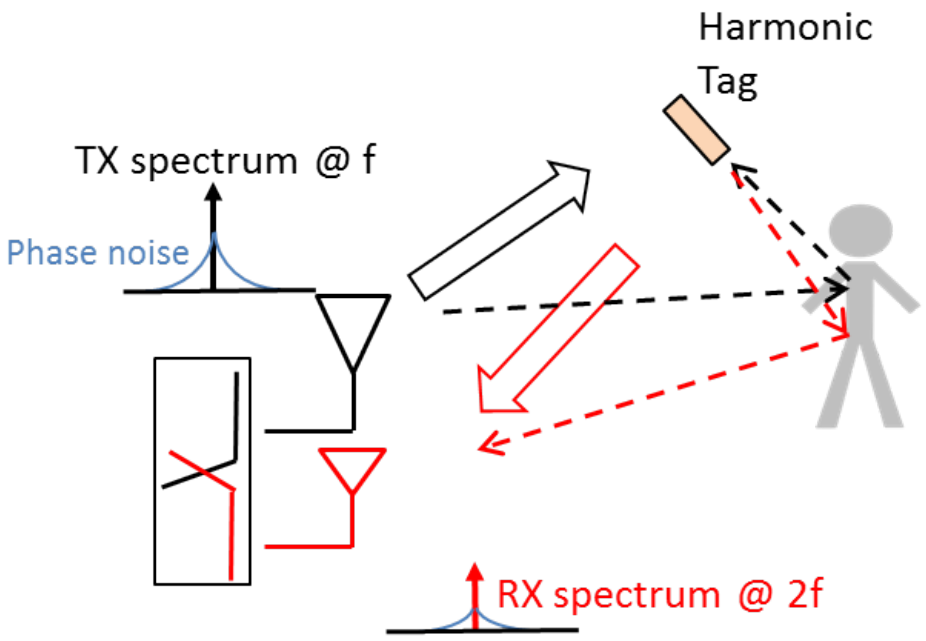

Figure 6.1: Harmonic backscattering with body motion interference

where A is the second harmonic amplitude. $\mathbf{r}_{\text{tag}}$ is the tag location referred to the reader. N denotes noise. The factor q represents the effect of multi-path interference on phase and amplitude errors [27]:

$$\begin{aligned} q &= \left(1 + \sum_i \frac{\exp(j\Delta\phi_i^{\text{DL}})}{\sqrt{\text{SIR}_i^{\text{DL}}}}\right)^2 \left(1 + \sum_i \frac{\exp(j\Delta\phi_i^{\text{UL}})}{\sqrt{\text{SIR}_i^{\text{UL}}}}\right) \\ &= 1 + B\exp(j\alpha) \end{aligned} \tag{6.2}$$

The first part is squared because the amplitude of the received second harmonic is proportional to the square of the amplitude of the inquiry signal on fundamental frequency f [27]. The error terms in downlink and uplink can be further combined into one complex number with amplitude B and phase α. SIR_i is the signal-to-interference ratio with respect to the i-th scatterer, and superscripts "DL"and "UL"denote downlink and uplink, respectively. $\Delta\phi_i$ is the phase delay difference between the LOS path and the i-th multi-path. The SIR can be expressed as:

$$SIR_i = \frac{4\pi|\mathbf{r}_{\text{tag}} - \mathbf{r}_i|^2|\mathbf{r}_i|^2}{|\mathbf{r}_{\text{tag}}|^2 \text{RCS}_i} \tag{6.3}$$

where $\mathbf{r}_i$ and $\mathbf{r}_{\text{tag}}$ are the location referred to the reader for the i-th scatterer and the tag, respectively. Note that RCS is angle and frequency dependent and thus usually different in uplink and downlink. The phase differences in downlink and uplink are:

$$\Delta\phi_i^{\text{DL}} = \frac{2\pi f(|\mathbf{r}_{\text{tag}}| - |\mathbf{r}_i| - |\mathbf{r}_i - \mathbf{r}_{\text{tag}}|)}{c} + \delta_i^{\text{DL}} \tag{6.4}$$

and

$$\Delta\phi_i^{\text{UL}} = \frac{2\pi f(|\mathbf{r}_{\text{tag}}| - |\mathbf{r}_i| - |\mathbf{r}_i - \mathbf{r}_{\text{tag}}|)}{c} + \delta_i^{\text{UL}} \tag{6.5}$$

The phase differences consist of two parts. The first part is caused by the propagation time difference and the second part δ_i is the phase offsets occurring during scattering.

Motion of human body will cause channel fluctuations, and hence variations in SIR and $\Delta\phi$. For $B < 1$, let θ denote the measured carrier phase. The maximum phase error is:

$$\Delta\theta_{\max} = \arcsin(B) \tag{6.6}$$

The characteristics of phase error fluctuations by random body motion are illustrated in the following example.

Example: In a $6 \times 6\text{m}^2$ area, a reader and a harmonic tag with 0dBi omnidirectional antenna gains are separated by 2 meters. fundamental frequency f is at 1GHz. The body RCS is set to 0.72m^2, which is 100 times of the effective transmitter antenna area. The body is assumed to be in random walk at the speed $v = 1\text{m/s}$. For simplicity, phase offset in the scattering is assumed to be a random constant number in $[0, 2\pi]$. The corresponding phase error of the received second harmonic signal is shown in Fig. 6.2.

Scatterers with large effective RCS like human body induce large phase errors that exhibit fast variation under a relatively slow modulated mask. Compared to the SIR fluctuation, at high f, the phase terms are much more sensitive to body motion, which induces fast variation in α. The change in SIR leads to slow variation in B and $\Delta\theta_{\max}$.

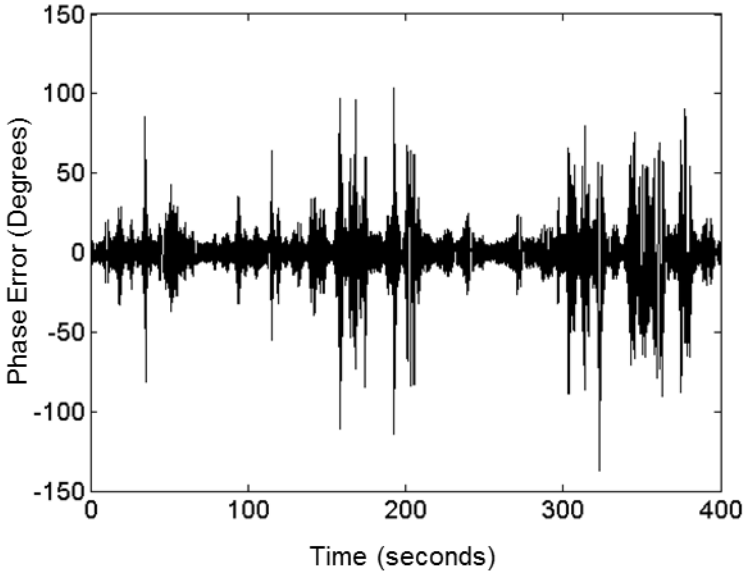

Figure 6.2: Received second harmonic phase error fluctuations caused by random body motion

The corresponding auto-correlation function in $\exp(j\alpha)$ and B are shown in Fig. 6.3. The time interval that channel changes significantly is measured by the coherence time T_c. For α, the coherence time is inversely proportion to the Doppler spread [10] and is almost two orders of magnitude smaller than that of B. In our case, for the correlation level at 0.1, coherence time of α in the harmonic backscatter can be roughly estimated as:

$$T_c{}^{\alpha}(0.1) \simeq \frac{c}{5fv} \tag{6.7}$$

With higher f, $T_c{}^{\alpha}$ will further shrink, but fluctuations in B will not scale down as frequency increases. At $v \simeq 1$m/s, $T_c{}^{\alpha}(0.1)$ is around tens of millisecond, while the coherence time of B, $T_c{}^{B}(0.1)$ is up to several seconds. The fast variation of phase α, relatively slow fluctuation of B and the phase error bound $\Delta\theta_{\max}$ should be carefully considered to design the ranging method.

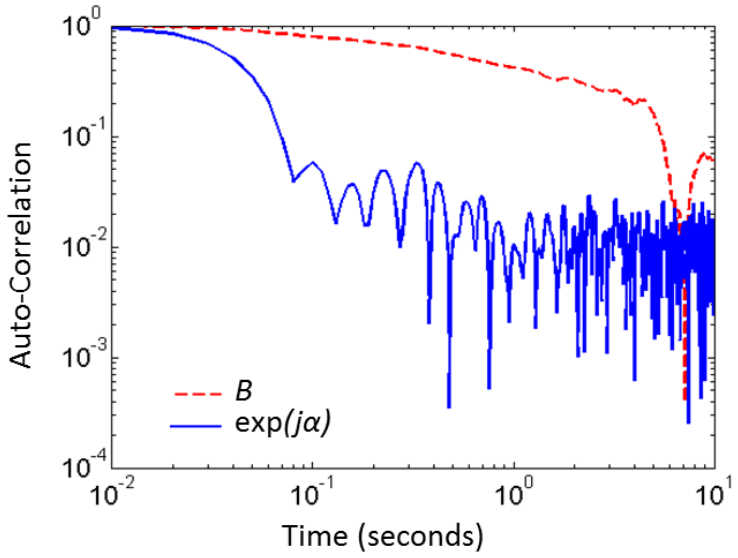

Figure 6.3: Auto-correlation in exp($j\alpha$) and B.

6.2 Harmonic ranging in ST-HMFCW

To deal with large phase fluctuations caused by body motions, we investigate broadband harmonic ranging strategy in ST-HMFCW. Notice that when phase distortion caused by jamming saturation is removed, phase fluctuations actually bring opportunities of getting small phase errors even with large multi-path interference: there are chances that the phase difference between signal and interference is sufficiently small or close to π. These opportunities are exploited by K-consistency sequential tests to extend phase error tolerance and improve spectral efficiency. Together with the frequency selection and cycle integer estimation in the broadband heuristic multi-frequency continuous wave ranging (HMFCW) method, the K-consistency sequential test in the ST-HMFCW ranging method can maintain ranging precision even in the presence of large phase errors by employing the coherence time characteristics of the fast-fading channel.

In HMFCW ranging, assuming we are using frequency combination $\mathbf{f} = (f_1, f_2, \cdots, f_L)$ for ranging. As long as the cycle integer estimation is correct, high accuracy can be achieved even with large phase error. For simplicity, we take the following ranging estimation. Pick the highest frequency f_L

$$\hat{d} = \frac{\lambda_L}{4}\hat{a}_L + \frac{\theta_L}{2\pi}\frac{\lambda_L}{4} \tag{6.8}$$

here, we use the quarter-wavelength $\lambda/4$ instead of $\lambda/2$ in the previous chapter because we are considering the round trip ranging. For differential ranging cases, we should use $\lambda/2$, however, all the analysis discussed in the section will still apply.

If the cycle integer estimation $\hat{a}_L$ is correct. Then the estimation error is:

$$\Delta d = |\hat{d} - d| = \frac{|\Delta\theta|}{8\pi}\lambda_L \leq \frac{\Delta\theta_{\max}(B)}{8\pi}\lambda_L \tag{6.9}$$

In chapter 4, it is pointed out that if the phase error θ is bounded within $[-\Phi, \Phi]$, the correctness of integer estimation is 100% guaranteed.

6.2.1 K-Consistency Sequential Test

Under strong interference, maximum phase errors $\Delta\theta_{\max}$ larger than Φ can occur. On the other hand, for given ranging accuracy requirement ${\Delta d_{\max}}^{\text{req}}$ (e.g. setting ${\Delta d_{\max}}^{\text{req}} = 1\text{cm}$ to achieve frequent mm-precision), the phase error just needs to be below Ψ

$$\Psi = 8\pi\frac{{\Delta d_{\max}}^{\text{req}}}{\lambda_L} \tag{6.10}$$

The operation of K-consistency sequential tests is illustrated below. Assume that $\Delta t_{\text{cycle}} > L\Delta t_s > LT_c{}^{\alpha}$ shown in (6.7) and thus each time ranging phase errors can be treated independently. For h-th transmitting frequency, if the estimated distance is

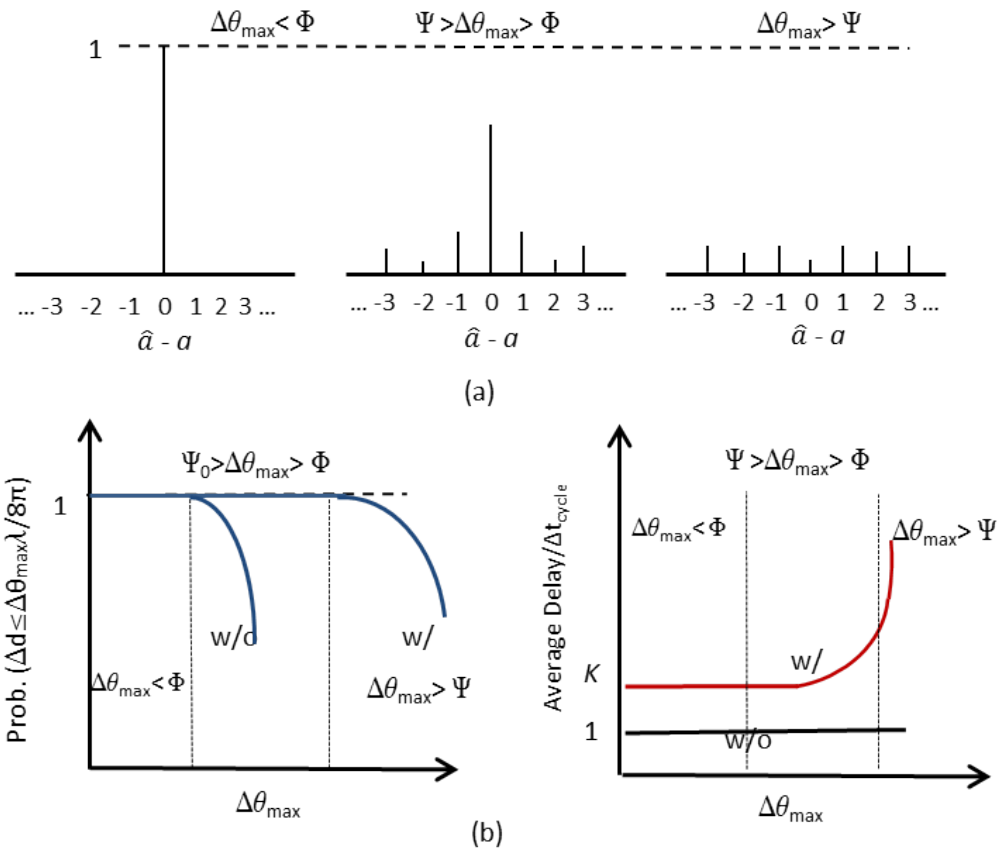

Figure 6.4: (a) Integer estimation error evolution; (b) Effects with and without K-consistency sequential tests in HMFCW ranging.

$\hat{d}_{(h)}$, the output estimated distance is updated as

$$d_{\text{est}} = \hat{d}_{(h)} \tag{6.11}$$

if and only if for integer K and $h - K + 1 \leq t \leq h$,

$$|\hat{d}_{(t)} - \hat{d}_{(t-1)}| \leq \frac{\lambda_L}{8} \tag{6.12}$$

If $\Phi < \Psi$, the phase error region between $[\Phi, \Psi]$ can be further exploited to improve spectrum efficiency, while $\Delta\theta_{\max}$ larger than Ψ needs to be rejected. Fortunately, opportunities arise from the fluctuations in wireless channels caused by human body motions to allow both improvements to be achieved at the same time.

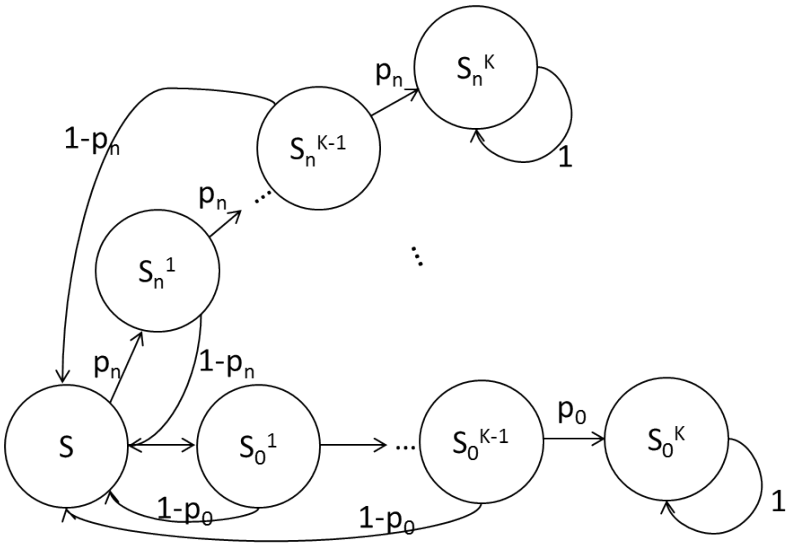

Figure 6.5: State machine of K-consistency sequential test.

Otherwise, when the above condition is not satisfied, the next sequence is taken in and the condition is re-checked. The K-consistency sequential test leverages the estimated error evolution along with the increase of $\Delta\theta_{\max}$. Let p_l denote the probability of integer error equal to l:

$$p_l = Prob.(\hat{a} - a = l) \tag{6.13}$$

As $\Delta\theta_{\max}$ becomes larger, the number of error events ($l \neq 0$) increases. Meanwhile, the probability on the initially probabilistically dominant event ($l = 0$) will be gradually split into these error events, and finally there is no probabilistically dominant event, as shown in Fig. 6.4(a). However, the only possible dominant event in HMFCW during the evolution is the correct integer estimation. As shown in Fig. 6.4 (b), by controlling the value of K, firstly, probabilistically dominant outcomes can be timely discovered when $\Delta\theta_{\max}$ is within $[\Phi, \Psi]$, thus extending the low error probability region of integer estimation. Secondly, as $\Delta\theta_{\max}$ reaches above Ψ, the average delay/waiting time is tuned by K to change dramatically within a small transition period. In another word, we reject the measured distance when $\Delta\theta_{\max} > \Psi$ and wait until the channel condition

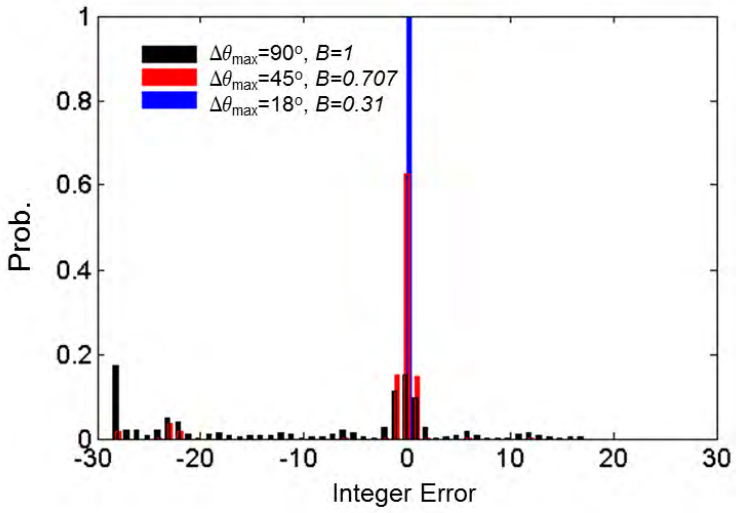

Figure 6.6: Estimated integer error profile evolution as $\Delta\theta_{\max}$ increases at 20% BW.

changes for further updates. A threshold on waiting time can also be set to trigger other measures such as antenna angle/position adjustment to help assist ranging operations [41]. The probability of an accurate result and the associated delay ET (Estimated Time) for $\Delta\theta_{\max} < \pi/2$ are derived from corresponding state machine shown in Fig. 6.5 (the initial state is denoted as S, and state ${S_l}^k$ denotes the state where the integer error is l for consecutive k times) and can be estimated as:

$$Prob.(\Delta d \leq \frac{\Delta\theta_{\max}}{8\pi}\lambda_L) \simeq \frac{{p_0}^K}{\sum_l {p_l}^K} \tag{6.14}$$

and

$$E_T \simeq \frac{1 + \sum_l p_l \frac{1-{p_l}^{K-1}}{1-p_l}}{\sum_l {p_l}^K} \tag{6.15}$$

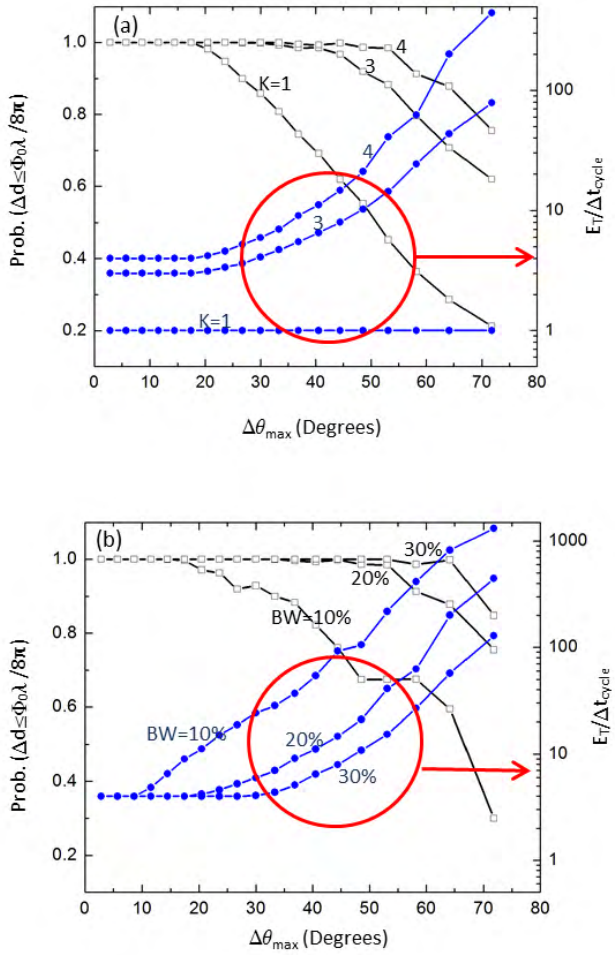

Figure 6.7: ST-HMFCW performance vs. $\Delta\theta_{\max}$ for (a) different K, BW = 20%; (b) different BW, $K = 4$.

6.3 Phase error threshold boosting by time diversity

The heuristically optimized frequency selections for BW at 10%, 20% and 30% used in following simulations are listed in Table 6.1. Φ is calculated when $\Delta d_{\max}{}^{\text{req}} = 1$cm. The integer error evolution in HMFCW at BW=20% is shown in Fig. 6.6 for a tag placed 1 m from the reader as an example. Distribution for $\Delta\theta$ is derived from Eq. (6.2) with

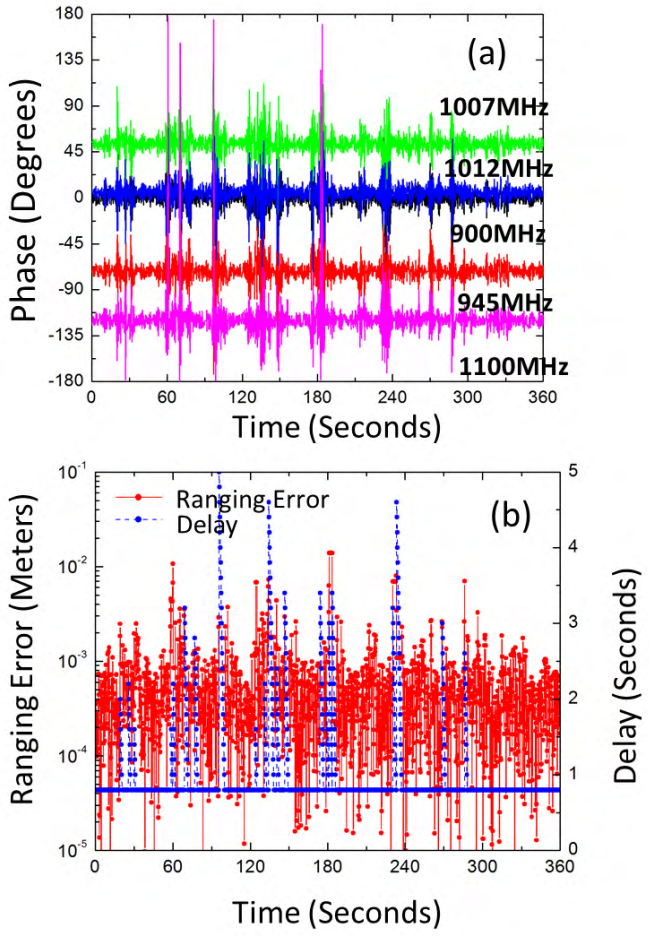

Figure 6.8: ST-HMFCW with $K = 4$, BW $= 20\%$ under random body motion interference: (a) Received SH phase fluctuations for each inquiry frequency; (b) Ranging error and delay.

fixed B and uniformly distributed α in $[0, 2\pi]$. Switching time Δt_s is assumed to be larger than $T_c{}^{\alpha}(0.1)$, so the phase errors are treated independent for different frequencies for simplicity. As discussed before, with increasing $\Delta\theta_{\max}$, the probabilistically dominant event gradually fades out into increasingly large number of error events. Finally, at very large $\Delta\theta_{\max}$, outcome becomes very diverse with no dominant event, and ranging output condition cannot be achieved.

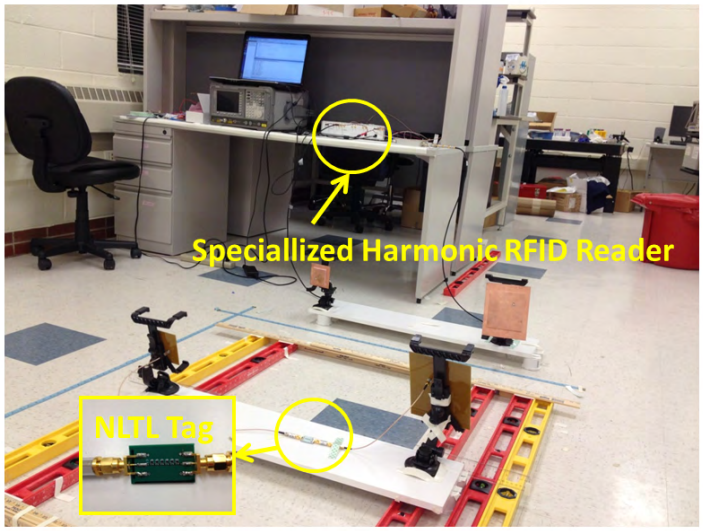

Figure 6.9: Experiment setup second harmonic ST-HMFCW ranging.

Table 6.1: Optimized frequency selection samples

Case No.	Number of freq.	Freq. (MHz)	BW%	Φ	Ψ	Reading range R
1	4	950,968,1014,1050	10%	9°	50°	4.5 m
2	5	900,945,1007,1012,1100	20%	18°	53°	4.5 m
3	6	850,877,916,1113,1125,1150	30%	27°	55°	4.5 m

Performance of ST-HMFCW $\Delta\theta_{\max}$ (or equivalently B) is shown in Fig. 6.7. ST-HMFCW extends the low ranging error region as K increases with small delay penalty between $[\Phi, \Psi]$, while the delay grows much faster with $\Delta\theta_{\max}$ beyond Ψ. In Fig. 6.7 (b), performance of ST-HMFCW ranging improves drastically as BW% increases, which shows feasibility of building a robust high-precision ranging system with efficient bandwidth usage.

Performance of ST-HMFCW ranging with $K = 4$ under random body motion is evaluated with $BW = 20\%$. In Fig. 6.8, Δt_s is set to 40ms and Δt_{cycle} to 200ms. The phase error on the harmonic backscatter of each fundamental inquiry signal is shown in

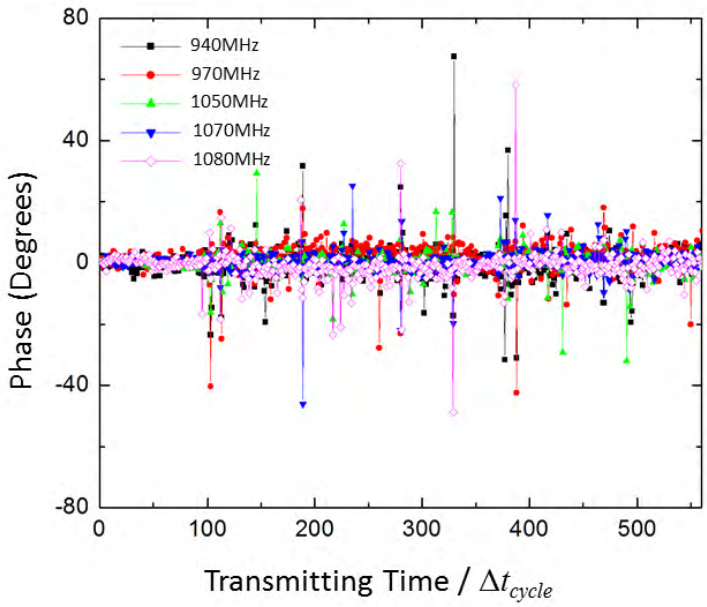

Figure 6.10: Relative phase errors caused by body motion when a person is walking around of the harmonic backscatter signal for the tag fixed at 0.9m.

Fig. 6.8 (a). For different time when reader begins to perform ranging, the ranging error and the corresponding delay are shown in Fig. 6.8 (b). In this simulation, even with large phase error fluctuation up to 90° caused by body motion, ST-HMFCW ranging shows robust ranging error in millimeter scale with delay below 5s for $BW = 20\%$.

6.4 Experimental verification

We verified the effectiveness of ST-HMFCW in a prototype system with a real-time harmonic backscattering reader. The NLTL tag was fabricated on PCB, which has −15dBm conversion loss and 3dB bandwidth from 600MHz to 1200MHz. Home-made patch antennas on both fundamental and SH frequencies are mounted on a rail to perform

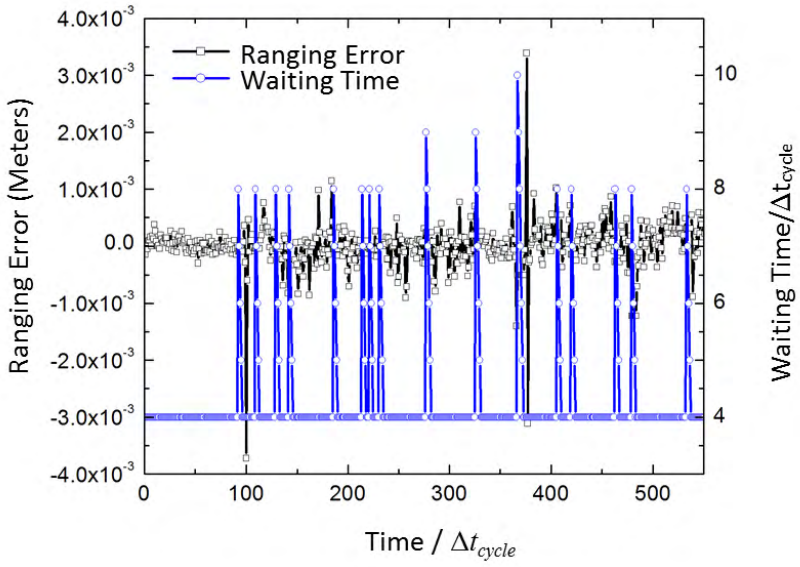

Figure 6.11: Corresponding ranging errors and delays caused by body motion when a person is walking around in ST-HMFCW ranging with K = 4 at BW=14% based on the measurements in Fig. 6.10.

ranging. The transmitting frequencies are chosen as 940MHz, 970MHz, 1050MHz, 1070MHz and 1080MHz. Δt_s is set at 100ms and Δt_{cycle} at 500ms. BW is equal to 14% and the maximum reading range is set at 3m. Calibration was done at 0.9m from the reader in order to cancel constant phase offset. The system setup is shown in Fig. 6.9.

To better understand the ranging error and delay caused by body motion interference, the tag was fixed at 0.9m to cancel out any artificial errors in distance measurement (e.g. errors caused by rail and antenna setup and tape measuring) and interference was then induced by walking around and hands and limbs waving before Tx and Rx antennas including walking through the LOS path in the second experiment. The recorded relative phase fluctuations are shown in Fig. 6.10 and the ranging error and corresponding delay are shown in Fig. 6.11. The maximum ranging error is about 4mm and the maximum

delay about 10 transmitting cycles.

6.5 Conclusion

In the effort to realize millimeter accuracy ranging of passive tags in an arbitrary environment, we investigate the broadband harmonic ST-HMFCW ranging technique to overcome random body motion interference. Both simulation and experiment have shown that the proposed approach is accurate and effective. The efficient bandwidth usage enables simple and low-cost system implementation. The proposed method is not limited to stationary passive tags, and can be embedded in other RFID locating methods to further resolve both dynamic and static interferences at the same time.

CHAPTER 7

DIVERSITY EXPLORATION: FREQUENCY DIVERSITY

The extreme broadband operation enabled by harmonic backscatter offer an unique opportunity for us to explore the frequency diversity.

Previous indoor RFID locating are always measured using high-directivity antenna due to the dense multi-paths [5, 11, 8, 55, 56]. High-gain antennas such as horn and patch antennas on readers and tags are often cumbersome because of their large size, heavy weight and high cost. The narrow angle coverage and high phase center variations pose additional difficulties in deployment and calibration [58]. Low-cost, omnidirectional antennas such as whip or rubber ducky antennas offer much smaller size and weight, enabling easy integration to portable devices with broad angle coverage and low phase center variation. For example, the Laird S9028PCR 9dBi patch 900MHz antenna has dimension of 259×259×33mm and weight of 793g, while the Taoglas TG22 low-directivity whip [36] antenna at same frequency offers 48mm×6mm∅ and 5.1g. However, locating passive tags with low-directivity antennas in indoor environment becomes even more challenging due to more multi-paths and weaker line-of-sight (LoS) path.

7.1 Basic idea

In order to enable high accuracy locating with low-directivity antennas, we must find a way to deal with the extreme conditions where the LoS path is totally dominated by multi-paths. Compared to the conditions dominated by multi-paths, the conditions with strong LoS paths are more reliable. The basic idea is to build a system that can tell which measurement is reliable and which one is not. In other words, the locating system needs to have some simple intelligence. Before describing the proposed solution, we

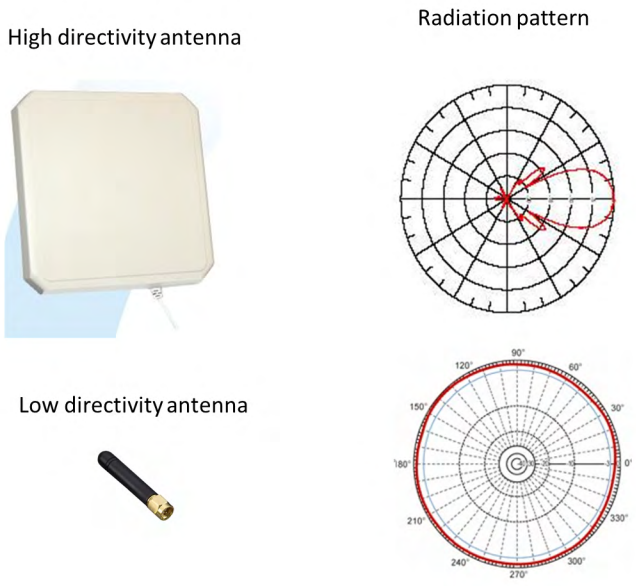

Figure 7.1: High-directivity antenna and low-directivity antenna. Low-directivity antenna is much smaller, lighter, more flexible, but sees more multi-paths.

will first talk about the ”coherence bandwidth” concept brought by the frequency diversity and how to utilize coherence bandwidth to make judgment about wireless channel conditions.

7.2 Multi-paths and coherence bandwidth

Coherence bandwidth is a statistical measure of the range of frequencies over which the channel can be can be considered ”flat” [59, 60]. Within coherence bandwidth, two frequencies have a strong potential for amplitude and phase correlation, but when two frequencies are separated larger than coherence bandwidth, their channel responses look more independent.

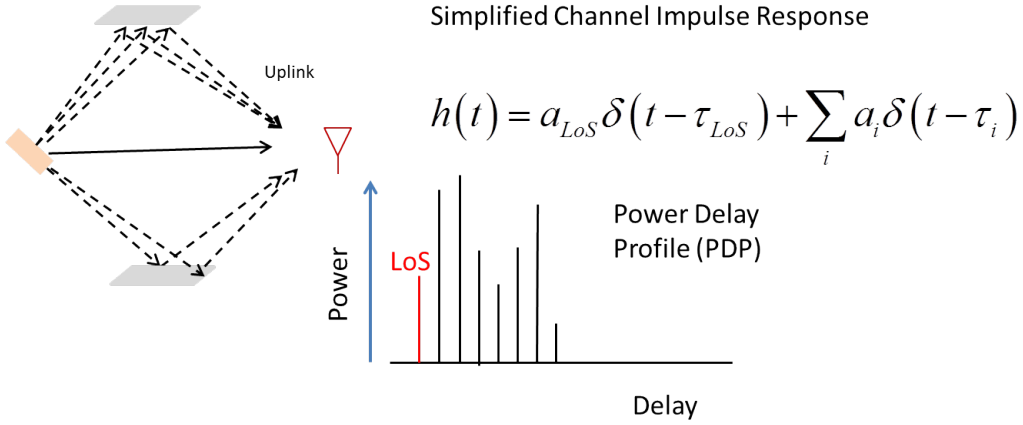

Figure 7.2: Simplified wireless channel impulse response and power delay profile

Coherence bandwidth is a phenomenon that is directly related to multi-paths propagation as shown in Fig. 7.2. For simplicity, a wireless channel impulse response can be written as:

$$h(t) = a_{\text{LoS}}\delta(t-\tau_{\text{LoS}}) + \sum_i a_i\delta(t-\tau_i) \tag{7.1}$$

where a_{LoS}, τ_{LoS} are the amplitude and delay of the LoS path, while a_i, τ_i are amplitude and delay of the i-th multi-path. For a transmitted signal $s(t)$ at frequency f

$$s(t) = \exp\left(\frac{j2\pi f}{c}t\right) \tag{7.2}$$

The received signal after multi-paths propagation can be expressed as

$$y(t) = s(t) * h(t) = a_{\text{LoS}}\exp\left[\frac{j2\pi f}{c}(t-\tau_{\text{LoS}})\right] + \sum_i a_i\exp\left[\frac{2\pi f}{c}(t-\tau_i)\right] \tag{7.3}$$

The carrier phase along each multi-path is frequency and delay sensitive, which results in adding constructively and destructively on different frequencies as shown in Fig. 7.3. The coherence bandwidth of multi-path profiles at different frequencies can be measured by the root-mean-square (RMS) multi-path delay spread δ_τ [60], and for the correlation level at 0.5, the coherence bandwidth is

$$B_c = \frac{1}{5\delta_\tau} \tag{7.4}$$

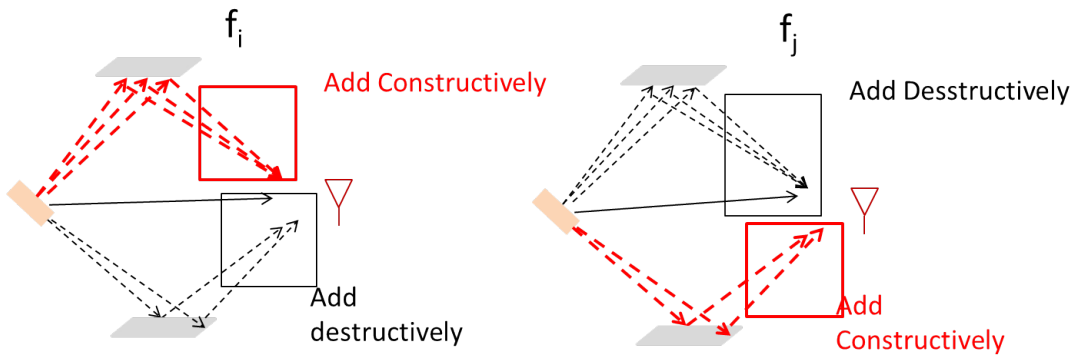

Figure 7.3: Frequency selective channel response resulted from multi-paths

It is important to note that Eq. (7.4) is only empirical and in general, spectral analysis techniques and simulation are required to determine the exact impact. However, from Eq. (7.4), we can see that the coherence bandwidth is inversely proportional to the RMS delay spread. With more multi-paths, the coherence bandwidth B_c tends to shrink which leads to a frequency selective wireless channel. For typical indoor environment with geometry size from 3m to 15m, δ_τ varies from 10ns to 50ns [60], resulting B_c from 4 to 20MHz.

7.3 AoA on frequencies separated larger than B_c

The coherence bandwidth gives us an opportunities to tell the channel conditions. We achieve such as task by leverage the "Gap of angle of arrival (AoA)" as shown in Fig. 7.4. For harmonic frequencies with separation wider than B_c, the strong multi-path signals will have large AoA differences as they are minimally correlated. For the LoS path, different frequencies are always heavily correlated no matter how large the frequency separation is. Therefore, when LoS is strong, AoA calculated from digital beamforming should yield a very similar angle for different frequencies, but when multi-paths are

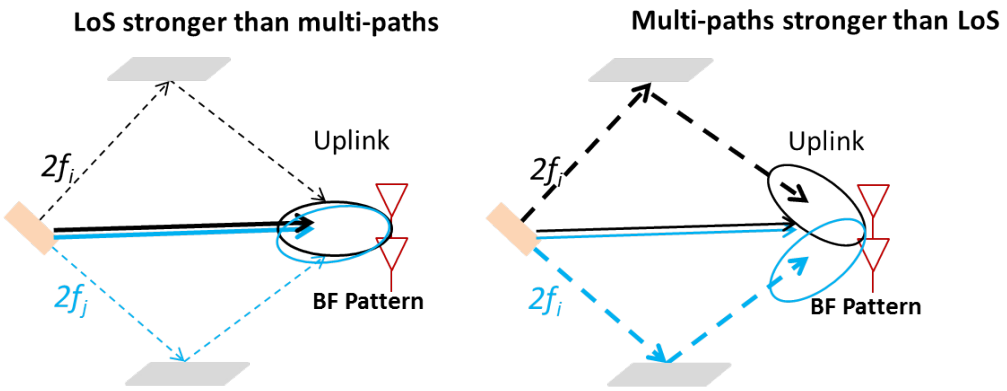

Figure 7.4: Quality Estimate w/ Gap of AoA. When LoS is strong, two frequencies will have close AoA. When multi-paths are strong, two frequencies will have different AoA estimations when separated larger than B_c

strong, for frequencies separated wider than B_c we expect large AoA gap, which can be used as a measure of multi-path dominance:

$$G_{\text{AoA}} = \max_k \left\{ \max_i(\beta_{k,i}) - \min_i(\beta_{k,i}) \right\} \tag{7.5}$$

where $\beta_{k,i}$ denotes the estimated AoA for the k-th 2-element antenna array on the i-th harmonic carrier. Please note that in HMFCW ranging discussed in Chapter 4, we are transmitting a frequency sequence $\mathbf{f} = (f_1, f_2, \cdots, f_N)$ to resolve the phase cycle ambiguity problem.

7.4 Digital beamforming with 2-element antenna arrays

We can use the minimum-sized antenna to build a locating system with intelligence to estimate G_{AoA}. The multi-static ranging system with 2-element low-directivity antenna arrays are illustrated in Fig. 7.5. We strengthen the LoS signal by spatial filtering

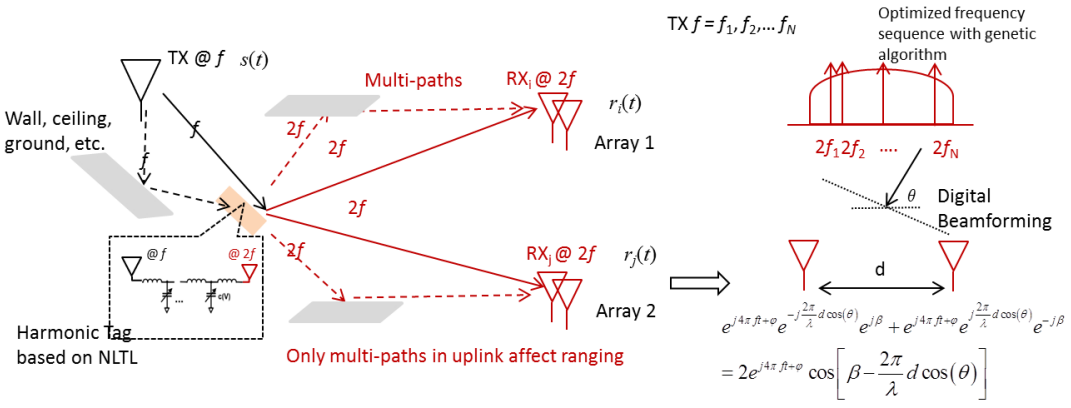

Figure 7.5: Frequency selective channel response resulted from multi-paths

through digital beamforming with minimum array size of $M = 2$. The center of the beam is rotated by applying weighted sum of signals r_1 and r_2 in the dual channels:

$$r = r_1 e^{j\frac{\pi}{\lambda} d\cos(\alpha)} + r_2 e^{-j\frac{\pi}{\lambda} d\cos(\alpha)} \tag{7.6}$$

where α is the beam steering angle. For a signal with incident angle θ, the beamforming factor can be expressed as

$$BF = \cos\left\{\frac{\pi d[\cos(\alpha) - \cos(\theta)]}{\lambda}\right\} \tag{7.7}$$

The signal phase is computed at α when r attains maximum. The effectiveness of spatial filtering depends on the antenna spacing d, as shown in Fig. 7.6. Increasing d gives a desirable narrow central beamwidth. However, the ambiguous side lobe with $BF = -1$ may arise which can cause 180° in the carrier phase computation and wrong AoA estimation. Notice that due to the broad frequency separation in HMFCW ranging, peaks of ambiguous side lobes spread much wider than the central beam peak. We implemented a two-stage search to avoid this multi-lobe issue. In stage one, we estimated AoA within 0° to 180° based on maximizing r in Eq. (7.6), and then used Eq. (7.7) to compute AoA corresponding to other potential peaks. In the second stage, we constructed groups of

Table 7.1: Optimal Tx frequency combination used in experiment

Number of freq.	Freq. (MHz)	BW%	Phase error threshold Φ	Reading range R
5	855 870 899 937 1090	24%	22°	3 m

peaks by drawing one peak at a time corresponding to each sensing frequency for each group. The group with minimum deviation was selected. Then, we recalculated AoA around the average of the selected group with a reduced search range.

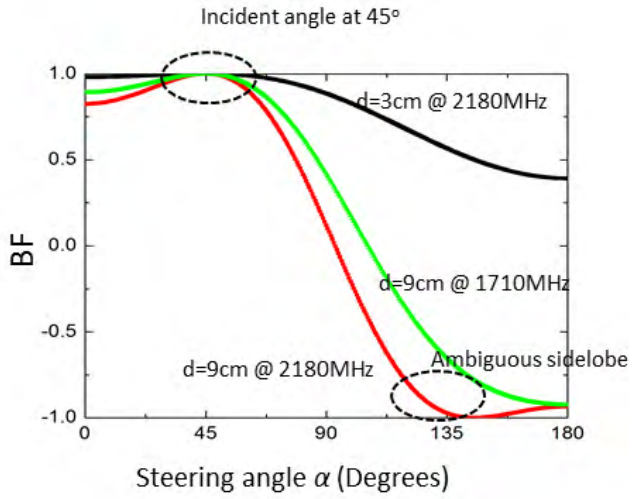

Figure 7.6: Beamforming factors with different antenna separation at different frequencies. The incident angle is set at 45°.

7.5 Experimental results

Homodyne harmonic reader was implemented as shown in Fig. 7.7(b). Dual arrays of 2-element omni-directional antennas on the reader were Taoglas Shockwave Series of length at 8cm and diameter at 4cm for their easy and stable plug in mounting, which

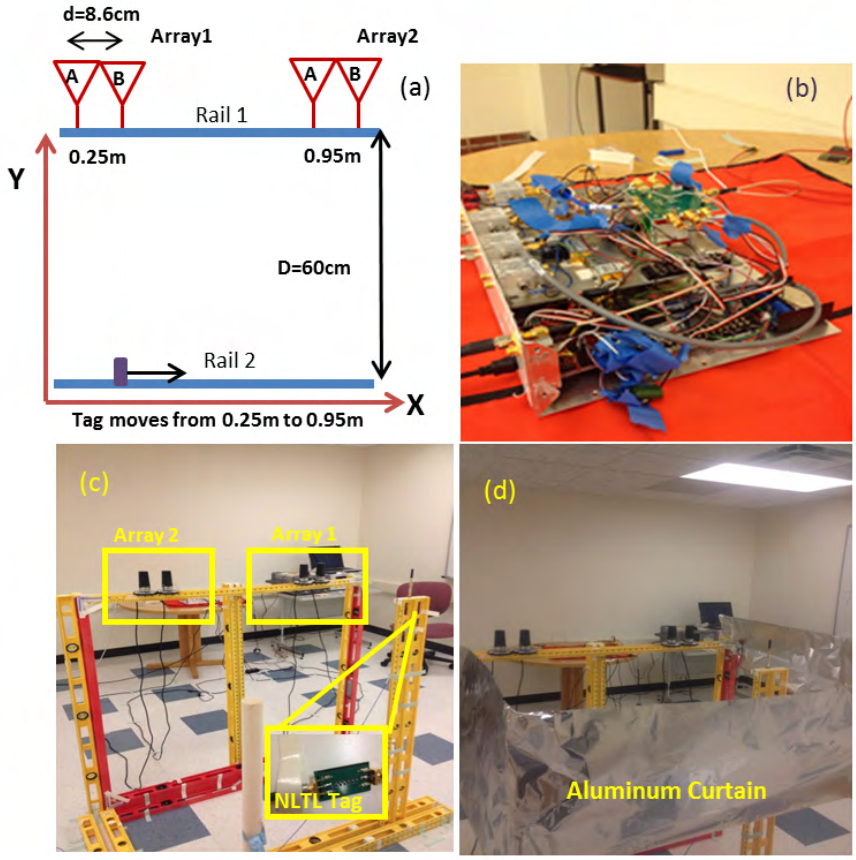

Figure 7.7: Experimental setup: (a) Coordinates in the ranging experiment. (b) The harmonic backscatter reader. (c) The indoor ranging setup. (d) Richer scattering environment was created with aluminum curtain to test the multi-path dominance indicator by the AoA gap.

covered frequency band from 700MHz to 2.7GHz and offered peak and average gain of 0.5dBi and −1.9 dBi respectively in the band of our interests. The centers of the two antennas in the same array were separated by 8.6cm and the centers of the two arrays were by 70cm. We adopted the same 5 harmonic frequencies for HMFCW ranging as the simulation in Table 7.1. The harmonic tag consisted of a 6-stage NLTL on PCB and two Taoglas TG22-series monopole antennas which covered band from 800MHz to 2.2GHz. The peak conversion gain over the frequency of interest at 0dBm input power

Table 7.2: AoA Gap with and without aluminum curtain (AC)

AoA Gap	Mean(RMS)	Median	Maximum
With AC	69.8°	62.7°	112°
Without AC	29.6°	25.9°	42.2°

is -15dBm which translates to at least 5m reading ranging at 4W EIRP and -90dBm receiving sensitivity. The tag was mounted on a rail, sliding from 0.25m to 0.95m. The distance from the tag rail to the antenna rail was 0.6m. The setup was shown in Fig. 7.7 (c) with coordinates shown in Fig. 7.7 (a). Because in our approach only uplink errors affect ranging, in order to calibrate the phase deviation in the uplink, we fed the fundamental frequency through an attenuator to the tag so that the input carrier phase in the downlink was kept fixed when the tag slid along the rail. In Fig. 7.8 (a), the measured signal amplitude ratio between the two antenna elements within each receiving array oscillated between 0.4 and 2.4, which clearly showed the multi-path effect. In an ideal situation without multi-paths, the ratio should be constant at 1. In Fig. 7.8 (b) the measured phase deviation in the uplink was reduced with digital beamforming. In Fig. 7.8 (c), we showed the ranging performance with and without digital beamforming in the HMFCW sparse sensing scheme. The measurement error was computed as the RF measured range subtracting ruler measured range, which might contain calibration uncertainty that made the ranging error without beamforming occasionally smaller. In Fig. 7.8 (d), we created a much richer scattering environment with an aluminum foil curtain (AC) and showed that the extracted AoA gaps were an effective measure of the multi-path dominance in Fig. 7.8 (d). The mean, median and maximum AoA gaps were shown in Table 7.2. By setting threshold for AoA gaps, further control of quality in severe multi-paths can be applied.

The CDF plot of the ranging errors from 450 measurements is shown in Fig. 7.9.

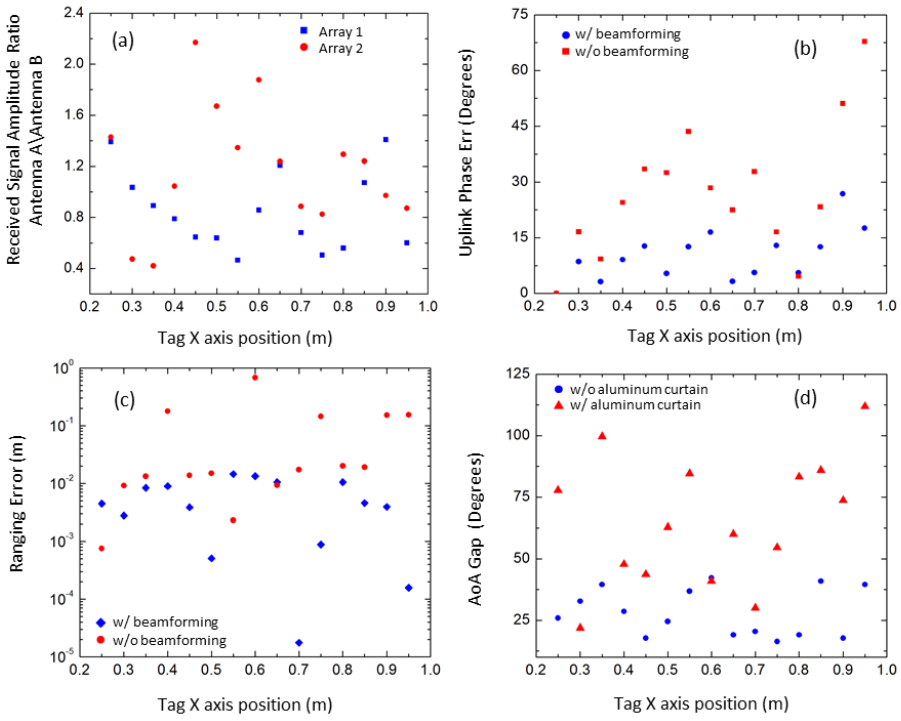

Figure 7.8: Experimental measurements: (a) Received signal amplitude ratio between antennas A and B within each array at 1798MHz to indicate the effect of indoor multi-paths. (b) Reduction of received phase errors at 1798MHz array 1 antenna B for (phase(x) − phase(x=25cm)) with digital beamforming. (c) Ranging errors from HMFCW for 5 frequencies with and without digital beamforming. (d) AoA gaps with and without aluminum curtain.

With the help of quality estimates based on G_{AoA}, unreliable measurements can be effectively rejected, hence resulting in millimeter accuracy ranging even with low-drectivity antennas. The mean, median and maximum ranging errors were shown in Table 7.3.

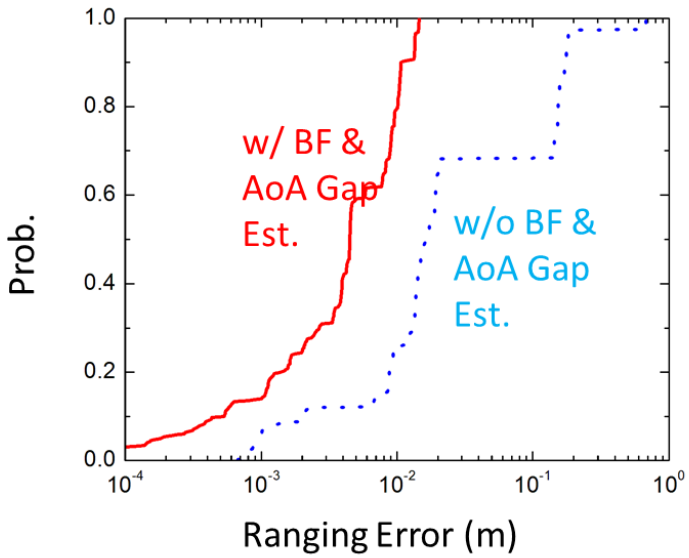

Figure 7.9: CDF plot of ranging error results.

Table 7.3: Ranging errors with and without beamforming & AoA Gap estimates

Error(mm)	Mean(RMS)	Median	Maximum
With BF& AoA estimate	7.48	4.45	14.5
Without BF& AoA estimate	194	17.3	679

7.6 Conclusion

We propose a simple solution by frequency diversity exploration using digital beamforming with two arrays of 2-element antennas in a broadband harmonic multi-static backscatter system. Millimeter-precision ranging in weak LoS environment is achieved in a broad and sparse frequency scheme with omni-directional antennas which offer peak and average gain of 0.5dBi and -1.9dBi respectively. Our system employs sensing frequencies that are separated wider than typical indoor coherence bandwidth and

therefore, we show that ranging robustness can be further enhanced by estimating angles of arrival (AoA) gap, i.e., unreliable measurements from dominant multi-paths can be distinguished and rejected.

CHAPTER 8

DIVERSITY EXPLORATION: SPATIAL DIVERSITY

With the proposed broadband backscatter techniques, not only tagged locating, but also the tagless object locating can be achieved. One way to realize object locating is to put tags on objects [5, 61, 13] with the additional benefit of unique identification through the pre-loaded tag code. The problem of locating an object is transformed to locating the attached tag. As the tag modulates the inquiry signal, by examining the backscatter phase, delay and amplitude, the position information can be extracted. However, in many scenarios an object of interest cannot be assumed tagged, whether intentionally or unintentionally [62, 63, 64]. Locating a tagless object which neither emits nor modulates signal is much more difficult. In this paper, we ask the following question: can we achieve high-accuracy tagless object locating with the assistance of passive landmark RFID tags? Here by high accuracy, we aim at precision within several centimeters. We are not solely interested in large objects such as human body, but other much smaller items such as wallets and hands.

Previous efforts on RF tagless object locating and tracking for indoors had often taken different approaches from tag locating [13, 5] due to unmodulated backscattering [63, 64, 65]. The main drawbacks include:

(1):Difficulty in locating small objects or parts: Compared to human body which has radar cross section (RCS) in the range of square meters [70], household items such as cups or body parts such as hands can be small and obscure, with RCS as small as few tens of square centimeters [28]. In comparison to the whole-body intrusion, signals in the indoor channels can be much less distorted in the scenario like hand pointing or displaced articles.

(2):Low accuracy: Many previous methods relied on received signal strength (RSS) [63, 64, 66, 67], which unlike phase, is not a sensitive function of range [61], offering only sub-meter to meter level accuracy. Other methods found the nearest neighbors of anchor tags and employed trajectory filtering of continuously moving targets [64, 65], still with only sub-meter accuracy due to the granularity limitation.

(3):Proprioceptive training phase: In order to improve RSS accuracy in heavy ambient interference, methods of fingerprinting [63] and the like rely on statistical methods such as Bayesian maximum likelihood estimation. The area of interest is first partitioned into many sub-cells. During the calibration phase, the statistical RSS measurement for each transmitter-receiver pair is recorded when a certain cell has large intrusion and is used as the signature of that cell. In the measurement phase, the newly measured RSS signals are compared to these signatures to identify the cell number. The cell-fingerprinting method requires repetitious scenario training in order to get reliable statistical distribution, similar to proprioception. The reduction of training overhead is however critical for practical applications, especially for indoor environments that are constantly changing due to daily activities.

(4):Relative motion helps but not always available: The locating problem become easier if there is predictable relative motion. The tracking accuracy can be improved by taking advantages of moving objects such as the method in Wi-Vi [68]. The basic working principle is similar to inverse synthetic aperture radar which utilizes relative motion for larger synthesized antenna aperture. However, predictable motion is not always available. We often need to deal with static objects as well.

From the fundamental RF point of view, the permittivity discontinuity introduced by the boundary of an object causes RF signal reflections. The object shape and location can be retrieved from the object reflectivity which is a continuous function in 3D

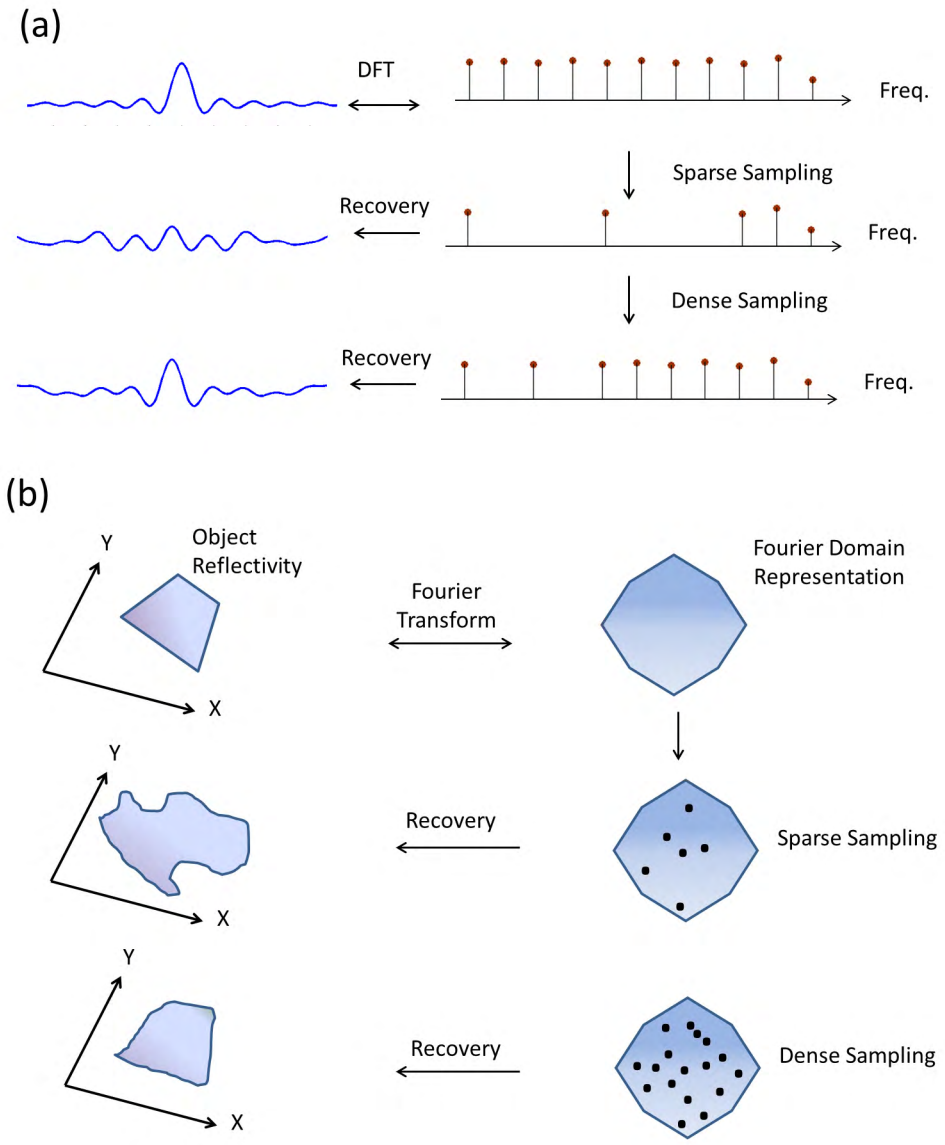

Figure 8.1: (a) Temporal signal recovery via Fourier domain sampling. (b) Object reflectivity can also be recovered by Fourier domain sampling if we find its spectrum.

space. In previous works accurate information of small object location or large object shape cannot be obtained because the system has insufficient information on reflectivity distribution. Recognizing these limitations, in this paper, we propose a system called PhiRadar that can potentially retrieve complete information of object reflectivity in a

low-cost and efficient manner. The key idea of PhiRadar is to use Passive broadband Harmonic tags to build a ubiquitous Indoor Radar system that is able to accurately sample the Fourier domain of object reflectivity.

In Fourier transform, instead of direct time-domain measurements, one can recover the temporal signal through inverse Fourier transform by sampling the frequency domain. The signal recovery quality then depends on how complete the sampling is. Dense sampling usually results in good signal recovery with small distortion while sparse sampling will lead to inaccurate recovery with heavy distortion or ambiguity as shown in Fig. 8.1(a). As reflectivity distribution can be a complete description of object locating, the problem of tagless object locating is essentially the object reflectivity function recovery. If we can convert reflectivity function into its spectrum in the Fourier domain then the rest of our job is to sample in that Fourier domain as wide and dense as possible. The recovery process is illustrated in Fig. 8.1(b), where a complete sampling coverage in Fourier domain can theoretically recover any object location with high complexity.

The design philosophy of PhiRadar is based on:

(1) We need to design a system which can well sample the reflectivity in the Fourier domain.

(2) Complete sampling in the Fourier domain will be achievable when the system complexity goes up.

(3) The system implementation should be low cost, highly flexible and easily imple-

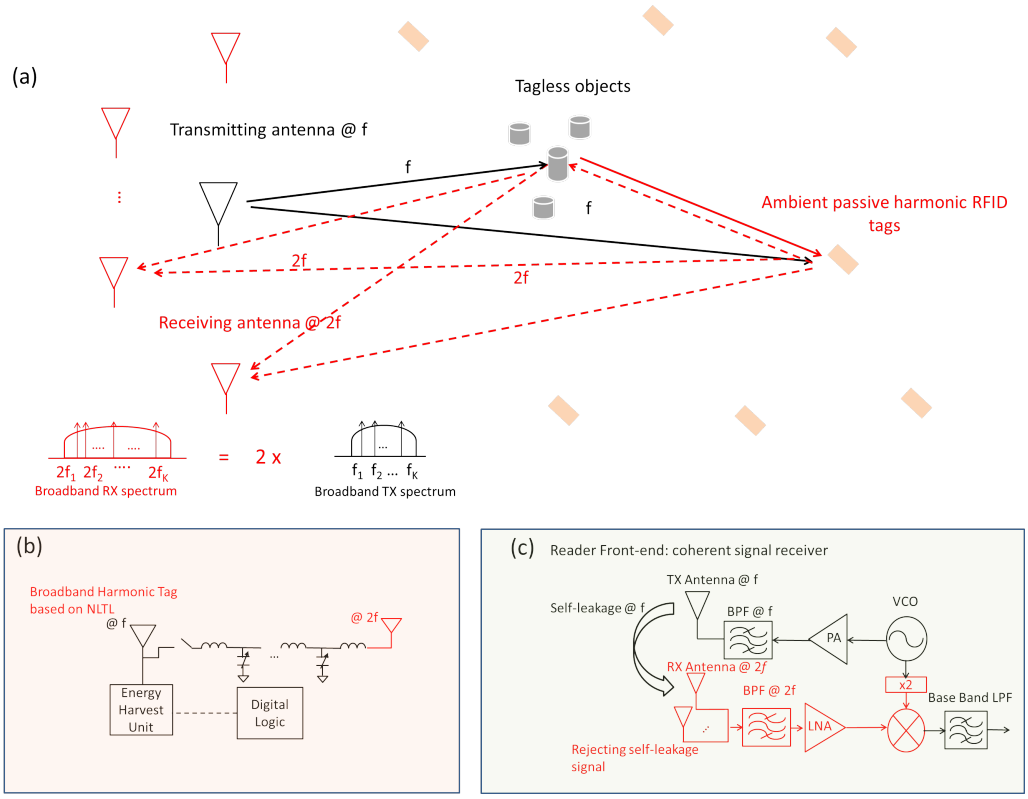

Figure 8.2: (a) Illustration of PhiRadar system. (b) Broadband harmonic tag based on NLTL. (c) Harmonic reader for coherent carrier phase and amplitude measurement.

mentable for indoors.

8.1 PhiRadar overview

The operation of PhiRadar is illustrated in Fig. 8.2(a). The first essential component in PhiRadar is the tessellated passive harmonic RFID tags with broadband backscatter operation. Fig. 8.2(b) shows a design example of such a tag based on distributed nonlinear transmission lines (NLTL) [29, 30]. The landmark tag location can be calibrated beforehand or located by reader using RFID tag locating technology in the calibration phase [31, 69]. The second component of PhiRadar is the broadband harmonic reader with multiple receiving antennas and at least one transmitting antenna. Fig. 8.2(c) shows the

reader block diagram, which encompasses coherent carrier phase and amplitude measurements.

During the tagless locating operation, reader sends out a sequence of inquiry fundamental frequency carriers. The harmonic tags are powered up by the reader inquiry signals and will respond to reader in turn. Each measurement sample will be marked uniquely by the tag location, the reader receiving antenna location and the harmonic backscatter carrier frequency. PhiRadar has the following merits:

(i) Ready synchronization: PhiRadar utilizes backscatter signals from ambient passive harmonic tags, which are powered by the inquiry signal at the fundamental frequency from the reader. PhiRadar receiver antennas listen to the second harmonic generated by the nonlinear passive tags. The local oscillator (LO) in the receiver can be directly generated from the nonlinearity in the reader transmitter power amplifier and thus, the backscatter signal reception is coherent [31].

(ii) Non-self-jamming: One major problem for the conventional backscatter system lies in the strong leakage signal directly from the transmitter to receiver [26, 24, 25]. Because an RFID transmitter needs to power up the ambient tags, thus high power transmission is unavoidable. In the meantime, the tag RCS is often very small. Due to the twice free-space propagation loss, the received backscatter signal is much weaker than the self-leakage interference and the transmitting antenna reflection [61]. PhiRadar receiver listens to , where the interferer on can be easily filtered out. Modulation is only necessary for identification purposes [42].

(iii) Wide angular diversity by low cost ambient tags: If angular diversity is provided by active receivers, the locating system will have significant cost in deployment and maintenance. In contrast, PhiRadar can employ a small number of receivers but a

larger number of ambient tags to achieve wide angular coverage. The price of current commercial passive RFID tags is around $0.1 each.

(iv) High accuracy from broadband operation and wide angular diversity: Bandwidth is the other important resource. The backscatter measurement for each tag-receiver pair at each harmonic frequency forms a sampling point in the Fourier domain. Broadband operation and angular diversity of tag-receiver pairs are the key factors affecting the image resolution and quality. PhiRadar utilizes passive broadband harmonic backscattering that had been recently developed for tag locating [29]. PhiRadar resembles the

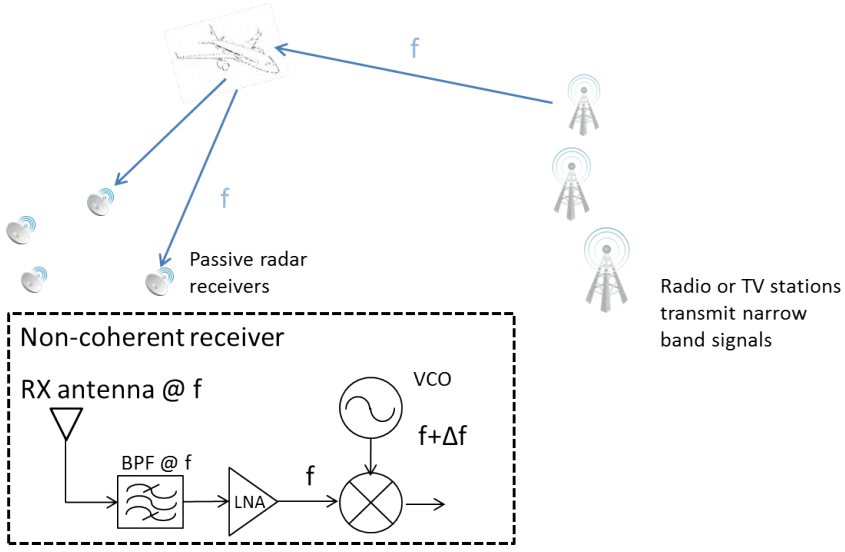

Figure 8.3: Multi-static passive Radar system.

military aircraft surveillance system of multi-static passive radar (MSPR) in theory and practice [71, 72, 73]. The fundamental difference between PhiRadar and MSPR is the diversity resource, which from the non-uniform Fourier domain sampling theory is the key to achieve fine and unambiguous resolution. In MSPR, multiple receivers collect broadcasting signals from nearby radio and TV stations, which are reflected off the airplane as it flies by. As radio and TV stations are not controlled by MSPR, synchronization is very challenging, leading to severe performance degradation. The operation

can also be very opportunistic due to the lack of available radio towers or the limited narrow radio bandwidth. Different from MSPR, PhiRadar is designed towards heavy multi-path interferences for indoor applications. The spatial and frequency diversities are provided by low-cost ambient landmark RFID tags, which can be attached to walls, ceilings, furniture, clothing and other household items. With the growth of IoT, more and more passive tags become available which offer a ready infrastructure for PhiRadar implementation. The broadband harmonic backscatter enables wide frequency diversity without synchronization difficulties.

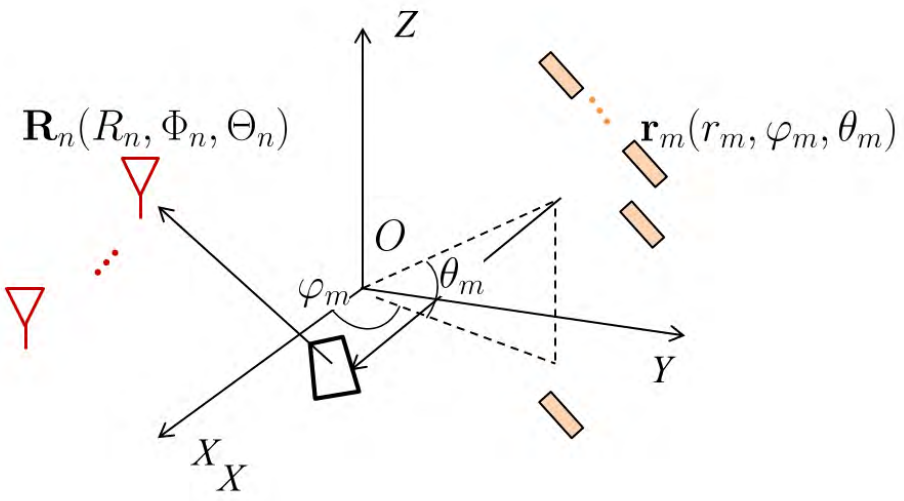

Figure 8.4: Spherical coordinates for the multi-static passive RF locating system.

8.2 Non-uniform sampling in Fourier domain

The location recovery derives from non-uniform sampling in the Fourier domain of target reflectivity. Only a simplified model is presented in this section to avoid losing focus.

The complete signal model will be in Sec. V. For more reference, a similar sampling theory for MSRP can be found in [71, 72, 73].

Let $\mathbf{R}_n$ and $\mathbf{r}_m$ represent the positions of the n-th receiving antenna and the m-th tag, respectively. We first consider the general scattering problem in a spherical coordinate as shown in Fig. 8.4. Assume the observation region is within $|\mathbf{p}| < r_{\max}$. For any tag-receiver pair, $|\mathbf{R}_n|, |\mathbf{r}_m| \gg r_{\max}$ and the signal propagation follows far-field approximation. The reflectivity distribution caused by the tagless targets is denoted as $\sigma(\mathbf{p})$. For simplicity, we first assume that the signal amplitude and phase can be well calibrated, synchronization is ideal, and no other multi-path exists. Assume TX transmits a sequence of L fundamental frequencies of $f_1 < f_2 < \cdots < f_L$. The demodulated second harmonic signal from tag located at $\mathbf{r}$ on frequency $f_{2\text{nd}} \in \{2f_1, 2f_2, \cdots 2f_L\}$ to the target position $\mathbf{p}$ in the observation region can then be simplified as:

$$g(\mathbf{p}) = e^{-j2\pi \mathbf{k}_T \cdot (\mathbf{r}-\mathbf{p})} \tag{8.1}$$

where $\mathbf{K}_T$ is the wavevector of the landmark tag,

$$\mathbf{k}_T = \frac{1}{\lambda_{2\text{nd}}} \frac{\mathbf{r}}{|\mathbf{r}|} \tag{8.2}$$

Similarly, we define $\mathbf{k}_R$ as the wavevector of the receiver located at position $\mathbf{R}$,

$$\mathbf{k}_R = \frac{1}{\lambda_{2\text{nd}}} \frac{\mathbf{R}}{|\mathbf{R}|} \tag{8.3}$$

After calibrating out the phase term associated only with $\mathbf{R}_n$ and $\mathbf{r}_m$, the received signal can be written as

$$\begin{aligned} Z(\mathbf{K}) &= \int\limits_{|\mathbf{p}|<r_{\max}} \sigma(\mathbf{p}) e^{j2\pi \mathbf{K}\cdot\mathbf{p}} \mathrm{d}\mathbf{p} \\ &= \iiint\limits_{x^2+y^2+z^2<r_{\max}^2} e^{j2\pi(xK_x+yK_y+zK_z)} \mathrm{d}x\mathrm{d}y\mathrm{d}z \end{aligned} \tag{8.4}$$

where

$$\mathbf{K} = \mathbf{k}_T + \mathbf{k}_R \tag{8.5}$$

It is worth noting that $Z(\mathbf{K})$ is the Fourier transform of reflectivity distribution. Thus, the target distribution can be recovered from the inverse Fourier transform

$$\begin{aligned} \sigma(\mathbf{p}) &= \int_{\mathbf{K}} Z(\mathbf{K}) e^{-j2\pi \mathbf{K}\cdot\mathbf{p}} \mathrm{d}\mathbf{K} \\ &= \iiint_{\mathbf{K}} Z(K_x, K_y, K_z) e^{-j2\pi(xK_x + yK_y + zK_z)} \mathrm{d}K_x \mathrm{d}K_y \mathrm{d}K_z \end{aligned} \tag{8.6}$$

Target locating can thus be understood as a sampling process: The observation from each tag-receiver pair on each frequency is a sampling point in the Fourier $\mathbf{K}$ domain in Fig. 8.1(b), and the target position recovery is essentially an inverse Fourier transform based on those sampling points. The coverage of the sampling domain $\mathbf{K}$ plays an important role: a dense and comprehensive coverage ensures accurate recovery without ambiguity, while sparse and partial coverage leads to locating inaccuracy and ghost images.

Vector $\mathbf{K}$ can be decomposed into its components along x, y and z axis, i.e., $\mathbf{K} = (K_x, K_y, K_z)$:

$$\begin{cases} K_x &= f_{2\mathrm{nd}} \left(\cos\Theta\cos\Phi + \cos\theta\cos\varphi\right)/c \\ K_y &= f_{2\mathrm{nd}} \left(\cos\Theta\sin\Phi + \cos\theta\sin\varphi\right)/c \\ K_z &= f_{2\mathrm{nd}} \left(\sin\Theta + \sin\theta\right)/c \end{cases} \tag{8.7}$$

where c is the speed of light. Each (K_x, K_y, K_z) represents a point in the Fourier domain in Fig. 8.1(b). In PhiRadar, we have $f_{2\mathrm{nd}} \in \{2f_1, 2f_2, \cdots 2f_L\}$, $\Theta \in \{\Theta_1, \Theta_2, \cdots \Theta_N\}$, $\Phi \in \{\Phi_1, \Phi_2, \cdots \Phi_N\}$, $\theta \in \{\theta_1, \theta_2, \cdots \theta_M\}$ and $\varphi \in \{\varphi_1, \varphi_2, \cdots \varphi_M\}$. From Eq. (8.7), it can be seen that

$$-2f_{2\mathrm{nd}}/c \le K_x, K_y, K_z \le 2f_{2\mathrm{nd}}/c \tag{8.8}$$

and

$$K_x^2 + K_y^2 + K_z^2 \le (2f_{2\mathrm{nd}}/c)^2 \le (4f_L/c)^2 \tag{8.9}$$

The sampling range in the Fourier domain is confined with a sphere with diameter of $8f_L/c$, where f_L is the maximum transmitting fundamental frequency. Thus, the best

achievable resolution in x, y and z directions is [73]

$$(\triangle_x)_{\text{opt}}, (\triangle_y)_{\text{opt}}, (\triangle_y)_{\text{opt}} = c/(8f_L) \tag{8.10}$$

From Eq. (8.7), it can be seen that the frequency diversity $\{f_{2\text{nd}l}\}$ as well as angular diversity of receivers $\{\Theta_n, \Phi_n\}$ and tags $\{\theta_m, \varphi_m\}$ are two valuable sampling resources. These two coupled resources together determine the coverage of the Fourier domain, whose radius is determined by the maximum sensing frequency. Since we only have discrete samples, the inverse Fourier transform in Eq.(8.6) is inexact. For a fixed receiver tessellation $\{\Theta_n, \Phi_n\}$, assuming the frequency and tag positions $\{f_{2\text{nd}l}, \theta_m, \varphi_m\}$ have uniform distributions in $[f_{\min}, f_{\max}]\times[0, 2\pi]\times[0, 2\pi]$, according to importance sampling (IS) [74],

$$\sigma_n(\mathbf{p}) \propto \sum_{l=1}^{L}\sum_{m=1}^{M} |J_{l,m,n}| Z(\mathbf{K}_{l,m,n}) e^{-j2\pi \mathbf{K}_{l,m,n}\cdot\mathbf{p}} \tag{8.11}$$

where $J_{l,m,n}$ is the Jacobian matrix element as

$$J_{l,m,n} = -\frac{f_{2\text{nd}l}^2}{c^3}\cos\theta_m \begin{bmatrix} 1 + \cos\Theta_n \cos\theta_m \cos(\Phi_n - \varphi_m) \\ + \sin\Theta_n \sin\theta_m \end{bmatrix} \tag{8.12}$$

From Eq. (8.11), $\sigma(\mathbf{p})$ is computed through averaging information collected by all N receivers

$$\sigma(\mathbf{p}) \propto \sum_{l=1}^{L}\sum_{m=1}^{M}\sum_{n=1}^{N} |J_{l,m,n}| Z(\mathbf{K}_{l,m,n}) e^{-j2\pi \mathbf{K}_{l,m,n}\cdot\mathbf{p}} \tag{8.13}$$

8.3 Tagless object position recovery in PhiRadar

In this section, the practical signal model, operation and locating algorithm of PhiRadar are assembled together. The algorithm adopts a nulling process to cancel out strong reflections from ground and walls, as well as a differential receiving strategy to cancel downlink multi-path distortions.

8.3.1 Basic signal model

For each sampling period, among the M ambient tags that have been identified and located during the initialization phase $(\mathrm{Tag}_1, \mathrm{Tag}_2, \cdots \mathrm{Tag}_M)$, one tag is selected at a time to respond to the reader to reduce tag-to-tag interference. Assume TX transmits a sequence of L fundamental frequencies of $f_1 < f_2 < \cdots < f_L$

$$u_l(t) = U_l e^{(j2\pi f_l t + j\varsigma_l)} \tag{8.14}$$

where U_l and ς_l are the amplitude and initial phase of the inquiry signal $u_l(t)$ on the l-th fundamental frequency f_l. The m-th tag at location $\mathbf{r}_m$ listens to $u_l(t)$ and generates a corresponding second harmonic $s_{l,m}(t)$

$$\begin{aligned} s_{l,m}(t) &= S_l(\mathbf{r}_m) e^{(j4\pi f_l t + j\phi_{l,m})} \\ S_l(\mathbf{r}_m) &= \alpha_{l,m} U_l^2 |\mathrm{PL}_{l,m}| \\ \phi_{l,m} &= 2(\varsigma_l - \angle \mathrm{PL}_{l,m} + \triangle\xi_{l,m}) + \rho_{l,m} \end{aligned} \tag{8.15}$$

$S_l(\mathbf{r}_m)$ denotes the second harmonic amplitude at the tag output which is proportional to the product of the square of fundamental signal amplitude U_l and downlink propagation loss $|\mathrm{PL}_{l,m}|$. Coefficient $\alpha_{l,m}$ depends on the nonlinear circuit characteristics. Larger $\alpha_{l,m}$ corresponds to better harmonic generation efficiency for the nonlinear circuits. $\phi_{l,m}$ is the initial output harmonic signal phase for the l-th frequency and the m-th tag, which depends on ς_l, the downlink propagation phase delay $\angle \mathrm{PL}_{l,m}$, the phase error $\triangle\xi_{l,m}$ induced in downlink multi-paths and the delay $\rho_{l,m}$ caused by harmonic generation circuits.

The reader has N receiving antennas. After filtering out the self-interference and direct reflections around f_l, the received signal on $2f_l$ consists of two parts. For simplicity, we first assume SNR is sufficiently high so the effect of circuit noises can be temporarily neglected. We thus focus only on phase and amplitude errors caused by indoor multi-paths. The first part consists of the signal propagating along the line-of-sight (LoS) path

as well as the multi-paths in a typical indoor environment, except for the multi-paths caused by the objects of interest in the observation region from the m-th tag to the n-th receiving antenna. Let $\mathbf{R}_n$ represent the position of n-th receiving antenna, the first part of the received signal can be written as

$$\tilde{q}_{l,m,n}(t) = s_{l,m}(t)\tilde{h}_{l,m,n} \tag{8.16}$$

where

$$\tilde{h}_{l,m,n} = \frac{\Gamma_{l,m,n} G^{\text{tag}}_{l,m}(\mathbf{R}_n - \mathbf{r}_m) G_{l,n}(\mathbf{r}_m - \mathbf{R}_n)}{8\pi \frac{f_l}{c} |\mathbf{r}_m - \mathbf{R}_n|} e^{j\left(\frac{-4\pi f_l |\mathbf{r}_m - \mathbf{R}_n|}{c} + \triangle\delta_{l,m,n}\right)} \tag{8.17}$$

The multi-path effect is modeled here as $\Gamma_{l,m,n}$ and $\triangle\delta_{l,m,n}$ to express the change in amplitude and phase with respect to a single-LoS channel model. The amplitude gain of the tag and reader receiving antennas on $2f_l$ are denoted as $G^{tag}_{l,m}(\mathbf{r})$ and $G_{l,n}(\mathbf{r})$, where the propagation direction is designated by the vector $\mathbf{r}$. The second part consists of the uplink signals reflected from tagless objects of interest within the observation region. Assume we have I objects with strong scattering. The reflected signals can be written as

$$q_{l,m,n}(t) = s_{l,m}(t) h_{l,m,n} \tag{8.18}$$

where

$$h_{l,m,n} = \sum_{i=1}^{I} \frac{\beta_i G^{tag}_{l,m}(\mathbf{p}_i - \mathbf{r}_m) G_{l,n}(\mathbf{p}_i - \mathbf{R}_n)}{16\pi^{\frac{3}{2}} \frac{f_l}{c} |\mathbf{r}_m - \mathbf{p}_i| |\mathbf{R}_n - \mathbf{p}_i|} e^{\frac{-j4\pi f_l (|\mathbf{r}_m - \mathbf{p}_i| + |\mathbf{R}_n - \mathbf{p}_i|)}{c}} \tag{8.19}$$

The position of the i-th object is $\mathbf{p}_i$ and β_i is the complex amplitude proportional to the object RCS. The total received signal $Q_{l,m,n}(t)$ combining the two parts is

$$Q_{l,m,n}(t) = \tilde{q}_{l,m,n}(t) + q_{l,m,n}(t) \tag{8.20}$$

8.3.2 Differential receiving for $\phi_{l,m}$ cancellation

Because the initial phase $\phi_{l,m}$ is unknown, instead of estimating this term, we adopt differential receiving strategy for cancellation. The advantage of differential receiving is

that the phase error induced by the downlink multi-paths, which is incorporated into $\phi_{l,m}$ in Eq. (8.15), can be canceled out. We only see the phase error induced by the uplink multi-paths. For the n-th receiving antenna and the m-th tag, v denotes another receiving antenna ($v \neq n$). We can compute the ratio of $Q_{l,m,n}(t)$ to $Q_{l,m,v}(t)$

$$H_{l,m,n,v} = \frac{Q_{l,m,n}(t)}{Q_{l,m,v}(t)} = \frac{\tilde{h}_{l,m,n}(1 + h_{l,m,n}/\tilde{h}_{l,m,n})}{\tilde{h}_{l,m,v}(1 + h_{l,m,v}/\tilde{h}_{l,m,v})} \tag{8.21}$$

The ratio H is independent of the unknown initial phase $\phi_{l,m}$ but only dependent on the channel coefficient h , and thus can be calibrated during the absence of the tagless objects of interest in advance. This calibration process can be done quickly, which is equal to one measurement for each f_l. Let Q^c denotes the measurement in the absence of targets, then

$$Q^c_{l,m,n}(t) = \tilde{q}^c_{l,m,n}(t) = s^c_{l,m}(t)\tilde{h}_{l,m,n} \tag{8.22}$$

and

$$H^c_{l,m,n,v} = \frac{Q^c_{l,m,n}(t)}{Q^c_{l,m,v}(t)} = \frac{\tilde{h}_{l,m,n}}{\tilde{h}_{l,m,v}} \tag{8.23}$$

Define $z_{l,m,n}$ as

$$\begin{aligned} z_{l,m,n} &= \frac{1}{N}\sum_{v=1}^{N} \frac{H_{l,m,n,v} - H^c_{l,m,n,v}}{H^c_{l,m,n,v}} \\ &= \frac{1}{N}\sum_{v=1}^{N} \frac{h_{l,m,n}/\tilde{h}_{l,m,n} - h_{l,m,v}/\tilde{h}_{l,m,v}}{1 + h_{l,m,v}/\tilde{h}_{l,m,v}} \end{aligned} \tag{8.24}$$

For objects with small RCS,

$$\frac{h_{l,m,v}}{\tilde{h}_{l,m,v}} \ll 1 \tag{8.25}$$

therefore

$$z_{l,m,n} = \frac{1}{N}\sum_{v=1}^{N}\left(\frac{h_{l,m,n}}{\tilde{h}_{l,m,n}} - \frac{h_{l,m,v}}{\tilde{h}_{l,m,v}}\right) \tag{8.26}$$

We can then establish the differential receiving from the m-th tag to the n-th receiving antenna. Here in Eq. (8.26),

$$\frac{h_{l,m,n}}{\tilde{h}_{l,m,n}} = \frac{e^{j(-\triangle\delta_{l,m,n} + \frac{4\pi f_l |\mathbf{r}_m - \mathbf{R}_n|}{c})}}{\Gamma_{l,m,n}} \times \sum_{i=1}^{I} \beta_i \alpha(\mathbf{p}_i, \mathbf{r}_m, \mathbf{R}_n) e^{-j\frac{4\pi f_l(|\mathbf{r}_m - \mathbf{p}_i| + |\mathbf{R}_n - \mathbf{p}_i|)}{c}} \tag{8.27}$$

where

$$\alpha(\mathbf{p}_i, \mathbf{r}_m, \mathbf{R}_n) = \frac{|\mathbf{r}_m - \mathbf{R}_n|}{2\pi^{\frac{1}{2}}|\mathbf{r}_m - \mathbf{p}_i||\mathbf{R}_n - \mathbf{p}_i|} \times \frac{G^{\text{tag}}_{l,m}(\mathbf{p}_i - \mathbf{r}_m)G_{l,n}(\mathbf{p}_i - \mathbf{R}_n)}{G^{\text{tag}}_{l,m}(\mathbf{R}_n - \mathbf{r}_m)G_{l,n}(\mathbf{r}_m - \mathbf{R}_n)} \tag{8.28}$$

8.3.3 Reconstruction

By using estimated LoS distance between the m-th tag and the n-th receiving antenna $|\mathbf{r}_m - \mathbf{R}_n|_{\text{est}}$,

$$Z_{l,m,n} = z_{l,m,n} \exp\left(-j\frac{4\pi f_l}{c}|\mathbf{r}_m - \mathbf{R}_n|_{\text{est}}\right) \tag{8.29}$$

The locations of the tagless objects are recovered by computing the weighted sum of $\{Z_{l,m,n}\}$. Let $|F(\mathbf{p})|^2$ represent the recovery image. For each point of location p within the observation region, we can compute

$$F(\mathbf{p}) = \sum_{l=1}^{L}\sum_{m=1}^{M}\sum_{n=1}^{N} w_{l,m,n}Z_{l,m,n}e^{j\frac{4\pi f_l(|\mathbf{r}_m-\mathbf{p}|+|\mathbf{R}_n-\mathbf{p}|)}{c}} \tag{8.30}$$

In imaging function of $|F(\mathbf{p})|^2$, high intensity regions correspond to locations of the tagless objects. $w_{l,m,n}$ represents the weight. Under ideal situation without multi-path effects in Eq. (8.17) and the estimated distance between the m-th tag and the n-th receiving antenna is precise (i.e.,$\Gamma_{l,m,n} = 1$, $|\mathbf{r}_m - \mathbf{R}_n|_{\text{est}} = |\mathbf{r}_m - \mathbf{R}_n|$ and $\triangle\delta_{l,m,n} = 0$), Eq. (8.29) can be simplified as

$$Z_{l,m,n} = \sum_{i=1}^{I}\beta_i\alpha(\mathbf{p}_i, \mathbf{r}_m, \mathbf{R}_n)e^{-j\frac{4\pi f_l(|\mathbf{r}_m-\mathbf{p}_i|+|\mathbf{R}_n-\mathbf{p}_i|)}{c}} + \triangle Z_{l,m,n} \tag{8.31}$$

where

$$\triangle Z_{l,m,n} = \frac{1}{N}\sum_{v=1}^{N}\sum_{i=1}^{I} -\beta_i\alpha(\mathbf{p}_i, \mathbf{r}_m, \mathbf{R}_v)e^{-j\frac{4\pi f_l(|\mathbf{r}_m-\mathbf{p}_i|+|\mathbf{R}_v-\mathbf{p}_i|)}{c}} \tag{8.32}$$

The interference term in Eqs. (8.31) and (8.32) is reduced through averaging among all N receiving antennas. By comparing Eqs. (8.30) and (8.13), it can be seen that when the weight in Eq. (8.17) is chosen as

$$w_{l,m,n} = |J_{l,m,n}| \tag{8.33}$$

$|F(\mathbf{p})|^2$ is essentially an extended form of Eq. (8.13), which however does not require far-field assumption.

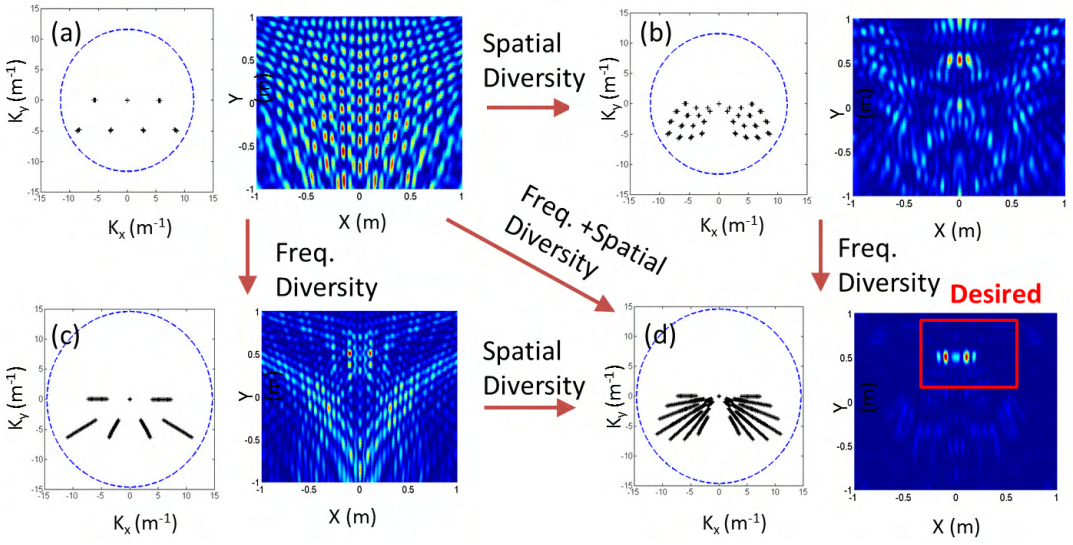

Figure 8.5: Effects of Fourier domain sampling coverage on locating 2 adjacent targets by the imaging function $|F(\mathbf{p})|^2$ in Eq. (8.17). PhiRadar uses both frequency and spatial diversity to enhance Fourier domain sampling for accurate and unambiguous location estimations.

The Fourier domain coverage effect on image recovery is shown in Fig. 8.5. The simulation setups vary with different number of tags M (located at $|\mathbf{r}_m| = 1.5$m, and $\angle\mathbf{r}_m$ equally distributed in $[0, \pi/3]$ and $[2\pi/3, \pi]$), number of receiving antennas N (located at $|\mathbf{R}_n| = 1.5$m, and $\angle\mathbf{R}_n$ equally distributed in $[4\pi/3, 5\pi/3]$) and number of frequency L whose second harmonic centered around 1.7GHz with various percentage bandwidth BW%. The $(M, N, L, \text{BW}\%)$ for four cases in the simulation are: (a) $(4, 2, 5, 6\%)$ (b) $(8, 4, 5, 6\%)$ (c) $(4, 2, 21, 59\%)$ and (d) $(8, 4, 21, 59\%)$. The two adjacent targets are located at $[-0.1\text{m}, 0.5\text{m}]$ and $[0.1\text{m}, 0.5\text{m}]$ which have RCS of 0.05m^2.

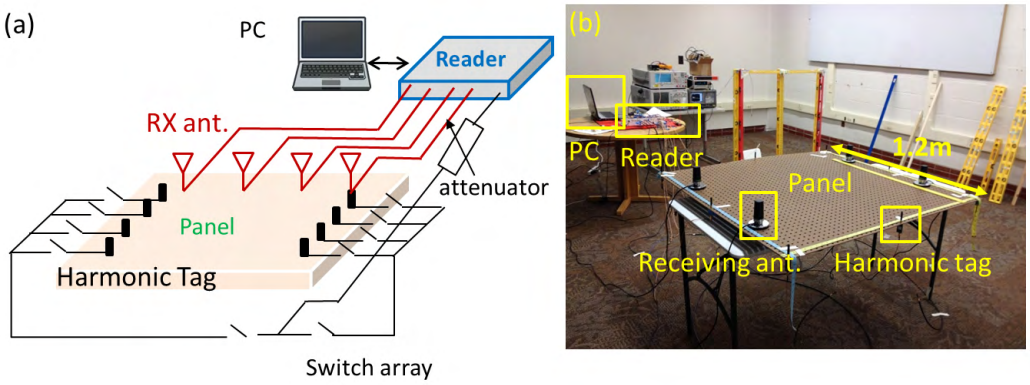

Figure 8.6: Experimental setup: (a) Schematic;(b) Photo.

8.4 Experimental verification

We verify the PhiRadar operation through experiments in a prototype system. The setup is shown in Fig. 8.6. This prototype consists of 8 harmonic tags and receiving antennas on a 1.2m $\times$ 1.2m wooden pegboard to construct an 8×4 tag-receiver uplink multiple-input-multiple-output (MIMO) channel. The tag design is based on NLTL, which has a microwave periodic structure for broadband harmonic generation. We adopt 19 frequencies with the harmonic frequency spanning from 1.74GHz to 2.16GHz. The minimum frequency separation is 20MHz, greater than typical indoor coherence bandwidth [60]. As the first concept demonstration, the current tag is not integrated with digital logic for multi-access modulation and has no RF-to-DC converter. In order to enable multiplexing, we utilize an RF switch array to feed the fundamental signal to tags through co-axis cables with programmable attenuators to emulate propagation loss. The RF switch array is controlled by the microcontroller to single out one tag at a time. As PhiRadar adopts differential receiving techniques, the multi-path effect in the downlink is canceled out. Hence, the present downlink implementation will not much affect the

experimental result. Downlink multi-path can actually be beneficial to facilitate power transfer in certain scenario. Fig. 8.7 showed the 2D position recovery of single and

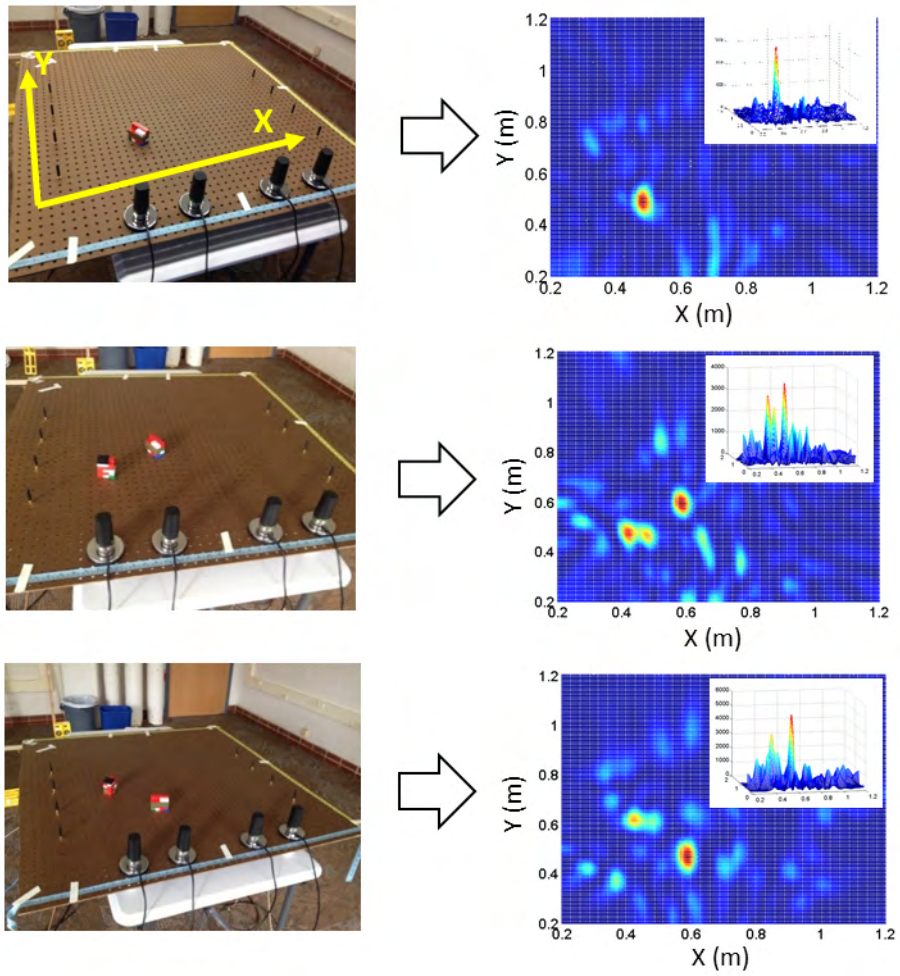

Figure 8.7: 2D position recovery of small objects for the single and dual target cases.

dual target cases. The targets were made of Lego bricks with feature dimension around 5cm. The Fourier domain coverage was shown in Fig. 8.8(a). To better understand the accuracy of PhiRadar locating capability, we varied the single Lego brick position for 35 different locations across the table. The cumulative probability plot for measurement errors in X and Y directions as well as the total errors were shown in Fig. 8.8(b). The

locating errors were below 3cm for 90% of measurements while the maximum error was 8cm. It is worth noticing that for this particular setup, as the Fourier domain coverage was only in the lower hemisphere, errors along the X axis should be smaller than errors along the Y axis. Indeed the 90% error along X and Y axes were 1.2cm and 2.8cm . The X error was roughly half of the Y error, which follows the theory in Sec. 8.2.

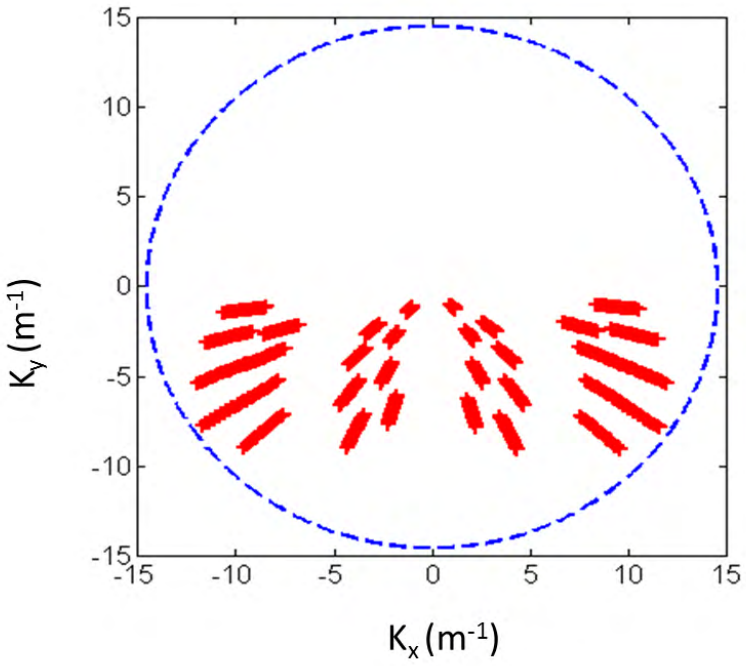

Figure 8.8: Fourier domain samples in experiment.

8.5 Conclusion

In this Chapter, we proposed the concept of PhiRadar, which extends the conventional multi-static passive radar system into indoor environment for tracking tagless targets. By harnessing angular diversity provided by passive RFID landmark tags and frequency

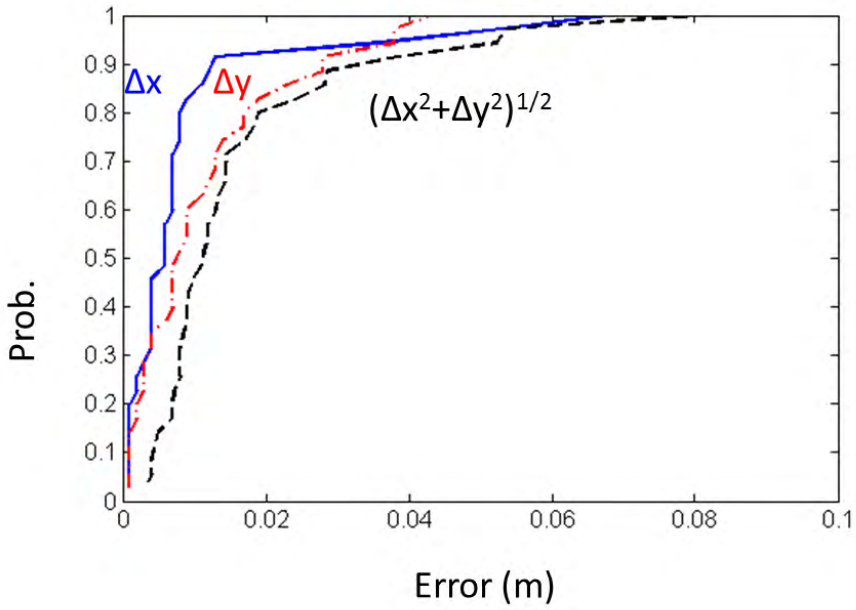

Figure 8.9: CDF of experiment measurement errors.

diversity by broadband harmonic backscattering, PhiRadar shows high accuracy for tagless locating even with target size as small as and good robustness against undesirable multi-paths. With such high resolution, PhiRadar is able to be extended to large number of large or small objects for ubiquitous tagless indoor locating. We present the fundamental theory, followed by experimental verification in a prototype system. The tag was not yet fully integrated with digital circuits for tag multiplexing. From the receiver point of view, the present multiplexing downlink emulation does not affect our location recovery algorithm, because the receiving is differential, i.e., the downlink signal and its associated multi-paths are always canceled out. As the harmonic backscatter technique can also locate tags accurately, fast and automatic calibration of landmark tags can be implemented in future designs.

CHAPTER 9

CONCLUSION

The thesis demonstrates the capability of a new class of indoor locating approach: passive broadband harmonic RF backscatter. The proposed approach is much more effective than the conventional RFID approach. Fig. 9.1 compares the works presented in this thesis with the state of art in the literature. The proposed works discussed in this thesis and the state of art works in Fig. 9.1 are listed in Tables 9.1 and 9.2 below.

Our proposed harmonic backscatter RF locating approach has shown much higher locating accuracy in 1D ranging measurement, 2D localization measurements for both tag locating and RFID assisted tagless object locating, and real-time 3D locating measurements. More importantly, the proposed approach has overcome the traditional constraints on RFID locating which include but not limited to: (1) Requirement of relative motion; (2) Requirement of reference tags or anchor nodes deployment; (3) 2D limited methods; (4) Rigid antenna configuration. To the best of our knowledge, we are the first to achieve real-time 3D passive device locating within centimeter accuracy in indoor environment.

Table 9.1: Our works discussed in this thesis which are listed in Fig. 9.1

Works.	Reference number or Chapter number
Ma, Submitted	Chapter 5 and [75]
Ma, TMTT	[29]
Ma, Globecom	Chapter 6 and [77]
Ma, IMS	Chapter 7 and [31]
Ma, Infocom	Chapter 8 and [76]

Table 9.2: State of art works which are listed in Fig. 9.1

Works.	Reference number
Ni, PerCom	[1]
Lanzisera, Intelligent Solution Embedded Sys.	[16]
Li, IEEE RFID	[48]
Nikitin, IEEE RFID	[5]
Zhou, IEEE Antenna Propagation Letter	[3]
Viikari, IEEE Sensor	[4]
Williams, IEEE RFID	[11]
Azzouzi, IEEE RFID	[50]
Zhang, IEEE TDS	[64]
Misen, IEEE RFID	[17]
Xu, IPSN	[63]
Han IEEE Infocom	[65]
Zhao, IEEE RFID	[19]
Anee, IEEE TMTT	[20]
Wang, Sigcomm	[18]
Wang, Mobicom	[13]
Scherhaufl, IEEE IMS	[55]
Liu, IEEE Infocom	[15]
Wang, Sigcomm	[9]
Yang, Mobicom	[8]

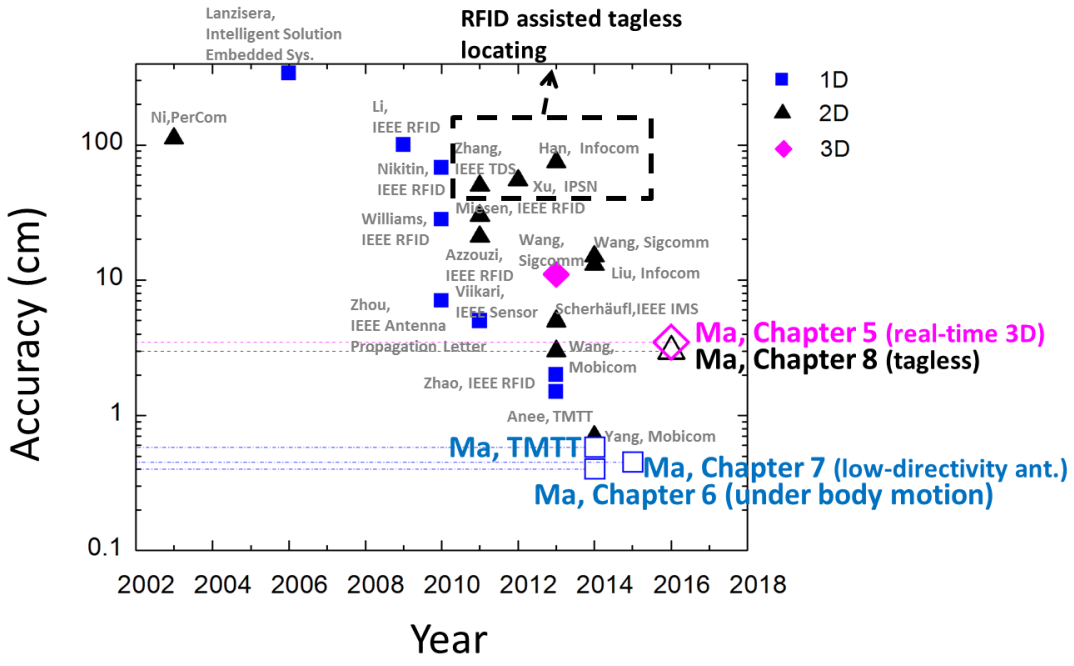

Figure 9.1: Comparison of proposed works with the state of art

I believe this thesis is only a start for harmonic-backscatter-based indoor locating systems and there are a lot of room for further improvement such as wireless multiplexing to track multiple tags simultaneously, systems with even broader bandwidth to handle extremely tough environments and multi-band operations with full FCC regulation compliance.

9.1 Future works

For the future works, there are multiple interesting and important things to be done.

(1) Locating multiple tags simultaneously: One of the big advantages of RFID lo-

cating is to combine an object ID with its accurate location information. Nowadays, with state-of-art RFID technology, we can quickly retrieve the IDs of hundreds of objects. The wireless multiplexing capability can be readily integrated with the proposed passive broadband harmonic RF backscatter locating techniques which opens the possibility of getting accurate location information from hundreds of objects simultaneously. The wireless multiplexing capability is highly desired which can greatly help constructing novel human machine interface (e.g. tracking multiple fingers) and enhancing robotic recognition capability.

(2) RFID assisted indoor imaging system: Chapter 8 has revealed the possibility of constructing a high resolution imaging system utilizing ambient passive RFID devices based on the non-uniform Fourier domain sampling theory. Due to the use of passive RFID tags, such imaging systems will be extremely low-cost and flexible and can be deployed ubiquitously to help human and animal health monitoring, security check and intrusion detection. To achieve such a task, a passive harmonic RFID system that works over several GHz frequency range is desired to further increase the frequency diversity.

(3) Harmonic RFID tag and reader implementation on CMOS IC: Custom CMOS IC provides a low cost way for mass production. As has been shown in Chpater 3, NLTL can be easily implemented on CMOS processes which offer excellent harmonic generation efficiency. Currently for RFID reader IC integration, one big challenge is the adoption of a bulky magnetic circulator to separate the Tx and Rx in current RFID reader architecture. A circulator is not CMOS compatible since it requires ferromagnetic material to create non-reciprocity [79]. Recently, there has been interesting efforts trying to exploit time varying system to build a non-reciprocal phase response of a two-port phase-shifting N-path filter which is used to implement an on-chip circulator [79]. However, the maximum allowed Tx power is about -7dBm which is much lower

than what is needed for RFID transmission. As in the proposed harmonic backscatter approach, a circulator is not required, hence the reader architecture is more CMOS compatible compared to the conventional RFID reader which can help further lower the cost in mass production.

BIBLIOGRAPHY

[1] L. M. Ni, Y. Liu, Y. C. Lau and A. P. Patil. Landmarc: indoor location sensing using active RFID. In *Proc. IEEE PERCOM*, 2003.

[2] J. Zhou and J. Shi. RFID localization algorithm and applications, a review. *J. Intell. Manuf.*, vol. 20, no.6, pp. 695-707, Dec 2009.

[3] C. Zhou and J. D. Griffin Accurate phase based ranging measurement for backscatter RFID tags. *IEEE Antennas Wireless Propag. Lett.*, vol. 11, pp. 152-155, Jan. 2012.

[4] V. Viikari, P. Pursula and K. Jaakkola. Ranging of UHF RFID tag using stepped frequency read-out. *IEEE Sensors J.*, vol. 10, no. 9, pp. 1535-1539, Sept. 2010.

[5] P. Nikitin, R. Martinez, S. Ramanurthy, H. Leland, G. Spiess and K. V. R. Rao. Phase based spatial identification of UHF RFID tags. In *Proc. IEEE Int. Conf. RFID*, 2010.

[6] C. Xu, et al. Improving rf-based device-free passive localization in cluttered indoor environment through probabilistic classification methods. In *ACM/IEEE International Conference on Information Processing in Sensor Networks (IPSN)*, 2012.

[7] S. Radiom, et al. Far-field on-chip antennas monolithically integrated in a wireless-powered 5.8-ghz downlink/uwb uplink rfid tag in 0.18-um standard cmos. *IEEE Journal of Solid State Circuits*, vol.45, no.9, pp. 1746 - 1758, Sept. 2010.

[8] L. Yang, Y. Chen, X. Li, C. Xiao, M. Li and Y. Liu. Tagoram: Real-time tracking of mobile RFID tags to high precision using cots devices. In *ACM MOBICOM*, 2014.

[9] J. Wang, D. Vasisht and D. Katabi. RF-IDraw: virtual touch screen in the air using RF signals. In *ACM SIGCOMM*, 2014.

[10] D. Tse and P. Viswanath. Fundamentals of wireless communication. 2005.

[11] C. H. Williams, B. Grant, X. Liu, Z. Zhang and P. Kumarl. Accurate localization of RFID tags using phase difference. In *Proc. IEEE Int. Conf. RFID*, 2010.

[12] D. Arnitz, K. Witrisal and U. Muehlmann. Multi-frequency continuous-wave radar approach to ranging in passive UHF RFID. *IEEE Tran. Microw. Theory Tech.*, vol. 57, no. 5, pp.1398-1405, May 2009.

[13] J. Wang, F. Alib, R. Knepper, D. Katabi and D. Rus. RF-compass: Robot object manipulation using RFIDs. In *ACM MOBICOM*, 2013.

[14] T. Li, C. An, Z. Tian, A. T. Campbell and X. Zhou. Human sensing using visible light communication. In *ACM MOBICOM*, 2014.

[15] L. Liu, et al. Anchor-free backscatter positioning for RFID tags with high accuracy. In *IEEE INFOCOM*, 2014.

[16] S. Lanzisera, D. Lin and K. S. J. Pister. RF time of flight ranging for wireless sensor networks localization. In *Workshop on Intelligent Solutions in Embedded Systems. Dig.*, 2006.

[17] R. Miesen, et al. Holographic localization of passive UHF RFID transponders. In *Proc. IEEE Int. Conf. RFID*, 2011.

[18] J. Wang and D. Katabi. Dude, where is my card? RFID positioning that works with multipath and non-line of sight. In *ACM SIGCOMM*, 2013.

[19] Y. Zhao and J. R. Smith A battery-free RFID-based indoor acoustic localization platform In *Proc. IEEE Int. Conf. RFID*, 2013.

[20] R. Anee and N. Karmakar Chipless RFID tag localization *IEEE Tran. Microw. Theory Tech.*, vol. 61, no. 11, pp. 4008-4017, Nov. 2013.

[21] T. Le, K. Mayaram and T. Fiez Efficient far-field radio frequency energy harvesting for passively powered sensor networks *IEEE J. Solid-State Circuits*, vol. 43, no. 5, pp. 1287-1302, May 2008.

[22] J. Fitch. Synthetic aperture radar. 1988.

[23] G. Durgin, et al. Modulation and sensitivity limits for backscatter receivers. In *Proc. IEEE Int. Conf. RFID*, 2013.

[24] S. Lee, et al. A new TX leakage-suppression technique for an RFID receiver using a dead-zone amplifier. In *ISSCC Tech. Dig.*, 2013.

[25] J. Lee, et al. A UHF mobile RFID reader IC with self-leakage canceller. In *IEEE RFIC Symp.*, 2007.

[26] P. B. Khannur, et al. A universal UHF RFID reader IC in 0.18-m CMOS technology. *IEEE J. Solid-State Circuits*, vol. 43, no. 5, pp. 1146-1155, May 2008.

[27] Y. Ma and E. C. Kan. Multipath interference reduction in NLTL tags. In *Proc. of IEEE Int. Wireless Symp.*, 2013.

[28] D. M. Pozar. Microwave Engineering. 2011.

[29] Y. Ma and E. C. Kan. Accurate Indoor Ranging by Broadband Harmonic Generation in Passive NLTL Backscatter Tags. *IEEE Tran. Microw. Theory Tech.*, vol. 62, no. 5, pp. 1249-1261, May 2014.

[30] F. Yu, Y. Ma and E. C. Kan. Reflective nonlinear transmission lines for single-antenna non-self-jamming RFID. In *IEEE MTT-S Intl. Microwave Symp. Dig.*, 2011.

[31] Y. Ma and E. C. Kan. Passive ranging with low directivity antenna with quality estimate. In *IEEE MTT-S Intl. Microwave Symp. Dig.*, 2015.

[32] G. Li, D. Amitz, R. Ebelt, U. Muehlmann, K. Witrisal and M. Vossiek. Bandwidth dependence of CW radar ranging to UHF RFID tags in severe multipath environments. In *Proc. IEEE Int. Conf. RFID*, 2011.

[33] T. H. Lee. The Design of CMOS Radio-frequency Integrated Circuits. Cambridge University Press, 1998.

[34] Panasonic. High frequency use (non magnetic) RF/RE/ND/NC/NA Catalog, datasheet. Sept. 2012.

[35] Taoglas Antenna Solutions. http://www.taoglas.com/images/product-images/original_images/TL10.1HH11W.pdf.

[36] Taoglas Antenna Solutions. http://www.taoglas.com/images/product_images/original_images/TG.22.0111.pdf.

[37] HC-06 Bluetooth Module. https://www.olimex.com/Products/Components/RF/BLUETOOTH-SERIAL-HC-06/resources/hc06.pdf, 2016.

[38] Impinj R420. http://www.impinj.com/products/readers/. 2016.

[39] National Instrument. http://www.ni.com/labview/. 2016.

[40] STMicroelectronics. http://www2.st.com/content/st_com/en/products/microcontrollers/stm32-32-bit-arm-cortex-mcus. 2016.

[41] S. Sugiura and H. Iizuka. Reactively steered ring antenna array for automotive applications. *IEEE Trans. Antennas Propagat.*, vol. 55, no. 7, pp. 1902-1908, July 2010.

[42] F. Yu, K. G. Lyon and E. C. Kan. A novel passive RFID transponder using harmonic generation of nonlinear transmission lines. *IEEE Tran. Microw. Theory Tech.*, vol. 58, no. 12, pp. 4121-4127, Dec. 2010.

[43] F. Yu, K. G. Lyon and E. C. Kan. Harmonic generation from integrated nonlinear transmission lines for RFID applications. In *IEEE MTT-S Int. Microw. Symp. Dig.*, 2010.

[44] [Online].Available: http://www.mosis.com/vendors/view/ibm/8rf-dm

[45] W. Lee and E. Afshari. Low noise resonant parametric amplifier. *IEEE Tran. Circuits Syst. I*, vol. 58, no.3, pp. 479-492, Dec. 2011.

[46] E. Afshari, H. S. Bhat, A. Hajimiri and J. E. Marsden. Extremely wideband signal shaping using one- and two-dimensional nonuniform nonlinear transmission lines. *Journal of Applied Physics*, 2006.

[47] Wisp 5 firmware repository. http://www.github.com/wisp/, 2016.

[48] X. Li, Y. Zhang and M. G. Amin. Multi-frequency-based range estimation of RFID tags. In *Proc. IEEE Int. Conf. RFID*, 2009.

[49] J. Xiong and K. Jamieson. Arraytrack: A fine-grained indoor location system. In *USENIX NSDI*, 2013.

[50] S. Azzouzi, et al. New measurement results for the localization of UHF RFID transponders using an angle of arrival (AoA) approach. In *Proc. IEEE Int. Conf. RFID*, 2011.

[51] P.V. Nikitin and K.V.S Rao. Theory and measurement of backscattering from RFID tags. *IEEE Antennas and Propagation Magazine*, vol. 48, no. 6, pp. 212-218, Dec. 2008.

[52] Impinj. Get low-level reader data with LLRP, [Online]. Available: https://support.impinj.com.

[53] B.L. Pham and A.V. Pham. Triple bands antenna and high efficiency rectifier de-

sign for RF energy harvesting at 900, 1900 and 2400 MHz. In *IEEE MTT-S Int. Microw. Symp. Dig.*, 2013.

[54] ChibiOS-RT. [Online]. Available: http://www.chibios.org/dokuwiki/doku.php

[55] M. Scherhaufl, et al. Phase-of-arrival-based localization of passive UHF RFID tags. In *IEEE MTT-S Int. Microw. Symp. Dig.*, 2013.

[56] V. Viikari, et al. Ranging of UHF RFID tag using stepped frequency read-out. *IEEE Sensors J.*, vol. 10, no. 9, pp. 1535-1539, 2010.

[57] W.L. Stutzman and G.A. Thiele. Antenna theory and design, 3rd Edition, 2012.

[58] P.N. Betjes. An algorithm for automated phase center determination and its implementation. In *Proc. AMTA Conf.*, 2007.

[59] N. Mandayam. www.winlab.rutgers.edu/ narayan/Course/WSID/Lectures02/lect5.pdf.

[60] N. Mandayam. Basics of small scale fading: towards choice of PHY,[Online].Available:http://www.winlab.rutgers.edu/ narayan/Course/WSID/wsid-lec1c.ppt.

[61] P. V. Nikitin, et al. Theory and measurement of backscattering from RFID tags. *IEEE Antennas and Propagation Magazine*, vol. 48, no. 6, pp. 212-218, 2008.

[62] P. Bahl and V. N. Padmanabhan. RADAR: An in-building RF-based user location and tracking system. In *Proc. IEEE INFOCOM*, 2000.

[63] C. Xu, et al. Improving RF-based device-free passive localization in cluttered indoor environment through probabilistic classification methods. In *Proc. ACM/IEEE International Conference on Information Processing in Sensor Networks (IPSN)*, 2012.

[64] D. Zhang, et al. TASA: tag-free activity sensing using RFID tag arrays. *IEEE Trans. Parallel and Distributed Sys*, vol. 22, no. 4, 2011.

[65] J. Han, et al. Twins: device-free object tracking using passive tags. In *Proc. IEEE INFOCOM*, 2014.

[66] K. Wu, et al. CSI-based indoor localization. *IEEE Trans. Parallel and Distributed Sys.*, vol. 24, no. 7, pp. 1300-1309, July 2012.

[67] M. Youssef, M. Mah and A. Agrawala. Challenges: device-free passive localization for wireless environments. In *ACM MOBICOM*, 2007.

[68] F. Adib and D. Katabi. See through wall with wi-fi!. In *ACM SIGCOMM*, 2013.

[69] F. Adib and D. Katabi. 3D tracking via body radio reflections. In *USENIX NSDI*, 2014.

[70] F. V. Schultz, R. C. Burgener and S. King. Measurement of the radar cross section of a man. *Proc. IRE*, vol. 46, pp. 476-481, 1958.

[71] Y. Wu and D. C. Munson. Multi-static passive radar imaging using the smoothed pseudo winger-ville distribution. In *Proc. IEEE ICIP*, 2001.

[72] M. Cetin and A. D. Lanteman. Region-enhanced passive radar imaging. In *Proc. IEE Radar, Sonar and Navigation*, 2005.

[73] C. Liu, et al. The distributed passive radar 3D imaging and analysis in wavenumber domain. In *Proc. IEEE ICSP*, 2010.

[74] R. Srinivasan. Importance Sampling Applications in Communication and Detection. Springer, 2002.

[75] Y. Ma, X. Hui and E. C. Kan. 3D indoor locating in passive devices by broadband nonlinear backscatter. Submitted to *ACM MOBICOM*, 2016.

[76] Y. Ma and E. C. Kan. Ubiquitous tagless object locating by ambient harmonic tags. In *Proc. IEEE INFOCOM*, 2016.

[77] Y. Ma, H. Rong and E. C. Kan. Millimeter accuracy ranging by broadband harmonic backscatter against body motion interference. In *Proc. IEEE GLOBECOM*, 2015.

[78] M. G. Case. Nonlinear transmission lines for picosecond pulse, impulse and millimeter-wave harmonic generation. Ph.D. dissertation, Dept. of Elect. Comput. Eng., Univ. of California, Santa Barbara, 1993.

[79] J. Zhou, N. Reiskarimian and H. Krishnaswamy Receiver with integrated magnetic-free N-path-filter-based non-reciprocal circulator and baseband self-interference cancellation for full-duplex wireless. In *ISSCC Dig. Tech. Papers*, 2016.

[80] J. R. Shewchuk. An introduction to the conjugate gradient method without the agonizing pain. [Online:] https://www.cs.cmu.edu/ quake-papers/painless-conjugate-gradient.pdf, 2016.

[81] G. A. Bartels. GPS-antenna phase center measurements performed in an anechoic chamber. Delft University Press, 1997.